3-2004

A Rapidly-Converging Alternative to Source Iteration for Solving the Discrete Ordinates Radiation Transport Equations in Slab Geometry

Nicholas J. Wager

A RAPIDLY-CONVERGING ALTERNATIVE TO SOURCE ITERATION FOR SOLVING THE DISCRETE ORDINATES RADIATION TRANSPORT EQUATIONS IN SLAB GEOMETRY

DISSERTATION

Nicholas J. Wager, Lieutenant Colonel, US Army
AFIT/DSP/ENP/04-01

DEPARTMENT OF THE AIR FORCE
AIR UNIVERSITY

AIR FORCE INSTITUTE OF TECHNOLOGY

Wright-Patterson Air Force Base, Ohio

The views expressed in this thesis are those of the author and do not reflect the official policy or position of the United States Air Force, Department of Defense, or the United States Government.

AFIT/DSP/ENP/04-01

A RAPIDLY-CONVERGING ALTERNATIVE TO SOURCE ITERATION FOR SOLVING THE DISCRETE ORDINATES RADIATION TRANSPORT EQUATIONS IN SLAB GEOMETRY

DISSERTATION

Presented to the Faculty

Graduate School of Engineering and Management

Air Force Institute of Technology

Air University

Air Education and Training Command

in Partial Fulfillment of the Requirements for the

Degree of Doctor of Philosophy

Nicholas J. Wager, BS, MS

Lieutenant Colonel, USA

March 2004

AFIT/DSP/ENP/04-01

A RAPIDLY-CONVERGING ALTERNATIVE TO SOURCE ITERATION FOR SOLVING THE DISCRETE ORDINATES RADIATION TRANSPORT EQUATIONS IN SLAB GEOMETRY

Nicholas J. Wager, BA, MS
Lieutenant Colonel, US Army

Approved: Date

_____ _____
Kirk A. Mathews (Chairman)

_____ _____
William Wiesel (Dean's Representative)

_____ _____
Charles J. Bridgman (Member)

_____ _____
Dr. William P. Baker (Member)

Accepted:

_____ _____
Robert A. Calico, Jr. Date
Dean, Graduate School of Engineering and Management

Abstract

I present a numerical technique to solve the time independent Boltzmann Transport Equation for the transport of neutrons and photons. The technique efficiently solves the discrete ordinates equations with a new iteration scheme. I call this new scheme the angle space distribution iteration method because it combines a non-linear, high angular-resolution flux approximation within individual spatial cells with a coarse angular-resolution flux approximation that couples all cells in a spatial mesh. This is shown to be an efficient alternative to source iteration.

The new method is implemented using the step characteristic and exponential characteristic spatial quadrature schemes. The latter was introduced in 1993 and has been shown to be accurate for both optically thin and optically thick spatial meshes and to produce strictly positive angular fluxes.

The discrete ordinates equations can be solved using the conventional source iteration method. However, it is well known that this method converges prohibitively slowly for optically-thick problems with regions that are dominated by scattering rather than absorption. The new scheme converges rapidly even for such problems. Numerical results show that the new scheme is reliably accurate for the problems intended, and that it is fast and efficient in use of memory.

The angle space distribution iteration method is demonstrated in slab geometry, for a single energy group, using isotropic cross sections, with exponential and step characteristic spatial quadratures.

Acknowledgments

I would like to express my sincere appreciation to my faculty advisor, Dr. Kirk Mathews for his mentorship throughout my academic journey. His intelligence and insight are without parallel in my past experience. He taught me relevant physics, helped me understand key nuclear engineering concepts and coached me in analysis and methodology. He literally threw open the doors to his home for me and I am deeply grateful to him. He was and continues to be an outstanding teacher, mentor, and friend.

I am also indebted to my other committee members. Dr William Baker taught me methods of mathematical analysis that were crucial to the development, application and documentation of my research. In addition to this, his ability to run my shorts off during our numerous physical fitness excursions showed me that I could be an engineer and a warrior. Dr Charles Bridgman provided encouragement, deep insight and sage advice throughout my efforts. His commitment to my academic development is a small example of his lifetime of calm, competent, and selfless service. I am also indebted to LTC Nick Prins who helped edit my dissertation, rehearse my defense and was a friend throughout.

Most importantly, I am indebted to my family. It would not have been possible to meet the demands of this research effort without the love and support of my wife and my children. Their sacrifice was far greater than mine. My wife's encouragement and empathy helped me persevere. Finally I want to thank my parents who taught me to value education, to work with discipline, and to believe in myself.

Nicholas J. Wager

Table of Contents

Page

List of Figures

Page

Page

Page

Page

List of Algorithms

List of Acronyms

ASDI ..... Angle Spatial Distribution Iteration

BTE ..... Boltzmann transport equation

c ..... Scattering ratio

DD ..... Diamond Difference

DSA ..... Diffusion synthetic acceleration

EC ..... Exponential Characteristic

LD ..... Linear Discontinuous

NC ..... Non-Linear Characteristic

SC ..... Step Characteristic

SI ..... Source iteration

SI_ASDI ..... Source iteration on ASDI solution

TSA ..... Transport synthetic acceleration

ε_{SRD} ..... Symmetric relative difference

A RAPIDLY-CONVERGING ALTERNATIVE TO SOURCE ITERATION FOR SOLVING THE DISCRETE ORDINATES RADIATION TRANSPORT EQUATIONS IN SLAB GEOMETRY

I. Introduction

The conventional practice for evaluating the time independent discretized, Boltzmann transport equation is the discrete ordinates angular quadrature method with truncated Legendre expansions representing the cross sections. In discrete-ordinates S_n approximations of large transport problems the underlying linear Boltzmann problem is discretized in space and angle and the resulting system of algebraic equations is solved iteratively using source iteration. If the physical system contains regions that are diffusive and optically thick, source iteration can be so slow to converge as to make the calculations impractical, unless an effective convergence acceleration scheme can be found (7:36). Accurate, nonnegative spatial quadrature schemes, in particular the exponential characteristic (EC) method, are effective for optically thick absorbing regions but with unaccelerated source iteration they are prohibitively slow to converge in thick diffusive regions.

In the work presented here, I have developed new algorithms that invert the scattering operator in each cell and directly solve the linear system of coupled equations. This approach eliminates source iteration (SI), per se, but does require iteration. The iteration converges cell coupling coefficients which depend on the angular distribution of the flux and (for EC) the spatial distribution of the source. I have implemented and benchmarked a code to execute one dimension slab geometry particle transport. This transport is efficient in thick diffusive problems for the two non-negative spatial quadrature schemes tested. The method overcomes the inefficient dependence on numerous particle flights by SI to estimate scattering source and the corresponding lack of robustness in the

converged SI solution. The method is not designed as an accelerator for SI but as a new transport method. Since the new method converges on a solution by iteratively seeking improved angular and spatial distribution information I refer to it as the angular and spatial distribution iteration (ASDI) method. The ASDI method performs comparably with the SI method for those problems that don't require acceleration and rapidly converges in problems that conventionally require SI acceleration. This is particularly important in the thermal neutron energy range from about 0 to 1 eV (*2*:83).

In systems that are optically thick and scattering dominated, particles undergo many collisions before being captured or leaking out of the problem. Developing a practical efficient iterative method for these problems is of significant practical importance.

Examination of the one group time independent Boltzmann Transport Equation (BTE) illustrates the problem. A one group particle problem in planar geometry can be expressed as:

$$\mu\frac{\partial\psi(x,\mu)}{\partial x}+\sigma(x)\psi(x,\mu)= \int_{-1}^{1}\sigma_s(x,\mu'\to\mu)\psi(x,\mu')\,d\mu'+Q^{ext}(x,\mu) \qquad 0<x<X, \tag{1}$$

$$\psi(0,\mu)=\psi_L^{incident}(\mu)+\int_0^1 d\mu'\alpha_L(\mu'\to\mu)\psi(0,\mu') \qquad \mu>0 \tag{2}$$

$$\psi(X,\mu)=\psi_R^{incident}(\mu)+\int_{-1}^0 d\mu'\alpha_R(\mu'\to\mu)\psi(X,\mu') \qquad \mu<0 \tag{3}$$

where x is the position coordinate; μ is the direction cosine of the angle of flight relative to the positive x-axis; $\sigma(x)$ is the total cross section; $\sigma_s(x,\Omega'\cdot\Omega)$ is the scattering cross section; $Q(x,\mu)$ is the interior emission source, $\psi(x,\mu)$ is the angular flux to be determined. Equations (2) and (3) are general covering all but periodic boundary conditions on the left and right sides with appropriate choice of boundary condition $\alpha_L(\mu'\to\mu)$ or $\alpha_R(\mu'\to\mu)$.

By defining a streaming and collision operator as

$$L=(\mu\frac{\partial}{\partial x}+\sigma(x)), \tag{4}$$

and a scattering operator as

$$S=\int_{-1}^{1} d\mu'\sigma_s(x,\mu_s), \tag{5}$$

with μ_s the scattering angle, equation (1) is written

$$L\psi(x,\mu)=S\psi(x,\mu)+Q^{ext}(x,\mu). \tag{6}$$

Generally an analytic solution for $\psi(x,\mu)$ is not possible. Conventional practice is to approximate a solution iteratively using Source Iteration (SI). The SI scheme is

$$L\psi^{(\ell+1)}(x,\mu)=S\psi^{\ell}_{ext}(x,\mu)+Q^{\ell}_{ext}(x,\mu). \tag{7}$$

Operationally SI works as outlined in algorithm 1.

Initialize $\psi^{(0)}(x,\mu)$ *with initial estimate*

Do

Update $Q^{(\ell)}(x,\mu)=S\psi^{(\ell)}(x,\mu)+Q_{ext}(x,\mu)$

Apply Boundary Conditions

Solve $L\psi^{(\ell+1)}(x,\mu)=Q^{(\ell)}(x,\mu)$ *for* $\psi^{(\ell+1)}$

Iterate until $\varepsilon_{SRD}\left(\psi^{(\ell+1)},\psi^{(\ell)}\right)$ *is less than convergence tolerance*

End do

The symmetric relative difference function $\varepsilon_{\mathrm{SRD}}$ is introduced in Algorithm 1. This function has all the properties required of a distance function (*3*:23), as is shown in appendix A. Thus, the real numbers, with this metric, form a metric space. This metric is combined with the vector norm $\|\cdot\|_\infty$ to measure the maximum distance between two vectors, as is explained in appendix A.

The symmetric relative difference, $\varepsilon_{\mathrm{SRD}}\left(\bar{\psi}^{(\ell+1)}(x,\mu),\bar{\psi}^{(\ell)}(x,\mu)\right)$, is used to determine when two successive flux iterations, $\bar{\psi}^{(\ell+1)}(x,\mu)$ and $\bar{\psi}^{(\ell)}(x,\mu)$, meet convergence tolerance. The iteration estimate for angular flux is $\psi^{(\ell)}(x,\mu)$. It is the angular flux due to particles that have scattered at most $\ell-1$ times. When particles undergo few collisions, the SI scheme converges rapidly. However, for problems that contain diffusive regions that are optically thick and scattering dominated, SI schemes converge slowly and may converge falsely. If scattering ratios are nearly one then the error in the final iterate can be much greater than the difference (between it and the previous iterate) that satisfied the preassigned convergence criterion.(*4*:10). This makes it difficult to determine when an iteration scheme is suitably converged and renders an SI solution unreliable. Slow and false convergences dictate the need to either accelerate SI or develop a more efficient iterative scheme.

Motivation

Recently Adams and Larsen conducted a comprehensive review of 40 years of methods that improve iterative transport convergence. This work outlines four desirable properties for fast iterative schemes (4:139). An iterative method should:

1. Converge effectively requiring few iterations. Convergence effectiveness is typically characterized by spectral radius, or equivalently iteration count. Often lower- order S_N schemes, or coarser angular refinement are proposed to accelerate higher-order S_N schemes. Typically these lower order or coarser schemes use fewer unknowns per cell and require fewer transport calculations, or require transport calculations that are computationally cheaper than the higher-order transport scheme. However these lower-order schemes may not reduce iteration count significantly in difficult problems.

2. Be computationally efficient. Computational efficiency can be measured by basic memory storage requirements, algebraic cost to implement the method or overall computing time. If the equations

used to accelerate a transport scheme carry the same number of unknowns or use computationally expensive cell variables the equations may yield satisfactory spectral radius yet be so time consuming to solve that the low order scheme is unacceptable.

3. Be applicable to both heterogeneous and homogeneous problems. Recently it was discovered that synthetic acceleration when extended to multiple dimensions, can degrade or diverge. Transport synthetic acceleration (TSA) diverges (*5*:15/16; *6*:12/17) and diffusion synthetic acceleration (DSA) degrades from a spectral radius of 1/3 in a homogeneous material to a spectral radius of 0.88 (4: 139) in problems with periodic material interfaces. Other acceleration methods are expected to show similar degradation. The transport community needs a scheme that maintains a small spectral radius and is cheap computationally in both slab geometry and multiple dimensions.

4. Be portable to parallel systems of computers and not degrade in parallel performance as the number of processors becomes large.

In addition to the four properties outlined by Adams and Larsen I add a fifth property. An iterative method should

5. Be robust. By this I mean that it should be usably accurate for the full range of problems that we want to solve. This accuracy should not be achieved by operator tuning, fix-ups, or expert system hybridization but by aptness of the algorithm for the problem. This property will be referred to as robustness.

Synthetic acceleration and quasidiffusion techniques have been applied to particle transport in problems that are many mean free paths thick, with scattering ratios close to unity with mixed results. In slab geometry the greatest improvement in efficiency results from DSA provided that the diffusion equation is consistently differenced and scattering is either isotropic or weakly anisotropic. I sought to improve the iterative convergence rate of the exponential characteristic (EC) method as developed by Mathews and Minor in 1993(*7*) which is essentially the same as the non-linear characteristic (NC) method introduced by Waring, Walters and Morel in 1996 (*8*: 24-37). Wareing and Morel subsequently were able to develop an effective acceleration method in slab geometry for their NC for both homogeneous and heterogeneous materials with scattering ratios of one. They did not demonstrate application to periodic material interfaces, and they did not report compute time leaving the computational efficiency of their acceleration method in question. Their research has not been extended to multiple dimensions (*9*:76). Recent research has pointed toward the failure of DSA when used in multiple dimensions on problems with periodic interfaces. Because of this I did not pursue Wareing and Morel's DSA accelerator for use with EC. Instead I sought to find an efficient slab geometry scheme that would not suffer from DSA-like degradation in multiple dimensions. My motivation for doing this is that no accelerated source iteration technique to date is unconditionally stable, yields the same solution as the unaccelerated source iteration, is rapidly convergent, is demonstrated to be computationally efficient, is general with respect to geometry and can be applied to the EC method. The research effort at the Air Force Institute of Technology

requires efficient solution of the transport equation in all dimensions. Mathews and his research team require an effective (low iteration count), computationally efficient (fast run time), robust (reliably accurate without user intervention) EC method applicable to homogeneous and heterogeneous materials of any configuration or geometry in order use the EC spatial quadrature on a wide range of transport problems of interest to the defense community. Further it is desirable that such a method be readily adapted for use with parallel computing environments.

Goal of the Research

My goal was to develop, implement, and evaluate an effective, computationally efficient, robust method for solving the one group, slab geometry Boltzmann transport equation (BTE) discretized in angle and space. I further sought to develop a method that was general with respect to material properties, was readily portable to parallel computing environments, and could be extended to multiple dimensions. I designed the method primarily for use with EC and step characteristic (SC) spatial quadratures but sought a method that could also be used with other spatial quadratures.

Scope

I derive a new transport method that explicitly solves for infinite particle flights in a single iteration. The method couples across cells in space using a two direction angular quadrature. This is referred to as the global space solution. The method further solves particle transport within each spatial cell coupling the N directions of a fine angular quadrature. This is called the fine angle solution. The theory of both the global space solution and fine angle solution is introduced as well as a technique to combine these methods in an iterative scheme that converges flux distribution as opposed to scattering source in order to solve the BTE iteratively.

The method is implemented and tested using discrete elements one group isotropic average cross sections with EC and SC spatial quadratures. The method is derived in a way that generalizes to include discrete ordinates Legendre moment generated cross sections (σ_l), multigroup anisotropic cross sections, and other positive spatial quadratures such as linear discontinuous (LD) and NC. The method was not tested with spatial quadratures that produce negative fluxes such as diamond difference (DD). The method might be expanded to include these spatial quadratures but would have to account for negative flux values in calculation of flux weights. This was not derived or tested. The new method for particle transport is validated by comparison with unaccelerated conventional SI for EC and SC. The symmetric relative difference, number of iterations and compute time for the two methods is the basis of comparison.

The scope of the test problems examined is:

- Fixed source, sub-critical, time independent systems
- Slab geometry
- Single group isotropic cross sections
- Isotropic emission sources uniform in each cell

- EC and SC spatial quadratures

Although the method was examined with the above scope it was derived in a general way. The extension to multigroup problems is immediate. The emission source can include down scatter, up scatter and fission contributions. Non-positive spatial quadratures such as DD will require new algorithms to calculate flux weights from negative angular fluxes.

Assumptions and Limitations

The method as designed and tested when using the EC spatial quadrature and discrete elements angular quadrature inherits limitations of these approximations. EC is not currently extendable to curvilinear geometry. Discrete elements angular quadratures lead to numerical approximations that are not the same as the diffusion approximation.

Approach

An explicit system of equations for the angular and spatially discretized BTE using a general linear spatial quadrature is derived in N directions. This system, although illustrative, is impractical to solve. A similar system using only two directions is introduced. A closed form solution of this two direction fully spatially coupled system is derived which is correct for transport with only two directions. The concepts of transport coefficients and flux weights are introduced. Transport coefficients define the relationships of incoming angular

fluxes and source emissions to outgoing angular fluxes within a spatial cell. Flux weights facilitate the projection of the system of equations between multiple directions and two directions. Then they are used to calculate a closed form solution using a coarse angle approximation which effectively solves for flux across the entire problem space. The cell edge flux calculated in this way is correct if the flux weights used to collapse the transport coefficients are correct. The coupling of the exact N direction transport method (using approximate edge flux values) with the equivalent 2 direction collapsed transport coefficient method (also using approximate edge flux values) is then introduced. An iteration scheme that produces progressively more accurate flux weights which are used to compute progressively more accurate transport coefficients is then discussed. This method effectively amounts to iteration on transport coefficients. The method differs significantly in concept and execution from accelerated SI. For instance, accelerated source iteration follows the logic of algorithm 2.

Intialize $Q\left(\psi^{(0)}\right)$

Do

Calculate $Q\left(\psi^{(\ell)}\right)$

Apply Boundary Conditions

Solve $L\psi^{(\ell+1)}\left(x,\mu\right)=Q^{(\ell)}\left(x,\mu\right)$ *for* $\psi^{(\ell+1)}$

Apply accelerator correction

End do when $s_{\ldots}\left(\vec{\psi}^{(\ell+1)}(x,\mu),\vec{\psi}^{(\ell)}(x,\mu)\right)<convergenceTolerance$

The method proposed in this research follows the logic of Algorithm 3

Initialize cell coupling coefficients with coarse angle approximation

Use 2 direction SC cell coupling coefficients to generate $\psi^{(o)}$

Do

Solve for fine angle flux within cells

Generate improved low-resolution cell coupling coefficients

Solve for fine angle flux within cells

Use low resolution edge flux to improve high resolution edge flux

$(\epsilon+1)$ (ϵ)

Algorithm 3 is implemented in Fortran 95 and benchmarked against unaccelerated source iteration which is also implemented in Fortran 95.
The ASDI method is then extended to the EC spatial quadrature by adding an iteration loop to find the source distribution parameter, β, but otherwise retains the same logic as algorithm 2. It is also written in Fortran 95 and is benchmarked against an unaccelerated source iteration.

II. Solution of the Discrete Ordinates (S_n) Transport Equations

Solution of the monoenergetic BTE introduced in Chapter 1 requires treatment of the space and angular variables through a number of discretization techniques that yield simultaneous equations. The discrete ordinates method is a widely used method for obtaining numerical solutions to the integrodifferential form of the transport equation. It is the method used in this research to discretize the Boltzmann transport equation in space and angle. A brief discussion of space and angle discretization follows.
In one group, slab geometry the scattered source on the right hand side of equation **(1)** may be replaced by a Legendre expansion (2:13,36,117):

$$\mu\frac{\partial\psi(x,\mu)}{\partial x}+\sigma(x)\psi(x,\mu)= \sum_{k=0}^{\infty}(2k+1)P(\mu)\sigma_{s_k}\phi_k+Q^{ext}(x,\mu) \qquad 0<x<X, \tag{8}$$

where σ_{s_k} are the Legendre moments of the scattering cross section and ϕ_k are the Legendre moments of the angular flux:

$$\phi_k(x)=\int_{-1}^{1}\frac{d\mu'}{2}P_k(\mu')\psi(x,\mu'). \tag{9}$$

The discrete ordinates approximation consists of requiring equation (8) to hold only for a number (N) of discrete directions then applying a compatible quadrature approximation to the flux moments in each of these directions. The weighted quadrature used for the flux moments has the form

$$\phi_k(x)=\sum_{n'=1}^{N}w_{n'}P_k(\mu_{n'})\psi(x,\mu_{n'}). \tag{10}$$

Substituting the weighted quadrature, at N distinct angles, with a Legendre expansion truncated at a finite number of polynomials (K) in equation (8) results in

$$\mu\frac{\partial\psi(x,\mu_n)}{\partial x}+\sigma(x)\psi(x,\mu_n)= \sum_{n'=1}^{N} w_{n'}\psi(x,\mu_{n'})\sum_{k=0}^{K}(2k+1)\sigma_{s_k}(x)P_k(\mu_n)P_k(\mu_{n'})+Q^{ext}(x,\mu_n). \qquad 0<x<X \tag{11}$$

The coupling of the system of equations occurs on the right hand side. The left hand side represents a set of angularly independent first order differential equations. Defining $\sigma_{s_{n',n}}$ to be the ordinate to ordinate scattering cross section:

$$\sigma_{s_{n'\to n}}(x)=\sum_{k=0}^{K}(2k+1)\sigma_{s_k}(x)P_k(\mu_{n'})P_k(\mu_n), \tag{12}$$

facilitates writing equation (11) as

$$\mu_n\frac{d\psi_n(x)}{dx}+\sigma(x)\psi_n(x)=\sum_{n'=1}^{N}\sigma_{s_{n'\to n}}(x)w_{n'}\psi_{n'}(x)+Q_n^{ext}(x). \tag{13}$$

Equation (13) represents a system of N coupled differential equations.
The method I have developed is dependent on representing the discrete ordinates equations in the form of equation (13) with the coupling of the system taking place on the right hand side through the term $\sum_{n'=1}^{N}\sigma_{s_{n'\to n}}(x)w_{n'}\psi_{n'}(x)$. How the cross section data weights and ordinate direction cosines are arrived at is not important to my work. Other methods, such as that introduced in 2003 by Gerts and Mathews, which calculate cross sections using piecewise averages and discrete elements (*10*), may be used if the discrete direction flux equations can be represented in a form analogous to equation (13) A brief discussion of their work follows.

Dropping spatial dependence, the scattered source term on right hand side of equation (1) is written

$$Q_s=\int_{4\pi}d\hat{\Omega}'\sigma_s\left(\hat{\Omega}\cdot\hat{\Omega}'\right)\psi\left(\hat{\Omega}'\right), \tag{14}$$

where $\hat{\Omega}$ is a unit vector:

$$\hat{\Omega} = \{Sin(\theta)Cos(\omega), Sin(\theta)Sin(\omega), Cos(\theta)\}, \tag{15}$$

and

$$\mu = Cos(\theta) \tag{16}$$

The discrete elements method approximates scattered source within an element, Q_{s_n}, by

$$Q_{s_n} = \int_{\Delta\Omega_n} Q_s\left(\hat{\Omega}\right) d\hat{\Omega}, \tag{17}$$

and angular flux within an element by

$$\psi_{n'} = \int_{\Delta\Omega_n} \psi\left(\hat{\Omega}'\right) d\hat{\Omega}'. \tag{18}$$

In the above equation $\Delta\Omega_n$ is the Cartesian product of the angular interval from $[0, 2\pi)$ and the μ interval containing the ordinate μ_n. The union of the μ intervals covers the range $[-1,1]$ with no overlap. An element of solid angle on the surface of the unit sphere in 1D slab geometry is:

$$\int_{\Delta\Omega_{n'}} d\Omega = \int_{\Delta\mu_{n'}} d\mu \int_0^{2\pi} d\omega \ . \tag{19}$$

Equation (18) is:

$$\psi_{n'} = \int_{\Delta\mu_{n'}} d\mu \int_0^{2\pi} d\omega \ \psi(\mu, \omega), \tag{20}$$

Equation (17) is:

$$Q_{s_n} = \int_{\Delta\mu_n} d\mu \int_0^{2\pi} d\omega \, Q_s(\mu, \omega), \tag{21}$$

and equation (14) is

$$Q_{s_n} = \int_{\Delta\mu_n} d\mu \int_0^{2\pi} d\omega \sum_{n'} \int_{\Delta\mu_{n'}} d\mu' \int_0^{2\pi} d\omega' \sigma_s\left(\{\mu',\omega'\}.\{\mu,\omega\}\right)\psi\left(\mu',\omega'\right) \tag{22}$$

The order of summation and integration in equation (22) may be rearranged resulting in:

$$Q_{s_n} = \sum_{n'} \int_{\Delta\mu_n} d\mu \int_0^{2\pi} d\omega \int_{\Delta\mu_{n'}} d\mu' \int_0^{2\pi} d\omega' \sigma_s\left(\{\mu',\omega'\}.\{\mu,\omega\}\right)\psi\left(\mu',\omega'\right). \tag{23}$$

In slab geometry $\psi\left(\mu',\omega'\right)$ has no ω' dependence:

$$\psi\left(\mu',\omega'\right) = \frac{\psi(\mu')}{2\pi}. \tag{24}$$

Substituting equation (24) into equation (20) results in:

$$\psi_{n'} = \int_{\Delta\mu_{n'}} d\mu' \psi\left(\mu_n'\right). \tag{25}$$

Substituting equation (25) into equation (23) results in:

$$Q_{s_n} = \sum_{n'} \int_{\Delta\mu_n} d\mu \int_{\Delta\mu_{n'}} d\mu' \psi\left(\mu'\right) \int_0^{2\pi} \frac{d\omega'}{2\pi} \int_0^{2\pi} d\omega \sigma_s\left(\{\mu',\omega'\}.\{\mu,\omega\}\right). \tag{26}$$

Within each angular element, the flux is approximated as isotropic:

$$\psi\left(\mu'\right) = \frac{\psi_{n'}}{\Delta\mu_{n'}}. \tag{27}$$

Substituting equation (27) into equation (26) and rearranging the order of integration results in

$$Q_{s_n} = \sum_{n'} \psi_{n'} \int_{\Delta\mu_n} d\mu \int_{\Delta\mu_{n'}} \frac{d\mu'}{\Delta\mu_{n'}} \int_0^{2\pi} \frac{d\omega}{2\pi} \int_0^{2\pi} d\omega' \sigma_s\left(\{\mu',\omega'\}.\{\mu,\omega\}\right). \tag{28}$$

The integral of equation (28) defines the element to element scattering cross section $\overline{\sigma}_{s_{n'\to n}}$:

$$\overline{\sigma}_{s_{n'\to n}} = \int_{\Delta\mu_n} d\mu \int_{\Delta\mu_{n'}} \frac{d\mu'}{\Delta\mu_{n'}} \int_0^{2\pi} \frac{d\omega}{2\pi} \int_0^{2\pi} d\omega' \sigma_s\left(\{\mu',\omega'\}.\{\mu,\omega\}\right). \tag{29}$$

Using this discrete elements angular quadrature,

$$Q_{s_n} = \sum_{n'} \overline{\sigma}_{s_{n'\to n}} \psi_{n'} . \tag{30}$$

The element-to-element scattering cross section $\overline{\sigma}_{s_{n'\to n}}$ is analogous to the ordinate-to-ordinate scattering cross section in equation (13). With discrete elements, there are no quadrature weights per se. These are replaced by the sizes of the elements $\Delta\mu_n$, and are treated implicitly through the calculation of $\overline{\sigma}_{s_{n'\to n}}$. Bothe angular quadratures have the same form if weights $w_n = 1$ are introduced in equation (30). Gerts and Mathews' work has the advantage of representing cross sections with non-negative values in sharp contrast to certain cross sections arrived at through Legendre expansion. My derivation and implementation is done with discrete elements cross sections because they are non-negative. I will use the term ordinate in my work since it is more common in the transport community but I intend for the term to refer to both ordinate in the discrete ordinates sense and element in the discrete elements sense. The numerical results presented in chapter 3 and chapter 5 used discrete elements.

Because the coupling of the system represented by (13) occurs on the right hand side, it is useful to combine the right hand side as a single term $Q_n(x)$:

$$Q_n(x) = S_n(x) + E_n(x), \tag{31}$$

where

$$S_n(x) = \sum_{n'=1}^{N} \sigma_{s_{n'\to n}} w_{n'} \psi_{n'}(x). \tag{32}$$

The source of scattered particles is $S_n(x)$ and the source of emitted particles is $E_n(x)$. Equation (13) is then

$$\mu_n \frac{\partial \psi_n(x)}{\partial x} + \sigma(x)\psi_n(x) = Q_n(x) \quad n = 1,\ldots N. \tag{33}$$

This results in N coupled differential equations for N ordinates.

The system represented by equation (33) is easily solved once spatially discretized using an iterative scheme like:

$$\mu_n \frac{\partial \psi_n^{(\ell+1)}(x)}{\partial x} + \sigma(x)\psi_n^{(\ell+1)}(x) = Q_n^{(\ell)}(x) \qquad n = 1,\ldots N \tag{34}$$

where ℓ is an iteration index. This is called source iteration. If one starts with a guess of zero for scalar flux the first iteration yields the uncollided flux, the second iteration yields the uncollided plus first collided flux, the next iteration yields the uncollided plus first and second collided flux and so on. In order to calculate a numerical solution for equation (34), it is first spatially discretized. The indexing for spatial discretization is shown in Figure 1.

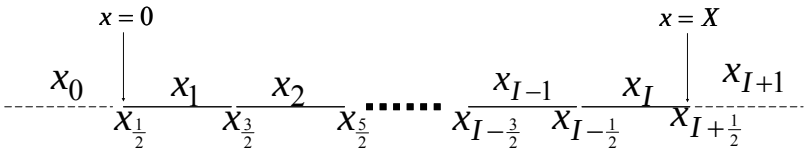

Figure 1 Spatial Index

In the spatial discretization shown in Figure 1, cell edge quantities carry half-integer indices and cell-average quantities carry integer indices. The total number of mesh cells is denoted by *I*. On the left and right sides are phantom cells, denoted with 0 and I+1 respectively. These phantom cells are a convenient accounting construct. They produce neither intrinsic nor scattered source. They have no thickness so they produce no particle losses. They do however contain edge flux information at the problem left and right boundaries.

The first step in the spatial discretization of equation (34) is to spatially integrate it over a cell to obtain a balance equation for the i^{th} spatial cell. In the ith cell, as indicated by Figure 1, the left edge is at $x_{i-\frac{1}{2}}$ while the right edge is at $x_{i+\frac{1}{2}}$. The thickness of cell i is $\Delta x_i = x_{i+\frac{1}{2}} - x_{i-\frac{1}{2}}$. We presume that material discontinuities are also cell edges so that $\sigma(\mathrm{x})$ is a constant σ_i, within each cell. Angular flux on the right and left cell edges are $\psi_{n,i+\frac{1}{2}}, \psi_{n,i-\frac{1}{2}}$ respectively. The subscript n denotes the ordinate and the subscript i denotes the mesh cell. Integration of the of the flux in the ith cell results in

$$\frac{\mu_n}{\Delta x_i}(\psi_{n,i+\frac{1}{2}} - \psi_{n,i-\frac{1}{2}}) + \sigma_i \psi_{n,i} = Q_{n,i}\,, \tag{35}$$

Where $Q_{n,i}$ is the average source in cell i:

$$Q_{n,i} = \int_{x_{i-\frac{1}{2}}}^{x_{i+\frac{1}{2}}} \frac{dx}{\Delta x}\, Q_n(x)\,. \tag{36}$$

The average source in cell i consists of average scatters ($S_{A_{n,i}}$) and average emissions ($E_{A_{n,i}}$):

$$Q_{n,i} = S_{A_{n,i}} + E_{A_{n,i}}\,. \tag{37}$$

Again the average scattered source in cell i, $S_{A_{n,i}}$, is found by integrating the scattered source, $S_n(x)$, over the cell:

$$S_{A_{n,i}} = \int_{x_{i-\frac{1}{2}}}^{x_{i+\frac{1}{2}}} \frac{dx}{\Delta x}\, S_n(x)\,. \tag{38}$$

The average intrinsic source in cell i, $E_{A_{n,i}}$, is also found by integrating the intrinsic emission source, $E_n(x)$, over the cell:

$$E_{A_{n,i}} = \int_{x_{i-\frac{1}{2}}}^{x_{i+\frac{1}{2}}} \frac{dx}{\Delta x}\; E_n(x)\,. \tag{39}$$

In practice the average scattered source is not calculated from equation (38) but from scattering cross sections and average angular flux. The average angular flux in cell i is:

$$\psi_{n,i} = \int_{x_{i-\frac{1}{2}}}^{x_{i+\frac{1}{2}}} \frac{dx}{\Delta x} \psi_n(x)\,. \tag{40}$$

The scattering cross sections from ordinate n' to ordinate n are assumed to be constant for cell i (as was done for total cross section) and are denoted as $\sigma_{s_{n',n,i}}$. Hence, the average scattered source of equation (38) can be written

$$S_{A_{n,i}} = \sum_{n'=1}^{N} w_{n'} \sigma_{s\,n',n,i}\, \psi_{n',i} \,. \tag{41}$$

Using equation (41) and equation (37) to substitute for the right hand side of equation (35) yields a system of equations that can be solved analytically if another equation is introduced and one of the fluxes (incoming, outgoing, or average) is known. If the incoming flux is known for each direction in a cell, the average and outgoing fluxes are the system unknowns. Two equations are needed for each direction but only the balance equation in each direction has yet been introduced. To complete the system of equations an additional equation for each direction is needed. This additional equation is known as the auxiliary equation. Given the balance equation and an auxiliary equation for a cell with an N direction angular refinement, it is straightforward to solve for the exiting flux. This can be done for every cell in a spatial approximation.

The conventional scheme sweeps through the cells in the direction of motion of the particles. Consider an example with quadrature points indexed in order of decreasing direction cosine but not necessarily symmetric about $\mu = 0$. Let μ_1 through μ_{N_R} be positive (rightward) and $\mu_{N_{R+1}}$ through μ_N be negative (leftward). The solution process for a multicell spatial discretization begins by solving for exiting edge flux $\psi_{N_R+1,I-\frac{1}{2}}$ and average flux $\psi_{N_R+1,I}$, where I denotes the total number of mesh cells and N_R+1 denotes a leftward direction whose direction cosine is smallest in magnitude among the direction cosines of the quadrature set. The incoming edge flux at the right face is $\psi_{N_R+1,I+\frac{1}{2}}$. It is known from the boundary condition at the right edge. With a vacuum or source boundary these values are explicitly known but with a reflective condition the incoming edge flux values are set to the appropriate outgoing edge flux values using the latest iteration estimate for these fluxes. After solving for outgoing flux at edge $\psi_{N_R+1,I-\frac{1}{2}}$ this value is used as the input for the adjacent cell then $\psi_{N_R+1,I-\frac{3}{2}}$ and $\psi_{N_R+1,I-1}$ are calculated. The solution process commonly referred to as a sweep proceeds across each cell until the left boundary is reached. The process is repeated for all remaining fluxes with $\mu_n < 0$. When the left face is reached for each ordinate the boundary condition is used to determine $\psi_{N_R,\frac{1}{2}}$. This value is used as the incoming

edge flux for the far left cell. Outgoing edge flux ($\psi_{N_R,\frac{3}{2}}$) and average angular flux $\psi_{1,1}$ are calculated. Outgoing edge flux from cell 1 ($\psi_{N_R,\frac{3}{2}}$) is used as input for the second cell. This procedure continues through the mesh successively solving for the average and outgoing fluxes in each cell until the right boundary is reached. The process is then repeated for all remaining ordinates. An iteration is complete when fluxes for all ordinates are calculated in all cells. Upon completion of an iteration, the source term is re-calculated from equation(37) and the sweep process begins again.

An alternative to source iteration is to consider the entire spatial and angular mesh as a system of equations with outgoing cell edge fluxes and cell average fluxes as the unknown variables. These variables are calculated by multiplying cell incoming fluxes, average intrinsic sources, and average scattered sources by coefficients that are determined by the spatial quadrature (spatial differencing) scheme. These spatial quadrature coefficients are scalar quantities that are calculated from cell cross section σ_i, particle direction μ_n, and cell thickness Δx_i. Certain spatial differencing schemes, such as EC, also use first moments to calculate them. I will discuss EC in chapter 4.

The discrete ordinates system of equations represented by equation (33) can be written as the contribution of cell incoming edge flux, scattered source and emission source multiplied by a transport coefficient to cell outgoing edge flux is

$$\begin{aligned}\psi_{n,i+\frac{1}{2}} &= K_{OI_{n,i}}\left(\sigma_i,\mu_n,\Delta x_i,S_{A_{n,i}},S_{x_{n,i}}\right)\psi_{n,i-\frac{1}{2}} \\ &+ K_{OS_{n,i}}\left(\sigma_i,\mu_n,\Delta x_i,S_{A_{n,i}},S_{x_{n,i}}\right)S_{A_{n,i}} \\ &+ K_{OE_{n,i}}\left(\sigma_i,\mu_n,\Delta x_i,S_{A_{n,i}},S_{x_{n,i}}\right)E_{A_{n,i}} \qquad \mu_n > 0,\end{aligned} \tag{42}$$

$$\begin{aligned}\psi_{n,i-\frac{1}{2}} &= K_{OI_{n,i}}\left(\sigma_i,\mu_n,\Delta x_i,S_{A_{n,i}},S_{x_{n,i}}\right)\psi_{n,i+\frac{1}{2}} \\ &+ K_{OS_{n,i}}\left(\sigma_i,\mu_n,\Delta x_i,S_{A_{n,i}},S_{x_{n,i}}\right)S_{A_{n,i}} \\ &+ K_{OE_{n,i}}\left(\sigma_i,\mu_n,\Delta x_i,S_{A_{n,i}},S_{x_{n,i}}\right)E_{A_{n,i}} \qquad \mu_n < 0.\end{aligned} \tag{43}$$

The spatial quadrature also provides coefficients for determining the cell average fluxes:

$$\psi_{n,i} = K_{AI_{n,i}}\left(\sigma_i, \mu_n, \Delta x_i, S_{A_{n,i}}, S_{x_{n,i}}\right)\psi_{n,i-\frac{1}{2}} + K_{AS_{n,i}}\left(\sigma_i, \mu_n, \Delta x_i, S_{A_{n,i}}, S_{x_{n,i}}\right)S_{A_{n,i}} + K_{AE_{n,i}}\left(\sigma_i, \mu_n, \Delta x_i, S_{A_{n,i}}, S_{x_{n,i}}\right)E_{A_{n,i}} \qquad \mu_n > 0, \tag{44}$$

$$\psi_{n,i} = K_{AI_{n,i}}\left(\sigma_i, \mu_n, \Delta x_i, S_{A_{n,i}}, S_{x_{n,i}}\right)\psi_{n,i+\frac{1}{2}} + K_{AS_{n,i}}\left(\sigma_i, \mu_n, \Delta x_i, S_{A_{n,i}}, S_{x_{n,i}}\right)S_{A_{n,i}} + K_{AE_{n,i}}\left(\sigma_i, \mu_n, \Delta x_i, S_{A_{n,i}}, S_{x_{n,i}}\right)E_{A_{n,i}} \qquad \mu_n < 0. \tag{45}$$

For compactness of notation the transport coefficients will be written without their arguments, unless these arguments are necessary for discussion or clarity. The spatial quadrature coefficients will be written as $K_{OI_{n,i}}$, $K_{OS_{n,i}}$, $K_{OE_{n,i}}$, $K_{AI_{n,i}}$, $K_{AS_{n,i}}$, $K_{AE_{n,i}}$. These spatial quadrature coefficients can be obtained from any spatial discretization (spatial quadrature). They are a convenient representation of the coupled differential equations of the discrete ordinates equations. These coefficients are derived for an SC spatial quadrature in the next section. SC is chosen in this research because it is a positive method, like EC, but is linear which simplifies implementation. Successful SC implementation does not guarantee extension to EC but was used to test method implementation before applying it to the more sophisticated EC spatial quadrature which uses first moments.

SC Transport Coefficients

In this section, formulas for the step characteristic (SC) spatial quadrature coefficients are derived. SC approximates the scattering and emission sources as being

uniformly distributed in a cell. The flux in the cell is obtained as characteristic solutions along each direction of the angular quadrature. This is evaluated at the outflow face and is averaged over the cell to obtain these coefficients.

Dividing equation (33) by μ_n results in:

$$\frac{\partial \psi_n(x)}{\partial x} + \frac{\sigma(x)}{\mu_n}\psi_n(x) = \frac{1}{\mu_n} Q_n(x). \tag{46}$$

Let the optical thickness from a point $\tilde{x}$ to a point x along the direction of the n^{th} ordinate be $\tau_n\left(x, \tilde{x}\right)$:

$$\tau_n\left(x, \tilde{x}\right) = \frac{1}{\mu_n}\int_{\tilde{x}}^{x} dx' \sigma(x') \qquad \tilde{x} \le x' \le x, \tag{47}$$

If σ is a constant between $\tilde{x}$ and x, then

$$\tau_n\left(x, \tilde{x}\right) = \frac{\sigma}{\mu_n}\left(x - \tilde{x}\right). \tag{48}$$

Now introducing the integrating factor $e^{\tau_n\left(x,\tilde{x}\right)}$ into equation (46) and replacing $\frac{\partial \psi_n(x)}{\partial x}$ with $\frac{d\psi_n(x)}{dx}$ results in

$$\frac{d\psi_n(x)}{dx} e^{\tau_n\left(x,\tilde{x}\right)} + \frac{\sigma(x)}{\mu_n}\psi_n(x) e^{\tau_n\left(x,\tilde{x}\right)} = \frac{1}{\mu_n} Q_n(x) e^{\tau_n\left(x,\tilde{x}\right)}. \tag{49}$$

Noting that

$$\frac{d}{dx}\left(\psi_n(x) e^{\tau_n\left(x,\tilde{x}\right)}\right) = \frac{\partial \psi_n(x)}{\partial x} e^{\tau_n\left(x,\tilde{x}\right)} + \frac{\sigma(x)}{\mu_n}\psi_n(x) e^{\tau_n\left(x,\tilde{x}\right)}, \tag{50}$$

and integrating equation (49) from $\tilde{x}$ to x produces

$$\psi_n(x)\,e^{\tau_n\left(x,\tilde{x}\right)}-\psi_n\left(\tilde{x}\right)e^{\tau_n\left(\tilde{x},\tilde{x}\right)}=\int_{\tilde{x}}^{x}\frac{dx'}{\mu_n}\,Q_n(x')\,e^{\tau_n\left(x',\tilde{x}\right)}\,. \tag{51}$$

Dividing equation (51) by the integrating factor and rearranging terms results in

$$\psi_n(x)=\psi\left(\tilde{x}\right)_n\,e^{\left(\tau_n(\tilde{x},\tilde{x})-\tau_n(x,\tilde{x})\right)}+\frac{1}{\mu_n}\int_{\tilde{x}}^{x}\frac{dx'}{\mu_n}\,Q_n(x')\;e^{\tau_n(x',\tilde{x})-\tau_n(x,\tilde{x})}\,, \tag{52}$$

where $e^{\tau_n\left(\tilde{x},\tilde{x}\right)}$ is 1. If $\mu_n>0$ the flux is entering from the left cell edge and $\tilde{x}=x_L$. If $\mu_n<0$ the flux is entering from the right cell edge and $\tilde{x}=x_R$. This leads to

$$\psi_n(x)=\psi\left(x_L\right)_n\,e^{-\tau_n(x,x_L)}+\frac{1}{\mu_n}\int_{x_L}^{x}\frac{dx'}{\mu_n}\,Q_n(x')\;e^{\tau_n(x',x_L)-\tau_n(x,x_L)}\qquad\mu_n>0\,, \tag{53}$$

$$\psi_n(x)=\psi\left(x_R\right)_n\,e^{-\tau_n(x,x_R)}-\frac{1}{\mu_n}\int_{x}^{x_R}\frac{dx'}{\mu_n}\,Q_n(x')\;e^{\tau_n(x',x_R)-\tau_n(x,x_R)}\qquad\mu_n<0\,. \tag{54}$$

In the i[th] cell as indicated by Figure 1 x_L corresponds to $x_{i-\frac{1}{2}}$ while x_R corresponds to $x_{i+\frac{1}{2}}$. Further if $\Delta x=x_{i+\frac{1}{2}}-x_{i-\frac{1}{2}}$ is sufficiently small, $\sigma\left(x\right)$ can be assumed to be a constant σ_i, the average over the cell. Equation (48) is then

$$\tau_n\left(x,\tilde{x}\right)=\frac{\sigma_i}{\mu_n}\left(x-\tilde{x}\right). \tag{55}$$

This is readily expressed in terms of the optical thickness of cell i in direction n, which I denote as

$$\left|\varepsilon_{n,i}\right|=\left|\frac{\sigma_i\,\Delta x_i}{\mu_n}\right|. \tag{56}$$

Thus,

$$\tau_n\left(x, x_{i-\frac{1}{2}}\right) = \left|\varepsilon_{n,i}\right| \frac{\left(x - x_{i-\frac{1}{2}}\right)}{\Delta x_i}, \tag{57}$$

and in a similar way

$$\tau_n\left(x, x_{i+\frac{1}{2}}\right) = \left|\varepsilon_{n,i}\right| \frac{\left(x_{i+\frac{1}{2}} - x\right)}{\Delta x}. \tag{58}$$

Substituting equation (57), equation (58), and the source integral as given by equation (31) these cell flux equations are:

$$\begin{aligned}
\psi_n(x) = \psi_{n,i-\frac{1}{2}}\, e^{-\left|\varepsilon_{n,i}\right| \frac{\left(x - x_{i-\frac{1}{2}}\right)}{\Delta x_i}} \\
+ \int_{x_{i-\frac{1}{2}}}^{x} \frac{dx'}{|\mu_n|} S_n(x')\, e^{-\left|\varepsilon_{n,i}\right| \frac{(x-x')}{\Delta x_i}} \\
+ \int_{x_{i-\frac{1}{2}}}^{x} \frac{dx'}{|\mu_n|}\, E_n(x)\, e^{-\left|\varepsilon_{n,i}\right| \frac{(x-x')}{\Delta x_i}} \qquad \mu_n > 0
\end{aligned} \tag{59}$$

$$\begin{aligned}
\psi_n(x) = \psi_{n,i+\frac{1}{2}}\, e^{-\left|\varepsilon_{n,i}\right| \frac{\left(x_{i+\frac{1}{2}} - x\right)}{\Delta x_i}} \\
+ \int_{x}^{x_{i+\frac{1}{2}}} \frac{dx'}{|\mu_n|} S_n(x')\, e^{-\left|\varepsilon_{n,i}\right| \frac{(x'-x)}{\Delta x_i}} \\
+ \int_{x}^{x_{i+\frac{1}{2}}} \frac{dx'}{|\mu_n|}\, E_n(x')\, e^{-\left|\varepsilon_{n,i}\right| \frac{(x'-x)}{\Delta x_i}} \qquad \mu_n < 0
\end{aligned} \tag{60}$$

Physically these equations determine the flux $\psi_n(x_i)$ in a cell as the superposition of the flux entering at a cell edge and the flux due to source production from scatters and emissions. In the above equations $S_n(x')$ is the source of scattered particle emissions and $E_n(x')$ is the source of intrinsic particle emissions at position x' into ordinate n. A

characteristic scheme introduces approximation by assuming a convenient form for the scattered source distribution then computes the exact angular flux corresponding to this assumed source distribution. A step characteristic spatial quadrature assumes that the source distribution is constant in cell i in ordinate μ_n. This constant source distribution averaged over a spatial cell is

$$S_{A_{n,i}} = \int_{x_{i-\frac{1}{2}}}^{x_{i+\frac{1}{2}}} \frac{dx}{\Delta x} S_n(x). \tag{61}$$

In practice $S_{A_{n,i}}$ is not calculated from equation (61) but is obtained from available cell information using

$$S_{A_{n,i}} = \sum_{n'=1}^{N} \sigma_{s_{n'n,i}} w_{n'} \psi_{n',i}. \tag{62}$$

Setting $x = x_{i+\frac{1}{2}}$ in equation (59) produces the flux exiting the right edge of spatial cell i given by

$$\begin{aligned} \psi_{n,i+\frac{1}{2}} &= \psi_{n,i-\frac{1}{2}} e^{-|\varepsilon_{n,i}|} \\ &+ S_{A_{n,i}} \int_{x_{i-\frac{1}{2}}}^{x_{i+\frac{1}{2}}} \frac{dx'}{|\mu_n|} e^{-|\varepsilon_{n,i}| \frac{\left(x_{i+\frac{1}{2}} - x'\right)}{\Delta x_i}} \\ &+ E_{A_{n,i}} \int_{x_{i-\frac{1}{2}}}^{x_{i+\frac{1}{2}}} \frac{dx'}{|\mu_n|} e^{-|\varepsilon_{n,i}| \frac{\left(x_{i+\frac{1}{2}} - x'\right)}{\Delta x_i}}. \qquad \mu_n > 0. \end{aligned} \tag{63}$$

Similarly setting $x = x_{i+\frac{1}{2}}$ in equations and (60) produces flux exiting the left edge of spatial cell i given by

Equation (60) solved for flux exiting the left edge of spatial cell i is:

$$\psi_{n,i-\frac{1}{2}} = \psi_{n,i+\frac{1}{2}} e^{-\left|\varepsilon_{n,i}\right|}$$
$$+ S_{A_{n,i}} \int_{x_{i-\frac{1}{2}}}^{x_{i+\frac{1}{2}}} \frac{dx'}{\left|\mu_n\right|} \; e^{-\left|\varepsilon_{n,i}\right| \frac{\left(x' - x_{i-\frac{1}{2}}\right)}{\Delta x_i}} \tag{64}$$
$$+ E_{A_{n,i}} \int_{x_{i-\frac{1}{2}}}^{x_{i+\frac{1}{2}}} \frac{dx'}{\left|\mu_n\right|} \; e^{-\left|\varepsilon_{n,i}\right| \frac{\left(x' - x_{i-\frac{1}{2}}\right)}{\Delta x_i}} \quad . \qquad \mu_n < 0.$$

Introducing the following change of variables to $u' = \frac{x' - x_{i-\frac{1}{2}}}{\Delta x}$ in equations (63) and (64) results in

$$\psi_{n,i+\frac{1}{2}} = \psi_{n,i-\frac{1}{2}} e^{-\left|\varepsilon_{n,i}\right|}$$
$$+ \mathrm{S}_{\mathrm{A_{n,i}}} \frac{\Delta x}{\left|\mu_n\right|} e^{-\left|\varepsilon_{n,i}\right|} \int_0^1 du' \; e^{\left|\varepsilon_{n,i}\right| u'} \tag{65}$$
$$+ E_{A_{n,i}} \frac{\Delta x}{\left|\mu_n\right|} e^{-\left|\varepsilon_{n,i}\right|} \int_0^1 d\mu' \; e^{\left|\varepsilon_{n,i}\right| u'} \qquad \mu_n > 0$$

$$\psi_{n,i-\frac{1}{2}} = \psi_{n,i+\frac{1}{2}} e^{-\left|\varepsilon_{n,i}\right|}$$
$$+ S_{A_{n,i}} \frac{\Delta x}{\left|\mu_n\right|} \int_0^1 du' \; e^{-\left|\varepsilon_{n,i}\right| u'} \tag{66}$$
$$+ E_{A_{n,i}} \frac{\Delta x}{\left|\mu_n\right|} \int_0^1 du' \; e^{-\left|\varepsilon_{n,i}\right| u'} \qquad \mu_n < 0.$$

Evaluation of the integrals in equations (65) and (66) yields a positive scalar quantity for each transport coefficient. Practical evaluation of these integrals requires using exponential moment functions as introduced by Mathews and Minor (*11*:169). The exponential moment function of order zero with one argument is:

$$\mathcal{M}_0(x) = \int_0^1 du \, e^{-xu} = \frac{1 - e^{-x}}{x} . \tag{67}$$

The exponential moment function of order n with one argument is:

$$\mathcal{M}_n(x) = \int_0^1 dt\ (1-t)^n e^{(-xt)} = \frac{1-n\mathcal{M}_{n-1}(x)}{x}. \tag{68}$$

Using equation (67) to evaluate the integrals of equation (65) results in

$$\begin{aligned}
&\psi_{n,i+\frac{1}{2}} = \psi_{n,i-\frac{1}{2}}\, e^{-|\varepsilon_{n,i}|} \\
&+\mathrm{S}_{\mathrm{A_{n,i}}}\, \frac{\Delta x}{|\mu_n|} e^{-|\varepsilon_{n,i}|} \mathcal{M}_{\mathcal{O}}\left(-|\varepsilon_{n,i}|\right) \\
&+E_{A_{n,i}}\, \frac{\Delta x}{|\mu_n|} e^{-|\varepsilon_{n,i}|} \mathcal{M}_{\mathcal{O}}\left(-|\varepsilon_{n,i}|\right) \qquad\qquad \mu_n > 0.
\end{aligned} \tag{69}$$

Noting that

$$e^{-x}\mathcal{M}_0(-x) = e^{-x}\,\frac{1-e^x}{-x} = \mathcal{M}_0(x), \tag{70}$$

results in rewriting equation (69) as

$$\begin{aligned}
&\psi_{n,i+\frac{1}{2}} = \psi_{n,i-\frac{1}{2}}\, e^{-|\varepsilon_{n,i}|} \\
&+\mathrm{S}_{\mathrm{A_{n,i}}}\, \frac{\Delta x}{|\mu_n|} \mathcal{M}_0\left(|\varepsilon_{n,i}|\right) \\
&+E_{A_{n,i}}\, \frac{\Delta x}{|\mu_n|} \mathcal{M}_0\left(|\varepsilon_{n,i}|\right) \qquad\qquad \mu_n > 0.
\end{aligned} \tag{71}$$

Using equation (67) to evaluate the integrals of equation (66) results in

$$\begin{aligned}
&\psi_{n,i-\frac{1}{2}} = \psi_{n,i+\frac{1}{2}}\, e^{-|\varepsilon_{n,i}|} \\
&+\mathrm{S}_{\mathrm{A_{n,i}}}\, \frac{\Delta x}{|\mu_n|} \mathcal{M}_0\left(|\varepsilon_{n,i}|\right) \\
&+E_{A_{n,i}}\, \frac{\Delta x}{|\mu_n|} \mathcal{M}_0\left(|\varepsilon_{n,i}|\right) \qquad\qquad \mu_n < 0.
\end{aligned} \tag{72}$$

Equations (71) and (72) are in the form of equations (42) and (43). The spatial quadrature coefficient for the outgoing flux due to the incoming flux, K_{OI}, is obtained from yhe first term on the right of equations (71) and (72):

$$K_{OI\,n,i} = e^{-\left|\varepsilon_{n,i}\right|}. \tag{73}$$

The second transport term on the right hand side relates the contribution of flux within cell scattering to the flux exiting an edge:

$$K_{OS\,n,i} = \frac{\Delta x}{\left|\mu_n\right|}\mathcal{M}_0\left(\left|\varepsilon_{n,i}\right|\right) \tag{74}$$

The third term on the right hand side relates the contribution of cell intrinsic emissions to the flux exiting an edge:

$$K_{OE\,n,i} = \frac{\Delta x}{\left|\mu_n\right|}\mathcal{M}_0\left(\left|\varepsilon_{n,i}\right|\right). \tag{75}$$

Note that for SC, $K_{OE\,n,i} = K_{OS\,n,i}$.

The coefficients for the cell average fluxes are developed next. Equations (59) and (60) averaged over a spatial cell are:

$$\begin{aligned}
\psi_{n,i} = &\int_{x_{i-\frac{1}{2}}}^{x_{i+\frac{1}{2}}} \frac{dx}{\Delta x}\psi_{n,i-\frac{1}{2}}\, e^{-\left|\varepsilon_{n,i}\right|\frac{x-x_{i-\frac{1}{2}}}{\Delta x}} \\
&+ S_{A_{n,i}}\int_{x_{i-\frac{1}{2}}}^{x_{i+\frac{1}{2}}} \frac{dx}{\Delta x}\int_{x_{i-\frac{1}{2}}}^{x} \frac{dx'}{\left|\mu_n\right|}\, e^{-\left|\varepsilon_{n,i}\right|\frac{(x-x')}{\Delta x}} \\
&+ E_{A_{n,i}}\int_{x_{i-\frac{1}{2}}}^{x_{i+\frac{1}{2}}} \frac{dx}{\Delta x}\int_{x_{i-\frac{1}{2}}}^{x} \frac{dx'}{\left|\mu_n\right|} e^{-\left|\varepsilon_{n,i}\right|\frac{(x-x')}{\Delta x}} \qquad \mu_n > 0,
\end{aligned} \tag{76}$$

$$\psi_{n,i} = \int_{x_{i-\frac{1}{2}}}^{x_{i+\frac{1}{2}}} \frac{dx}{\Delta x} \psi_{n,i+\frac{1}{2}} \, e^{-|\varepsilon_{n,i}| \frac{x_{i+\frac{1}{2}} - x}{\Delta x}}$$
$$+ S_{A_{n,i}} \int_{x_{i-\frac{1}{2}}}^{x_{i+\frac{1}{2}}} \frac{dx}{\Delta x} \int_{x}^{x_{i+\frac{1}{2}}} \frac{dx'}{|\mu_n|} \, e^{-|\varepsilon_{n,i}| \frac{(x'-x)}{\Delta x}} \tag{77}$$
$$+ E_{A_n} \int_{x_{i-\frac{1}{2}}}^{x_{i+\frac{1}{2}}} \frac{dx}{\Delta x} \int_{x}^{x_{i+\frac{1}{2}}} \frac{dx'}{|\mu_n|} \, e^{-|\varepsilon_{n,i}| \frac{(x'-x)}{\Delta x}} \qquad \mu_n < 0.$$

Using the change of variables $u = \frac{x - x_{i-\frac{1}{2}}}{\Delta x}$, and $u' = \frac{x' - x_{i-\frac{1}{2}}}{\Delta x}$ for equation (76) then rearranging terms results in

$$\psi_{n,i} = \int_0^1 du \, \psi_{n,i-\frac{1}{2}} \, e^{-|\varepsilon_{n,i}| u}$$
$$+ S_{A_{n,i}} \frac{\Delta x}{|\mu_n|} \int_0^1 du \, e^{-|\varepsilon_{n,i}| u} \int_0^u du' \, e^{|\varepsilon_{n,i}| u'} \tag{78}$$
$$+ E_{A_{n,i}} \frac{\Delta x}{|\mu_n|} \int_0^1 du \, e^{-|\varepsilon_{n,i}| u} \int_0^u du' e^{|\varepsilon_{n,i}| u'} \qquad \mu_n > 0.$$

Using equation (67) to evaluate the first term of equation (78) and evaluating the right most integral of the second and third terms of equation (78) results in

$$\psi_{n,i} = \psi_{n,i-\frac{1}{2}} \mathcal{M}_0 \left(|\varepsilon_{n,i}| \right)$$
$$+ S_{A_{n,i}} \frac{\Delta x}{|\mu_n|} \frac{1}{|\varepsilon_{n,i}|} \int_0^1 du \left(1 - e^{-|\varepsilon_{n,i}| u} \right) \tag{79}$$
$$+ E_{A_{n,i}} \frac{\Delta x}{|\mu_n|} \frac{1}{|\varepsilon_{n,i}|} \int_0^1 du \left(1 - e^{-|\varepsilon_{n,i}| u} \right) \qquad \mu_n > 0.$$

Using equation (67) to evaluate the remaining integral in the second and third terms results in

$$\begin{aligned}\psi_{n,i} &= \psi_{n,i-\frac{1}{2}} \mathcal{M}_0\left(\left|\varepsilon_{n,i}\right|\right) \\ &+ S_{A_{n,i}} \frac{\Delta x}{\left|\mu_n\right|}\left(\frac{1-\mathcal{M}_0\left(\left|\varepsilon_{n,i}\right|\right)}{\left|\varepsilon_{n,i}\right|}\right) \\ &+ E_{A_{n,i}} \frac{\Delta x}{\left|\mu_n\right|}\left(\frac{1-\mathcal{M}_0\left(\left|\varepsilon_{n,i}\right|\right)}{\left|\varepsilon_{n,i}\right|}\right) \qquad \mu_n > 0.\end{aligned} \tag{80}$$

Substituting equation (68) where appropriate in equation (80) results in

$$\begin{aligned}\psi_{n,i} &= \psi_{n,i-\frac{1}{2}} \mathcal{M}_0\left(\left|\varepsilon_{n,i}\right|\right) \\ &+ S_{A_{n,i}} \frac{\Delta x}{\left|\mu_n\right|} \mathcal{M}_1\left(\left|\varepsilon_{n,i}\right|\right) \\ &+ E_{A_{n,i}} \frac{\Delta x}{\left|\mu_n\right|} \mathcal{M}_1\left(\left|\varepsilon_{n,i}\right|\right) \qquad \mu_n > 0.\end{aligned} \tag{81}$$

Using the change of variables $u = \frac{x - x_{i-\frac{1}{2}}}{\Delta x}$, and $u' = \frac{x' - x_{i+\frac{1}{2}}}{\Delta x}$ for equation (77) then rearranging terms results in

$$\begin{aligned}\psi_{n,i} &= \int_0^1 du\ \psi_{n,i+\frac{1}{2}}\, e^{-\left|\varepsilon_{n,i}\right|(1-u)} \\ &+ S_{A_{n,i}} \frac{\Delta x}{\left|\mu_n\right|} \int_0^1 du\, e^{\left|\varepsilon_{n,i}\right|u} e^{-\left|\varepsilon_{n,i}\right|} \int_{u-1}^0 du'\, e^{-\left|\varepsilon_{n,i}\right|u'} \\ &+ E_{A_{n,i}} \int_0^1 du\, e^{\left|\varepsilon_{n,i}\right|u} e^{-\left|\varepsilon_{n,i}\right|} \int_{u-1}^0 du'\, e^{-\left|\varepsilon_{n,i}\right|u'} \qquad \mu_n < 0.\end{aligned} \tag{82}$$

Using equation (67) to evaluate the first term of equation (82) and evaluating the inner integrals of equation (82) results in

$$\begin{aligned}\psi_{n,i} &= \psi_{n,i+\frac{1}{2}} \mathcal{M}_0\left(\left|\varepsilon_{n,i}\right|\right) \\ &+ S_{A_{n,i}} \frac{\Delta x}{\left|\mu_n\right|} \frac{1}{\left|\varepsilon_{n,i}\right|} \int_0^1 du \left(e^{-\left|\varepsilon_{n,i}\right|u} - e^{-\left|\varepsilon_{n,i}\right|}\right) \\ &+ E_{A_n} \frac{\Delta x}{\left|\mu_n\right|} \frac{1}{\left|\varepsilon_{n,i}\right|} \int_0^1 du \left(e^{-\left|\varepsilon_{n,i}\right|u} - e^{-\left|\varepsilon_{n,i}\right|}\right) \qquad \mu_n < 0.\end{aligned} \tag{83}$$

Using equation (67) and equation (70) to evaluate the remaining integral of equation (83) results in

$$\begin{aligned}\psi_{n,i} &= \psi_{n,i+\frac{1}{2}} \mathcal{M}_0\left(\left|\varepsilon_{n,i}\right|\right) \\ &+ S_{A_{n,i}} \frac{\Delta x}{\left|\mu_n\right|}\left(\frac{1-\mathcal{M}_0\left(\left|\varepsilon_{n,i}\right|\right)}{\left|\varepsilon_{n,i}\right|}\right) \\ &+ E_{A_n} \frac{\Delta x}{\left|\mu_n\right|}\left(\frac{1-\mathcal{M}_0\left(\left|\varepsilon_{n,i}\right|\right)}{\left|\varepsilon_{n,i}\right|}\right) \qquad \mu_n < 0.\end{aligned} \tag{84}$$

Substituting equation (68) where appropriate in equation (80) results in

$$\begin{aligned}\psi_{n,i} &= \psi_{n,i+\frac{1}{2}} \mathcal{M}_0\left(\left|\varepsilon_{n,i}\right|\right) \\ &+ S_{A_{n,i}} \frac{\Delta x}{\left|\mu_n\right|} \mathcal{M}_1\left(\left|\varepsilon_{n,i}\right|\right) \\ &+ E_{A_{n,i}} \frac{\Delta x}{\left|\mu_n\right|} \mathcal{M}_1\left(\left|\varepsilon_{n,i}\right|\right) \qquad \mu_n < 0.\end{aligned} \tag{85}$$

Equation (81) and equation (85) are again in the form of equation (44) and equation (45). The fourth transport coefficient relates the contribution of cell entering edge flux to cell average flux it is

$$K_{AI_{n,i}} = \mathcal{M}_O\left(\left|\varepsilon_{n,i}\right|\right). \tag{86}$$

The fifth transport coefficient relates the contribution of cell scattered flux to cell average flux. It is

$$K_{AS_{n,i}} = \frac{\Delta x}{\left|\mu_n\right|} \mathcal{M}_1\left(\left|\varepsilon_{n,i}\right|\right). \tag{87}$$

The sixth transport coefficient relates the contribution of cell intrinsic emissions to cell average flux. It is

$$K_{AE_{n,i}} = \frac{\Delta x}{|\mu_n|} \mathcal{M}_1 \left(|\varepsilon_{n,i}| \right). \tag{88}$$

Note that for SC $K_{AS_{n,i}} = K_{AE_{n,i}}$.

The spatial quadrature coefficients in this section are derived for SC. A similar procedure is followed with other spatial quadratures which result in different formulas for the spatial quadrature coefficients that also can be put in the form of equations (42) and (43). The use of these coefficients in the ASDI method is general and applicable to coefficients derived from any spatial quadrature.

Explicit Solution of Transport Equations for N Directions Coupled in Space

The cell transport equations; (63), (64),(76), (77), written in vector notation are

$$\vec{\psi}_{out_i} = \mathbf{K}_{OI_i} \vec{\psi}_{in_i} + \mathbf{K}_{OS_i} \vec{S}_{A_i} + \mathbf{K}_{OE_i} \vec{E}_{A_i}, \tag{89}$$

$$\vec{\psi}_{A_i} = \mathbf{K}_{AI_i} \vec{\psi}_{in_i} + \mathbf{K}_{AS_i} \vec{S}_{A_i} + \mathbf{K}_{AE_i} \vec{E}_{A_i}, \tag{90}$$

$$\vec{S}_{A_i} = \mathbf{\Sigma}_{S_i} \vec{\psi}_{A_i}, \tag{91}$$

where bold type denotes a matrix, $\vec{}$ denotes a vector, and i denotes a cell number. If the total number of ordinates is denoted by N, the ordinate set is $\left\{ \mu_1, \mu_2, \cdots, \mu_{N_R}, \mu_{N_{R+1}}, \cdots \mu_N \right\}$. Denoting the rightward, $\mu_n > 0$, ordinates as

$\left\{\mu_1, \mu_2, \cdots, \mu_{N_R}\right\}$, N_R is the number of rightward directions. The leftward, $\mu_n < 0$, ordinates are $\left\{\mu_{N_{R+1}}, \cdots \mu_N\right\}$. The number of leftward directions is

$$N_L = N - N_R . \tag{92}$$

The inward flux vector in cell i ($\vec{\psi}_{in_i}$) has N components

$$\vec{\psi}_{in_i} = \begin{bmatrix} \psi_{1,i-\frac{1}{2}} \\ \vdots \\ \psi_{N_R,i-\frac{1}{2}} \\ \psi_{N_R+1,i+\frac{1}{2}} \\ \vdots \\ \psi_{N,i+\frac{1}{2}} \end{bmatrix}. \tag{93}$$

The top set of angular fluxes in equation (93) represent the flux in at the left edge of cell i streaming in the rightward direction, $\left\{\psi_{1,i-\frac{1}{2}} \ldots \psi_{N_R,i-\frac{1}{2}}\right\}$, and the bottom set represent flux in at the right streaming in the leftward direction in cell i $\left\{\psi_{N_R+1,i+\frac{1}{2}} \cdots \psi_{N,i+\frac{1}{2}}\right\}$.

The outward flux vector in cell i ($\vec{\psi}_{out_i}$) has N components

$$\vec{\psi}_{out_i} = \begin{bmatrix} \psi_{1,i+\frac{1}{2}} \\ \vdots \\ \psi_{N_R,i+\frac{1}{2}} \\ \psi_{N_R+1,i-\frac{1}{2}} \\ \vdots \\ \psi_{N,i-\frac{1}{2}} \end{bmatrix}. \tag{94}$$

The top set of angular fluxes in equation (94) represent the flux out at the right edge of cell i streaming in the rightward direction, $\left\{\psi_{1,i+\frac{1}{2}} \cdots \psi_{N_R,i+\frac{1}{2}}\right\}$, and the bottom set represent flux out at the left edge of cell i streaming in the leftward direction $\left\{\psi_{N_R+1,i-\frac{1}{2}} \cdots \psi_{N,i-\frac{1}{2}}\right\}$.

Equation (93) can be written even more compactly as

$$\vec{\psi}_{in_i} = \begin{bmatrix} \vec{\psi}_{in\,R_i} \\ \vec{\psi}_{in\,L_i} \end{bmatrix}, \tag{95}$$

where

$$\vec{\psi}_{in_{R_i}} = \begin{bmatrix} \psi_{1,i-\frac{1}{2}} \\ \vdots \\ \psi_{N_R,i-\frac{1}{2}} \end{bmatrix}, \tag{96}$$

and

$$\vec{\psi}_{in_{L_i}} = \begin{bmatrix} \psi_{N_R+1,i+\frac{1}{2}} \\ \vdots \\ \psi_{N,i+\frac{1}{2}} \end{bmatrix}. \tag{97}$$

Similarly equation (94) can be written

$$\vec{\psi}_{out_i} = \begin{bmatrix} \vec{\psi}_{out\,R_i} \\ \vec{\psi}_{out\,L_i} \end{bmatrix}, \tag{98}$$

where

$$\vec{\psi}_{out_{R_i}} = \begin{bmatrix} \psi_{1,i+\frac{1}{2}} \\ \vdots \\ \psi_{N_R,i+\frac{1}{2}} \end{bmatrix}, \tag{99}$$

and

$$\vec{\psi}_{out_{L_i}} = \begin{bmatrix} \psi_{N_R+1,i-\frac{1}{2}} \\ \vdots \\ \psi_{N,i-\frac{1}{2}} \end{bmatrix}. \tag{100}$$

The average intrinsic emission vector in cell i ($\vec{E}_{A_i}$) has N components. Written in compact notation it is

$$\vec{E}_{A_i} = \begin{bmatrix} \vec{E}_{A_{R,i}} \\ \vec{E}_{A_{L,i}} \end{bmatrix}, \tag{101}$$

where

$$\vec{E}_{A_{R_i}} = \begin{bmatrix} E_{A_{1,i}} \\ \vdots \\ E_{A_{N_R,i}} \end{bmatrix}, \tag{102}$$

and

$$\vec{E}_{A_{L_i}} = \begin{bmatrix} E_{A_{N_{R+1},i}} \\ \vdots \\ E_{A_{N,i}} \end{bmatrix}. \tag{103}$$

The coefficient matrix denoting the contribution to the outgoing fluxes from the incoming fluxes in cell i is a diagonal matrix of size NxN:

$$\mathbf{K}_{OI_i} = \begin{bmatrix} K_{OI_{1,i}} & 0 & 0 & 0 \\ 0 & K_{OI_{2,i}} & 0 & 0 \\ 0 & 0 & \ddots & 0 \\ 0 & 0 & 0 & K_{OI_{N,i}} \end{bmatrix}. \tag{104}$$

The other transport coefficient matrices $\mathbf{K}_{AI_i}, \mathbf{K}_{OS_i}, \mathbf{K}_{AS_i}, \mathbf{K}_{AE_i}, \mathbf{K}_{OE_i}$, have the same form as equation(104). They are diagonal matrices of their corresponding spatial quadrature coefficients.

The matrix $\mathbf{\Sigma}_{s_i}$ contains the element-to-element scattering cross sections, or the ordinate-to-ordinate scattering cross sections and weights:

$$\mathbf{\Sigma}_{s_i} = \begin{bmatrix} \sigma_{s_{1\to 1,i}} w_1 & \sigma_{s_{2\to 1,i}} w_2 & \cdots & \sigma_{s_{N\to 1,i}} w_N \\ \sigma_{s_{1\to 2,i}} w_1 & \sigma_{s_{2\to 2,i}} w_2 & \cdots & \sigma_{s_{N\to 2,i}} w_N \\ \vdots & \cdots & \ddots & \vdots \\ \sigma_{s_{1\to N,i}} w_1 & \sigma_{s_{2\to N,i}} w_2 & \cdots & \sigma_{s_{N\to N,i}} w_N \end{bmatrix}. \tag{105}$$

The following matrices are useful for stripping the rightward or leftward components of the vectors introduced

$$\mathbf{I}_{\mathrm{R}} = \begin{bmatrix} \mathbf{I}_{N_R} & \mathbf{0} \\ \mathbf{0} & \mathbf{0} \end{bmatrix}, \tag{106}$$

$$\mathbf{I}_L = \begin{bmatrix} \mathbf{0} & \mathbf{0} \\ \mathbf{0} & \mathbf{I}_{N_L} \end{bmatrix}, \tag{107}$$

where $\mathbf{I}_{N_R}$ and $\mathbf{I}_{N_L}$ are identity matrices of dimension N_R and N_L respectively, and $\mathbf{0}$ represents a matrix of zeros of appropriate dimensions. As an example of how these matrices are used I will rewrite equation (98) in terms of the outgoing flux from the two cells adjacent to cell i. Using equation (106) and equation (107) results in

$$\begin{bmatrix} \vec{\psi}_{out_{R_i}} \\ \vec{\psi}_{out_{L_i}} \end{bmatrix} = \begin{bmatrix} \mathbf{I}_{\mathbf{N_R}} & \mathbf{0} \\ \mathbf{0} & \mathbf{0} \end{bmatrix} \begin{bmatrix} \vec{\psi}_{out_{R_i}} \\ \vec{\psi}_{out_{L_i}} \end{bmatrix} + \begin{bmatrix} \mathbf{0} & \mathbf{0} \\ \mathbf{0} & \mathbf{I}_{\mathbf{N}_L} \end{bmatrix} \begin{bmatrix} \vec{\psi}_{out_{R_i}} \\ \vec{\psi}_{out_{L_i}} \end{bmatrix} . \tag{108}$$

An explicit solution of the discrete ordinates equations, (89) and, (90) is possible. First consider cells that are not on either the left or right exterior boundaries so that particles stream into the cell from the adjacent cell on each side and particles stream out of the cell into those cells. Substituting equation (91) into equation (89) and (90) results in

$$\vec{\psi}_{out_i} = \mathbf{K}_{OI_i} \vec{\psi}_{in_i} + \mathbf{K}_{OS_i} \boldsymbol{\Sigma}_{S_i} \vec{\psi}_{A_i} + \mathbf{K}_{OE_i} \vec{\bar{E}}_{A_i}, \tag{109}$$

$$\vec{\psi}_{A_i} = \mathbf{K}_{AI_i} \vec{\psi}_{in_i} + \mathbf{K}_{AS_i} \boldsymbol{\Sigma}_{S_i} \vec{\psi}_{A_i} + \mathbf{K}_{AE_i} \vec{\bar{E}}_{A_i}. \tag{110}$$

The formal solution of equation (110) for $\vec{\psi}_{A_i}$ results in

$$\vec{\psi}_{A_i} = (I - \mathbf{K}_{AS_i} \boldsymbol{\Sigma}_{S_i})^{-1} \mathbf{K}_{AI_i} \vec{\psi}_{in_i} + (I - \mathbf{K}_{AS_i} \boldsymbol{\Sigma}_{S_i})^{-1} \mathbf{K}_{AE_i} \vec{\bar{E}}_{A_i}. \tag{111}$$

Substituting equation (111) into equation (109) with some rearrangement results in

$$\begin{aligned} \vec{\psi}_{out_i} = &\left(\mathbf{K}_{OI_i} + \mathbf{K}_{OS_i} \boldsymbol{\Sigma}_{S_i} (I - \mathbf{K}_{AS_i} \boldsymbol{\Sigma}_{S_i})^{-1} \mathbf{K}_{AI_i} \right) \vec{\psi}_{in_i} \\ &+ \left(\mathbf{K}_{OE_i} + \mathbf{K}_{OS_i} \boldsymbol{\Sigma}_{S_i} (I - \mathbf{K}_{AS_i} \boldsymbol{\Sigma}_{S_i})^{-1} \mathbf{K}_{AE_i} \right) \vec{\bar{E}}_{A_i}. \end{aligned} \tag{112}$$

This may be written more compactly as

$$\vec{\psi}_{out_i} = \mathbf{m}_{OI_i} \vec{\psi}_{in_i} + \mathbf{m}_{OE_i} \vec{\bar{E}}_{A_i}, \tag{113}$$

where

$$\mathbf{m}_{OI_i} = \left(\mathbf{K}_{OI_i} + \mathbf{K}_{OS_i} \boldsymbol{\Sigma}_{S_i} (I - \mathbf{K}_{AS_i} \boldsymbol{\Sigma}_{S_i})^{-1} \mathbf{K}_{AI_i} \right), \tag{114}$$

and

$$\mathbf{m}_{OE_i} = \left(\mathbf{K}_{OE_i} + \mathbf{K}_{OS_i} \boldsymbol{\Sigma}_{S_i} (I - \mathbf{K}_{AS_i} \boldsymbol{\Sigma}_{S_i})^{-1} \mathbf{K}_{AE_i} \right). \tag{115}$$

I will refer to the elements of the matrices $\mathbf{m}_{OI_i}$ and $\mathbf{m}_{OE_i}$ as cell transport coefficients. The flux entering at the left of cell i moving rightward is $\left(\vec{\psi}_{in_i}\right)_{n' \le N_R}$. The flux exiting at the right of cell i moving rightward is $\left(\vec{\psi}_{out_i}\right)_{n \le N_R}$. The fraction of flux entering at the left ($\mu_n > 0$) and leaving at right ($\mu_n > 0$) is $\left(\mathbf{m}_{OI_i}\right)_{n,n'}$

Using equation (108), equation (113) can be written

$$\vec{\psi}_{out_i} = \mathbf{m}_{OI_i}(\mathbf{I}_R).\vec{\psi}_{out_{i-1}} + \mathbf{m}_{OI_i}(\mathbf{I}_L).\vec{\psi}_{out_{i+1}} + \mathbf{m}_{OE_i}\vec{E}_{A_i}. \tag{116}$$

Equation (113) expresses the outgoing edge flux for a mesh cell ($\vec{\psi}_{out_i}$) in terms of cell emission ($\vec{E}_{A_i}$) and outgoing edge flux from the two adjacent cells. The coefficient matrix $\mathbf{m}_{OI_i}$ determines the contribution to cell outgoing flux from cell incoming flux. The coefficient matrix $\mathbf{m}_{OE_i}$ determines the contribution to cell outgoing flux from cell intrinsic emission.

Next consider cells at the left or right boundaries. If a cell is at an exterior boundary, particles stream into the cell from one adjacent cell and particles behave in accordance with a boundary condition on the other side. The reflection condition for this boundary condition for any discrete ordinates set can be represented as a matrix. This matrix is denoted by $\boldsymbol{\alpha}_L$ on the left boundary and $\boldsymbol{\alpha}_R$ on the right boundary. Each element of the matrix represents the fraction of flux from an outgoing ordinate that is reflected into an incoming ordinate. Defining these boundary matrices as

$$\boldsymbol{\alpha}_L = \begin{bmatrix} 0 & \cdots & 0 & \alpha_{L_{1,N_R+1}} & \cdots & \alpha_{L_{1,N}} \\ \vdots & \ddots & \vdots & \vdots & \cdots & \vdots \\ 0 & \cdots & 0 & \alpha_{L_{N_R,N_R+1}} & \cdots & \alpha_{L_{N_R,N_R}} \\ 0 & \cdots & 0 & 0 & \cdots & 0 \\ \vdots & \ddots & \vdots & \vdots & \ddots & \vdots \\ 0 & \cdots & 0 & 0 & \cdots & 0 \end{bmatrix}, \tag{117}$$

$$\boldsymbol{\alpha}_R = \begin{bmatrix} 0 & \cdots & 0 & 0 & \cdots & 0 \\ \vdots & \ddots & \vdots & \vdots & \ddots & \vdots \\ 0 & \cdots & 0 & 0 & \cdots & 0 \\ \alpha_{R_{N_R+1,1}} & \cdots & \alpha_{R_{N_R+1,N_R}} & 0 & \cdots & 0 \\ \vdots & \ddots & \vdots & \vdots & \ddots & \vdots \\ \alpha_{R_{N,1}} & \cdots & \alpha_{R_{N,N_R}} & 0 & \cdots & 0 \end{bmatrix}, \tag{118}$$

facilitates specification of all but periodic boundaries. In block form these boundary matrices are:

$$\boldsymbol{\alpha}_L = \begin{bmatrix} \mathbf{0} & \boldsymbol{\alpha}_\ell \\ \mathbf{0} & \mathbf{0} \end{bmatrix}, \tag{119}$$

where

$$\boldsymbol{\alpha}_\ell = \begin{bmatrix} \alpha_{L_{1,N_R+1}} & \cdots & \alpha_{L_{1,N}} \\ \vdots & \ddots & \\ \alpha_{L_{N,N_R+1}} & \cdots & \alpha_{L_{N,N}} \end{bmatrix}, \tag{120}$$

and

$$\boldsymbol{\alpha}_R = \begin{bmatrix} \mathbf{0} & \mathbf{0} \\ \boldsymbol{\alpha}_r & \mathbf{0} \end{bmatrix}, \tag{121}$$

where

$$\boldsymbol{\alpha}_{\mathrm{R}} = \begin{bmatrix} \alpha_{R_{N_R+1,1}} & \cdots & \alpha_{R_{N_R+1,N}} \\ \vdots & \ddots & \\ \alpha_{R_{N,1}} & \cdots & \alpha_{R_{N,N}} \end{bmatrix}. \tag{122}$$

Consider a problem without incident flux, cell 1 which is at the left boundary has as an incident flux on the left side the flux resulting from the above boundary condition rather than the inward flux denoted in equation (93). Using the above boundary condition this inward flux at the left boundary ($\vec{\psi}_{in_1}$) is written:

$$\vec{\psi}_{in_1} = \begin{bmatrix} \sum_{n'=NR+1}^{N} \alpha_{L_{n',1}} \psi_{n',\frac{1}{2}} \\ \vdots \\ \sum_{n'=NR+1}^{N} \alpha_{L_{n',N_R}} \psi_{n',\frac{1}{2}} \\ \psi_{N_R+1,\frac{3}{2}} \\ \vdots \\ \psi_{N,\frac{3}{2}} \end{bmatrix}. \tag{123}$$

Equation (123) can be rearranged as

$$\vec{\psi}_{in,1} = \begin{bmatrix} \sum_{n'=N_R+1}^{N} \alpha_{L_{n',1}} \psi_{n',\frac{1}{2}} \\ \vdots \\ \sum_{n'=N_R+1}^{N} \alpha_{L_{n',N_R}} \psi_{n',\frac{1}{2}} \\ 0 \\ \vdots \\ 0 \end{bmatrix} + \begin{bmatrix} 0 \\ \vdots \\ 0 \\ \psi_{N_R+1,\frac{3}{2}} \\ \vdots \\ \psi_{N,\frac{3}{2}} \end{bmatrix} \tag{124}$$

Equation (124) represents the inward flux of the left boundary as the contribution to the cell flux from the left side boundary reflection and particles streaming in from the right adjacent cell. In compact matrix notation this is

$$\vec{\psi}_{in_1} = \boldsymbol{\alpha}_L \cdot \vec{\psi}_{out_1} + \mathbf{I}_L \cdot \vec{\psi}_{in_1} . \tag{125}$$

In any spatial discretization scheme adjacent cells are coupled at the edge that is shared by the two cells. This adjacent cell coupling for cells one and two for the leftward streaming flux is expressed as:

$$\mathbf{I}_L \vec{\psi}_{in_1} = \mathbf{I}_L \vec{\psi}_{out_2} . \tag{126}$$

With this expression (125) can be written

$$\vec{\psi}_{in_1} = \boldsymbol{\alpha}_L \vec{\psi}_{out_1} + \mathbf{I}_L \vec{\psi}_{out_2} . \tag{127}$$

Substituting equations (127) into equation(113), and applying the left side boundary condition results in

$$\vec{\psi}_{out_1} = \mathbf{m}_{OI_1} \boldsymbol{\alpha}_L \vec{\psi}_{out_1} + \mathbf{m}_{OI_1} \mathbf{I}_L \vec{\psi}_{out_2} + \mathbf{m}_{OE_1} \vec{E}_{A_1} . \tag{128}$$

Rearranging terms in equation (128) results in

$$\left(\mathbf{I} - \mathbf{m}_{OI_1} \boldsymbol{\alpha}_L\right) \vec{\psi}_{out_1} = \mathbf{m}_{OI_1} \mathbf{I}_L \vec{\psi}_{out_2} + \mathbf{m}_{OE_1} \vec{E}_{A_1} . \tag{129}$$

The right most (I^{th}) cell in the spatial domain is handled in the same way resulting in:

$$\left(\mathbf{I} - \mathbf{m}_{OI_I} \boldsymbol{\alpha}_R\right) \vec{\psi}_{out_I} = \mathbf{m}_{OI_I} \mathbf{I}_R \vec{\psi}_{out_{I-1}} + \mathbf{m}_{OE_I} \vec{E}_{A_I} . \tag{130}$$

The system represented by equation (116) has $2N$ equations in $2NI$ unknowns corresponding with interior cells. Equations (129) and (130) each represent N equations and N unknowns corresponding to the two cells on the boundaries. There appears to be more unknowns than equations until one considers the connectivity of the mesh cells. This connectivity results from the edges shared by adjacent cells. For an

interior cell the incoming edge flux is the outgoing edge flux from the adjacent cell. This leads to N connectivity equations for the (I-2) interior cells

$$\mathbf{I}_R.\vec{\psi}_{in_i} = \mathbf{I}_R.\vec{\psi}_{out_{i-1}} \qquad i = \{2,\ldots,I\}, \tag{131}$$

$$\mathbf{I}_L.\vec{\psi}_{in_i} = \mathbf{I}_L.\vec{\psi}_{out_{i+1}} \qquad i = \{1,\ldots,I-1\}. \tag{132}$$

Note that the incoming edge fluxes on any cell edge can be written as the sum of the outgoing edge fluxes from two adjacent cells.

On the left boundary in cell 1, flux enters from edge $i = 1/2$ and from edge $i = 3/2$. The incoming flux in cell 1 at edge $i = 1/2$ is the outgoing flux at this same edge reflected back in the incoming direction. The incoming flux in cell 1 at edge i = 3/2 is the outgoing edge flux from cell 2. In cell 1 there are N/2 connectivity equations and N/2 boundary equations. Likewise the right edge incoming flux is the outgoing flux reflected at the boundary at edge $i = I + 1/2$ and from the adjacent upstream cell i = I-1/2. In cell I there are N/2 connectivity equations and N/2 boundary equations. The boundary cells contribute N connectivity equations and N boundary equations to the spatially coupled system. Collectively there are $2NI$ unknowns and $2NI$ equations.

A particle transport system of equations that connects all the interior cells with the boundary cells and couples all directions represents fully coupled discrete ordinates transport. This angular and spatially coupled system of transport equations can be written in the following way. Let $\vec{\Psi}_{in}$ represent incoming flux vectors for the cells in a spatial mesh of I cells with a phantom cell on the left side and a phantom cell on the right side. This vector has 2 N (I+1) components and is written

$$\vec{\Psi}_{in} = \begin{bmatrix} \vec{\psi}_{in_0} \\ \vec{\psi}_{in_1} \\ \vdots \\ \vec{\psi}_{in_I} \\ \vec{\psi}_{in_{I+1}} \end{bmatrix}. \tag{133}$$

Let $\overline{\overline{\Psi}}_{out}$ represent outgoing flux vectors for the same mesh:

$$\overline{\overline{\Psi}}_{out} = \begin{bmatrix} \vec{\psi}_{out_0} \\ \vec{\psi}_{out_1} \\ \vdots \\ \vec{\psi}_{out_I} \\ \vec{\psi}_{out_{I+1}} \end{bmatrix}. \tag{134}$$

Let $\overline{\vec{E}}_A$ represent average intrinsic emission vectors for the same mesh, it is written:

$$\overline{\vec{E}}_A = \begin{bmatrix} 0 \\ \vec{E}_{A_1} \\ \vdots \\ \vec{E}_{A_I} \\ 0 \end{bmatrix}. \tag{135}$$

The zeros at the top and bottom of the emission vector of equation (135) represent left and right phantom cells which do not emit. In equation (133) $\vec{\psi}_{in_0}$, $\vec{\psi}_{out_0}$ represent the flux entering or exiting a phantom cell at the left boundary, $\vec{\psi}_{in_{I+1}}$, $\vec{\psi}_{out_{I+1}}$ represent the flux entering, or exiting a phantom cell at the right boundary. Flux enters and leaves these phantom cells through a single edge. Using equations (93) through (100) these arrays can be written

$$\vec{\psi}_{in_0} = \begin{bmatrix} \boldsymbol{0} \\ \vec{\psi}_{L_{out_1}} \end{bmatrix}, \tag{136}$$

$$\vec{\psi}_{out_0} = \begin{bmatrix} \vec{\psi}_{R_{in_1}} \\ \boldsymbol{0} \end{bmatrix}, \tag{137}$$

$$\vec{\psi}_{in_{I+1}} = \begin{bmatrix} \vec{\psi}_{R_{out_I}} \\ \boldsymbol{0} \end{bmatrix}, \tag{138}$$

$$\vec{\psi}_{out_{I+1}} = \begin{bmatrix} \boldsymbol{0} \\ \vec{\psi}_{L_{out_{I+1}}} \end{bmatrix}, \tag{139}$$

where $\boldsymbol{0}$ is a vector of zeros of length N_R or N_L. Because the incoming edge flux for interior mesh cells is the outgoing edge flux from an adjacent cell, ψ_{in_i} can be expressed as a combination $\psi_{out_{i-1}}, \psi_{out_{i+1}}$. Using the matrices specified by equation (106) and equation (107) ψ_{in_i} is written

$$\vec{\psi}_{in_i} = \begin{bmatrix} \mathbf{I}_R & \mathbf{0} \\ \mathbf{0} & \mathbf{I}_L \end{bmatrix} \begin{bmatrix} \vec{\psi}_{R_{out_{i-1}}} \\ \vec{\psi}_{L_{out_{i+1}}} \end{bmatrix}. \tag{140}$$

The phantom cell incoming flux at the left edge is written

$$\vec{\psi}_{in_0} = \begin{bmatrix} \mathbf{0} & \mathbf{0} \\ \mathbf{0} & \mathbf{I}_{\mathbf{N_L}} \end{bmatrix} \begin{bmatrix} \mathbf{0} \\ \vec{\psi}_{L_{out_1}} \end{bmatrix}. \tag{141}$$

The phantom cell incoming flux at the right edge is written

$$\vec{\psi}_{in_{I+1}} = \begin{bmatrix} \mathbf{I}_{\mathbf{N}_R} & \mathbf{0} \\ \mathbf{0} & \mathbf{0} \end{bmatrix} \begin{bmatrix} \vec{\psi}_{R_{out_I}} \\ \mathbf{0} \end{bmatrix}. \tag{142}$$

and $\vec{\psi}_{out_i}$ is written

$$\vec{\psi}_{out_i} = \begin{bmatrix} \mathbf{I}_R & \mathbf{0} \\ \mathbf{0} & \mathbf{I}_L \end{bmatrix} \begin{bmatrix} \vec{\psi}_{R_{in_{i+1}}} \\ \vec{\psi}_{L_{in_{i-1}}} \end{bmatrix}. \tag{143}$$

The phantom cell outgoing flux at the left edge is written

$$\vec{\psi}_{out_0} = \begin{bmatrix} \mathbf{I}_{\mathbf{N}_R} & \mathbf{0} \\ \mathbf{0} & \mathbf{0} \end{bmatrix} \begin{bmatrix} \vec{\psi}_{R_{in_1}} \\ \mathbf{0} \end{bmatrix}. \tag{144}$$

The phantom cell outgoing flux at the right edge is written

$$\vec{\psi}_{out_{I+1}} = \begin{bmatrix} \mathbf{0} & \mathbf{0} \\ \mathbf{0} & \mathbf{I}_{\mathbf{N}_L} \end{bmatrix} \begin{bmatrix} \mathbf{0} \\ \vec{\psi}_{L_{in_I}} \end{bmatrix}. \tag{145}$$

Using equations (140) through (145) the global spatial vector $\overline{\Psi}_{in}$ can be written in terms of the global spatial vector $\overline{\Psi}_{out}$:

$$\begin{bmatrix} \mathbf{0} \\ \vec{\psi}_{L_{in_0}} \\ \vec{\psi}_{R_{in_1}} \\ \vec{\psi}_{L_{in_1}} \\ \vec{\psi}_{R_{in2}} \\ \vec{\psi}_{L_{in_2}} \\ \\ \\ \vec{\psi}_{R_{in_{I-1}}} \\ \vec{\psi}_{L_{in_{I-1}}} \\ \vec{\psi}_{R_{in_I}} \\ \vec{\psi}_{L_{in_I}} \\ \vec{\psi}_{R_{in_{I+1}}} \\ \mathbf{0} \end{bmatrix} = \begin{bmatrix} \mathbf{0} & \mathbf{0} & \mathbf{0} & \mathbf{0} & \mathbf{0} & \mathbf{0} & \mathbf{0} & \mathbf{0} & \cdots & \mathbf{0} & \mathbf{0} & \mathbf{0} & \mathbf{0} \\ \mathbf{0} & \mathbf{0} & \mathbf{0} & \mathbf{I}_{N_{\mathbf{L}}} & \mathbf{0} & \mathbf{0} & \mathbf{0} & \mathbf{0} & \cdots & \mathbf{0} & \mathbf{0} & \mathbf{0} & \mathbf{0} \\ \mathbf{I}_{N_{\mathbf{R}}} & \mathbf{0} & \mathbf{0} & \mathbf{0} & \mathbf{0} & \mathbf{0} & \mathbf{0} & \mathbf{0} & \cdots & \mathbf{0} & \mathbf{0} & \mathbf{0} & \mathbf{0} \\ \mathbf{0} & \mathbf{0} & \mathbf{0} & \mathbf{0} & \mathbf{0} & \mathbf{I}_{N_{\mathbf{L}}} & \mathbf{0} & \mathbf{0} & \cdots & \mathbf{0} & \mathbf{0} & \mathbf{0} & \mathbf{0} \\ \mathbf{0} & \mathbf{0} & \mathbf{I}_{N_{\mathbf{R}}} & \mathbf{0} & \mathbf{0} & \mathbf{0} & \mathbf{0} & \mathbf{0} & \cdots & \mathbf{0} & \mathbf{0} & \mathbf{0} & \mathbf{0} \\ \mathbf{0} & \mathbf{0} & \mathbf{0} & \mathbf{0} & \mathbf{0} & \mathbf{0} & \mathbf{0} & \mathbf{I}_{\mathbf{N}_{\mathbf{L}}} & \cdots & \mathbf{0} & \mathbf{0} & \mathbf{0} & \mathbf{0} \\ & & & & & & \ddots & & & & & & \\ & & & & & & & \ddots & & & & & \\ \mathbf{0} & \mathbf{0} & \mathbf{0} & \mathbf{0} & & \cdots & \mathbf{I}_{\mathbf{N}_{\mathbf{R}}} & \mathbf{0} & \mathbf{0} & \mathbf{0} & \mathbf{0} & \mathbf{0} & \mathbf{0} \\ \mathbf{0} & \mathbf{0} & \mathbf{0} & \mathbf{0} & & \cdots & \mathbf{0} & \mathbf{0} & \mathbf{0} & \mathbf{0} & \mathbf{I}_{N_{\mathbf{L}}} & \mathbf{0} & \mathbf{0} \\ \mathbf{0} & \mathbf{0} & \mathbf{0} & \mathbf{0} & & \cdots & \mathbf{0} & \mathbf{0} & \mathbf{I}_{\mathbf{N}_{\mathbf{R}}} & \mathbf{0} & \mathbf{0} & \mathbf{0} & \mathbf{0} \\ \mathbf{0} & \mathbf{0} & \mathbf{0} & \mathbf{0} & & \cdots & \mathbf{0} & \mathbf{0} & \mathbf{0} & \mathbf{0} & \mathbf{0} & \mathbf{0} & \mathbf{I}_{N_{\mathbf{L}}} \\ \mathbf{0} & \mathbf{0} & \mathbf{0} & \mathbf{0} & & \cdots & \mathbf{0} & \mathbf{0} & \mathbf{0} & \mathbf{0} & \mathbf{I}_{N_{\mathbf{R}}} & \mathbf{0} & \mathbf{0} \\ \mathbf{0} & \mathbf{0} & \mathbf{0} & \mathbf{0} & & \cdots & \mathbf{0} & \mathbf{0} & \mathbf{0} & \mathbf{0} & \mathbf{0} & \mathbf{0} & \mathbf{0} \end{bmatrix} \begin{bmatrix} \vec{\psi}_{R_{out_0}} \\ \mathbf{0} \\ \vec{\psi}_{R_{out_1}} \\ \vec{\psi}_{L_{out_1}} \\ \vec{\psi}_{R_{out_2}} \\ \vec{\psi}_{L_{out_2}} \\ \\ \\ \vec{\psi}_{R_{out_{I-1}}} \\ \vec{\psi}_{L_{out_{I-1}}} \\ \vec{\psi}_{R_{out_I}} \\ \vec{\psi}_{L_{out_I}} \\ \mathbf{0} \\ \vec{\psi}_{L_{out_{I+1}}} \end{bmatrix} \tag{146}$$

Two of the equations leading to the system denoted by equation (146) carry no information. These correspond to the phantom cell edge flux corresponding to the edges

that are not shared with cell 1 or cell I. Noting that the first and last rows and the second and next to last column are zero in the matrix of equation (146) we can remove these equations from the system since they carry no information. Doing this results in

$$\begin{bmatrix} \vec{\psi}_{L_{in_0}} \\ \vec{\psi}_{R_{in_1}} \\ \vec{\psi}_{L_{in_1}} \\ \vec{\psi}_{R_{in2}} \\ \vec{\psi}_{L_{in_2}} \\ \vdots \\ \\ \vec{\psi}_{R_{in_{I-1}}} \\ \vec{\psi}_{L_{in_{I-1}}} \\ \vec{\psi}_{R_{in_I}} \\ \vec{\psi}_{L_{in_I}} \\ \vec{\psi}_{R_{in_{I+1}}} \end{bmatrix} = \begin{bmatrix} \mathbf{0} & \mathbf{0} & \mathbf{I}_{N_\mathbf{L}} & \mathbf{0} & \mathbf{0} & \mathbf{0} & \mathbf{0} & \mathbf{0} & \mathbf{0} & \mathbf{0} & \mathbf{0} & \mathbf{0} \\ \mathbf{I}_{N_\mathbf{R}} & \mathbf{0} & \mathbf{0} & \mathbf{0} & \mathbf{0} & \mathbf{0} & \mathbf{0} & \mathbf{0} & \mathbf{0} & \mathbf{0} & \mathbf{0} & \mathbf{0} \\ \mathbf{0} & \mathbf{0} & \mathbf{0} & \mathbf{0} & \mathbf{I}_{N_\mathbf{L}} & \mathbf{0} & \mathbf{0} & \mathbf{0} & \mathbf{0} & \mathbf{0} & \mathbf{0} & \mathbf{0} \\ \mathbf{0} & \mathbf{I}_{N_\mathbf{R}} & \mathbf{0} & \mathbf{0} & \mathbf{0} & \mathbf{0} & \mathbf{0} & \mathbf{0} & \mathbf{0} & \mathbf{0} & \mathbf{0} & \mathbf{0} \\ \mathbf{0} & \mathbf{0} & \mathbf{0} & \mathbf{0} & \mathbf{0} & \mathbf{0} & \mathbf{I}_{\mathbf{N_L}} & \mathbf{0} & \mathbf{0} & \mathbf{0} & \mathbf{0} & \mathbf{0} \\ & & & & & \ddots & & & & & & \\ & & & & & & \ddots & & & & & \\ \mathbf{0} & \mathbf{0} & \mathbf{0} & \mathbf{0} & \mathbf{0} & \mathbf{I}_{\mathbf{N_R}} & \mathbf{0} & \mathbf{0} & \mathbf{0} & \mathbf{0} & \mathbf{0} & \mathbf{0} \\ \mathbf{0} & \mathbf{0} & \mathbf{0} & \mathbf{0} & \mathbf{0} & \mathbf{0} & \mathbf{0} & \mathbf{0} & \mathbf{0} & \mathbf{0} & \mathbf{I}_{N_\mathbf{L}} & \mathbf{0} \\ \mathbf{0} & \mathbf{0} & \mathbf{0} & \mathbf{0} & \mathbf{0} & \mathbf{0} & \mathbf{0} & \mathbf{I}_{\mathbf{N_R}} & \mathbf{0} & \mathbf{0} & \mathbf{0} & \mathbf{0} \\ \mathbf{0} & \mathbf{0} & \mathbf{0} & \mathbf{0} & \mathbf{0} & \mathbf{0} & \mathbf{0} & \mathbf{0} & \mathbf{0} & \mathbf{0} & \mathbf{0} & \mathbf{I}_{N_\mathbf{L}} \\ \mathbf{0} & \mathbf{0} & \mathbf{0} & \mathbf{0} & \mathbf{0} & \mathbf{0} & \mathbf{0} & \mathbf{0} & \mathbf{0} & \mathbf{I}_{N_\mathbf{R}} & \mathbf{0} & \mathbf{0} \end{bmatrix} \begin{bmatrix} \vec{\psi}_{R_{out_0}} \\ \vec{\psi}_{R_{out_1}} \\ \vec{\psi}_{L_{out_1}} \\ \vec{\psi}_{R_{out_2}} \\ \vec{\psi}_{L_{out_2}} \\ \vdots \\ \\ \vec{\psi}_{R_{out_{I-1}}} \\ \vec{\psi}_{L_{out_{I-1}}} \\ \vec{\psi}_{R_{out_I}} \\ \vec{\psi}_{L_{out_I}} \\ \vec{\psi}_{L_{out_{I+1}}} \end{bmatrix}. \quad (147)$$

Defining $\mathbf{P}_{IO}$ as the matrix of equation (147)

$$\mathbf{P}_{IO} = \begin{bmatrix} \mathbf{0} & \mathbf{0} & \mathbf{I}_{N_\mathbf{L}} & \mathbf{0} & \mathbf{0} & \mathbf{0} & \mathbf{0} & \cdots & \mathbf{0} & \mathbf{0} & \mathbf{0} & \mathbf{0} \\ \mathbf{I}_{N_\mathbf{R}} & \mathbf{0} & \mathbf{0} & \mathbf{0} & \mathbf{0} & \mathbf{0} & \mathbf{0} & \cdots & \mathbf{0} & \mathbf{0} & \mathbf{0} & \mathbf{0} \\ \mathbf{0} & \mathbf{0} & \mathbf{0} & \mathbf{0} & \mathbf{I}_{N_\mathbf{L}} & \mathbf{0} & \mathbf{0} & \cdots & \mathbf{0} & \mathbf{0} & \mathbf{0} & \mathbf{0} \\ \mathbf{0} & \mathbf{I}_{N_\mathbf{R}} & \mathbf{0} & \mathbf{0} & \mathbf{0} & \mathbf{0} & \mathbf{0} & \cdots & \mathbf{0} & \mathbf{0} & \mathbf{0} & \mathbf{0} \\ \mathbf{0} & \mathbf{0} & \mathbf{0} & \mathbf{0} & \mathbf{0} & \mathbf{0} & \mathbf{I}_{\mathbf{N_L}} & \cdots & \mathbf{0} & \mathbf{0} & \mathbf{0} & \mathbf{0} \\ & & & & & \ddots & & & & & & \\ & & & & & & \ddots & & & & & \\ \mathbf{0} & \mathbf{0} & \mathbf{0} & \mathbf{0} & \cdots & \mathbf{I}_{\mathbf{N_R}} & \mathbf{0} & \mathbf{0} & \mathbf{0} & \mathbf{0} & \mathbf{0} & \mathbf{0} \\ \mathbf{0} & \mathbf{0} & \mathbf{0} & \mathbf{0} & \cdots & \mathbf{0} & \mathbf{0} & \mathbf{0} & \mathbf{0} & \mathbf{0} & \mathbf{I}_{N_\mathbf{L}} & \mathbf{0} \\ \mathbf{0} & \mathbf{0} & \mathbf{0} & \mathbf{0} & \cdots & \mathbf{0} & \mathbf{0} & \mathbf{I}_{\mathbf{N_R}} & \mathbf{0} & \mathbf{0} & \mathbf{0} & \mathbf{0} \\ \mathbf{0} & \mathbf{0} & \mathbf{0} & \mathbf{0} & \cdots & \mathbf{0} & \mathbf{0} & \mathbf{0} & \mathbf{0} & \mathbf{0} & \mathbf{0} & \mathbf{I}_{N_\mathbf{L}} \\ \mathbf{0} & \mathbf{0} & \mathbf{0} & \mathbf{0} & \cdots & \mathbf{0} & \mathbf{0} & \mathbf{0} & \mathbf{0} & \mathbf{I}_{N_\mathbf{R}} & \mathbf{0} & \mathbf{0} \end{bmatrix}, \tag{148}$$

equation (147) can be written more compactly as

$$\overline{\Psi}_{in} = \mathbf{P}_{IO}\ \overline{\Psi}_{out}. \tag{149}$$

Note that $\mathbf{P}_{IO}$ is a permutation matrix that reorders $\overline{\Psi}_{out}$ to become $\overline{\Psi}_{in}$. As such, its inverse is its transpose.

Global spatially coupled coefficient matrices, denoted as $\mathbf{M}_{OE}$ and $\mathbf{M}_{OI}$, are assembled from the cell coefficient matrices of equations (114) and (115). These matrices are ordered so that their first and last rows correspond with phantom cells and their other rows correspond with interior cells

$$\mathbf{M}_{OI} = \begin{bmatrix} \boldsymbol{\alpha}_\ell & & & & & & & & \\ & \mathbf{m}_{oi_{N_R,N_R,1}} & \mathbf{m}_{oi_{N_R,N_L,1}} & & & & & & \\ & \mathbf{m}_{oi_{N_L,N_R,1}} & \mathbf{m}_{oi_{N_L,N_L,1}} & & & & & & \\ & & & \mathbf{m}_{oi_{N_R,N_R,2}} & \mathbf{m}_{oi_{N_R,N_L,2}} & & & & \\ & & & \mathbf{m}_{oi_{N_L,N_R,2}} & \mathbf{m}_{oi_{N_L,N_L,2}} & & & & \\ & & & & & \ddots & & & \\ & & & & & & \mathbf{m}_{oi_{N_R,N_R,I}} & \mathbf{m}_{oi_{N_R,N_L,I}} & \\ & & & & & & \mathbf{m}_{oi_{N_L,N_R,I}} & \mathbf{m}_{oi_{N_L,N_L,I}} & \\ & & & & & & & & \boldsymbol{\alpha}_r \end{bmatrix}, \tag{150}$$

$$\mathbf{M}_{OE} = \begin{bmatrix} \mathbf{0} & & & & & & & & \\ & \mathbf{m}_{o\mathsf{E}_{N_R,N_R,1}} & \mathbf{m}_{o\mathsf{E}_{N_R,N_L,1}} & & & & & & \\ & \mathbf{m}_{o\mathsf{E}_{N_L,N_R,1}} & \mathbf{m}_{o\mathsf{E}_{N_L,N_L,1}} & & & & & & \\ & & & \mathbf{m}_{o\mathsf{E}_{N_R,N_R,2}} & \mathbf{m}_{o\mathsf{E}_{N_R,N_L,2}} & & & & \\ & & & \mathbf{m}_{o\mathsf{E}_{N_L,N_R,2}} & \mathbf{m}_{o\mathsf{E}_{N_L,N_L,2}} & & & & \\ & & & & & \ddots & & & \\ & & & & & & \mathbf{m}_{o\mathsf{E}_{N_R,N_R,I}} & \mathbf{m}_{o\mathsf{E}_{N_R,N_L,I}} & \\ & & & & & & \mathbf{m}_{o\mathsf{E}_{N_L,N_R,I}} & \mathbf{m}_{o\mathsf{E}_{N_L,N_L,I}} & \\ & & & & & & & & \mathbf{0} \end{bmatrix}. \tag{151}$$

Using equations (114), (135), (150), and (151), the spatially coupled system becomes:

$$\overline{\Psi}_{out} = \mathbf{M_{OI}}\ \overline{\Psi}_{in} + \mathbf{M_{OE}}\ \overline{E}_A\ . \tag{152}$$

Equation (152) represents the transport equations explicitly. It accounts for all particle penetration and scattering. Using equation (149) and combining $\overline{\Psi}_{out}$ coefficients results in

$$\left(\mathbf{I} - \mathbf{M_{OI}} \;\; \mathbf{P}_{IO}\right)\overline{\Psi}_{out} \;\; = \mathbf{M_{OE}} \;\; \vec{E}_A \;\; . \tag{153}$$

The matrix $\left(\mathbf{I} - \mathbf{M_{OI}} \;\; \mathbf{P}\right)$ is reordered to result in a banded diagonal matrix of minimum bandwidth. The reordering matrix which achieves this minimum bandwidth structure is

$$\mathbf{P}_B = \begin{bmatrix}
\mathbf{I}_{N_\mathbf{R}} & \mathbf{0} & \mathbf{0} & \mathbf{0} & \mathbf{0} & \mathbf{0} & \mathbf{0} & \mathbf{0} & \mathbf{0} & \mathbf{0} & \mathbf{0} & \mathbf{0} \\
\mathbf{0} & \mathbf{0} & \mathbf{I}_{N_\mathbf{L}} & \mathbf{0} & \mathbf{0} & \mathbf{0} & \mathbf{0} & \mathbf{0} & \mathbf{0} & \mathbf{0} & \mathbf{0} & \mathbf{0} \\
\mathbf{0} & \mathbf{I}_{N_\mathbf{R}} & \mathbf{0} & \mathbf{0} & \mathbf{0} & \mathbf{0} & \mathbf{0} & \mathbf{0} & \mathbf{0} & \mathbf{0} & \mathbf{0} & \mathbf{0} \\
\mathbf{0} & \mathbf{0} & \mathbf{0} & \mathbf{0} & \mathbf{I}_{N_\mathbf{L}} & \mathbf{0} & \mathbf{0} & \mathbf{0} & \mathbf{0} & \mathbf{0} & \mathbf{0} & \mathbf{0} \\
\mathbf{0} & \mathbf{0} & \mathbf{0} & \mathbf{I}_{\mathbf{N_R}} & \mathbf{0} & \mathbf{0} & \mathbf{0} & \mathbf{0} & \mathbf{0} & \mathbf{0} & \mathbf{0} & \mathbf{0} \\
 & & & & & \ddots & & & & & & \\
 & & & & & & \ddots & & & & & \\
\mathbf{0} & \mathbf{0} & \mathbf{0} & \mathbf{0} & \mathbf{0} & \mathbf{0} & \mathbf{0} & \mathbf{I}_{\mathbf{N_L}} & \mathbf{0} & \mathbf{0} & \mathbf{0} & \mathbf{0} \\
\mathbf{0} & \mathbf{0} & \mathbf{0} & \mathbf{0} & \mathbf{0} & \mathbf{0} & \mathbf{I}_{\mathbf{N_R}} & \mathbf{0} & \mathbf{0} & \mathbf{0} & \mathbf{0} & \mathbf{0} \\
\mathbf{0} & \mathbf{0} & \mathbf{0} & \mathbf{0} & \mathbf{0} & \mathbf{0} & \mathbf{0} & \mathbf{0} & \mathbf{0} & \mathbf{0} & \mathbf{I}_{N_\mathbf{L}} & \mathbf{0} \\
\mathbf{0} & \mathbf{0} & \mathbf{0} & \mathbf{0} & \mathbf{0} & \mathbf{0} & \mathbf{0} & \mathbf{0} & \mathbf{0} & \mathbf{I}_{N_\mathbf{R}} & \mathbf{0} & \mathbf{0} \\
\mathbf{0} & \mathbf{0} & \mathbf{0} & \mathbf{0} & \mathbf{0} & \mathbf{0} & \mathbf{0} & \mathbf{0} & \mathbf{0} & \mathbf{0} & \mathbf{0} & \mathbf{I}_{N_\mathbf{L}}
\end{bmatrix} . \tag{154}$$

Applying $\mathbf{P}_B$ to equation (153) and solving for $\overline{\Psi}_{out}$ yields the explicit solution of the fully coupled, in both angle and space, system of transport equations

$$\overline{\Psi}_{out} = \left(\mathbf{P}_B \left(\mathbf{I} - \mathbf{M}_{OI} \;\; \mathbf{P}_{IO}\right)\right)^{-1} \mathbf{P}_B \, \mathbf{M}_{OE} \;\; \vec{E}_A \;\; . \tag{155}$$

Edge flux computed from equation (155) yields an explicit solution for the discrete ordinates equations without iteration. It accounts for particle transport within a cell and particle transport across cells. Unfortunately, the $2\,N\,I$ system which results from N directions and I cells is impractical to invert or solve, particularly if the spatial

and angular discretization are fine. This is why source iteration (SI) does not attempt to solve this system. Instead SI approximates the solution by iteration on the scattering source.

Angular and Spatial Distribution Iteration

I did not attempt to solve the system of equations represented by equation (155)in this research. Rather, I investigated an efficient iteration scheme that was different from source iteration. I solved equation (113) with a refined angular quadrature locally within each individual spatial cell using an estimate for incoming edge flux and its cell transport coefficients. I then estimated particle transport among cells across the problem space using equation (155) with a coarse angular quadrature and transport coefficients that are correct for the approximate edge flux used. I developed and examined a method that couples local within cell scattering using a refined angular quadrature with across cell particle transport using transport coefficients obtained from a coarse angular quadrature in a unique way that retains angular resolution. The concept is similar to 2 direction synthetic acceleration but differs from it in two important ways:

1. The proposed method does not use transport sweeps. The proposed method does not approximate the error in the flux iterate to correct a transport sweep.

2. The method estimates the solution directly with a coarse angular quadrature and a fine angular quadrature linked with transport coefficients.

The method uses the coarse angular quadrature to directly solve equation (155). This provides edge fluxes ($\overline{\Psi}_{in}$) that are approximate. These edge flux values are used in equation (113) to gain a better estimate of transport coefficients ($K_{OS_{n,i}}, K_{AS_{n,i}}, K_{OI_{n,i}}$, $K_{AI_{n,i}}, K_{OE_{n,i}}, K_{AE_{n,i}}$), in a way not yet discussed, in order to obtain a better estimate of $\overline{\Psi}_{in}$ for a two direction spatially coupled angular quadrature. In my method $4I$ equations are solved in the spatially coupled coarse angle routine or $4N$ equations are solved in the fine angle within cell routine as compared with the $2NI$ equations of the fully coupled system,. By de-coupling space and direction the system of equations is reduced to either four times the number of ordinates in the angular quadrature or four times the spatial cells. This is far less than the number of ordinates times the number of spatial cells required for the fully coupled system.

Unique aspects of this research are the use of the flux distribution along cell edges to yield progressively better edge flux transport coefficients and of iteration on angular and spatial flux distributions. The method effectively amounts to improvement of transport coefficients and iteration on angle and spatial flux distributions. The method eliminates the need for modeling neutron flights by transport sweeps as is done with SI. The method significantly reduces transport iterations, even when scattering ratios are nearly 1. The method produces reliably accurate answers even when neutron flights are nearly infinite. Discussion of the fine angle and coarse angle solution methods and their coupling follows.

Explicit Solution of a Two Direction Transport Problem Coupled in Space

Although it was not practical to solve the discrete ordinates system of equations with many directions coupled across space, it is practical if there are only two directions to couple across space. Consider a slab geometry transport problem with two

directions. Following the vector notation of the previous section the cell transport equation is given by

$$\mathbf{P}_{B_m}\left(\mathbf{I}-\mathbf{M_{OI}}\,\mathbf{P}\right)\overline{\Psi}_{out} \;=\mathbf{M_{OE}}.\overline{E}_A\;, \tag{156}$$

where $\mathbf{M_{OI}}$ is

$$\mathbf{M_{OI}}=\begin{bmatrix}
\alpha_{L_{2,1}} & & & & & & & & & \\
 & m_{OI_{1,1,1}} & m_{OI_{1,2,1}} & & & & & & & \\
 & m_{OI_{2,1,1}} & m_{OI_{2,2,1}} & & & & & & & \\
 & & & m_{OI_{1,1,2}} & m_{OI_{1,2,2}} & & & & & \\
 & & & m_{OI_{2,1,2}} & m_{OI_{2,2,2}} & & & & & \\
 & & & & & \ddots & & & & \\
 & & & & & & m_{OI_{1,1,I}} & m_{OI_{1,2,I}} & & \\
 & & & & & & m_{OI_{2,1,I}} & m_{OI_{2,2,I}} & & \\
 & & & & & & & & \alpha_{L_{1,2}} &
\end{bmatrix}, \tag{157}$$

and $\mathbf{M_{OE}}$ is

$$\mathbf{M_{OE}}=\begin{bmatrix}
0 & & & & & & & & & \\
 & m_{OE_{1,1,1}} & m_{OE_{1,2,1}} & & & & & & & \\
 & m_{OE_{2,1,1}} & m_{OE_{2,2,1}} & & & & & & & \\
 & & & m_{OE_{1,1,2}} & m_{OE_{1,2,2}} & & & & & \\
 & & & m_{OE_{2,1,2}} & m_{OE_{2,2,2}} & & & & & \\
 & & & & & \ddots & & & & \\
 & & & & & & m_{OE_{1,1,I}} & m_{OE_{1,2,I}} & & \\
 & & & & & & m_{OE_{2,1,I}} & m_{OE_{2,2,I}} & & \\
 & & & & & & & & 0 &
\end{bmatrix}. \tag{158}$$

$\mathbf{P}$ is given by equation (148) and $\mathbf{P}_{\mathbf{B}_m}$ by equation (154) with

$$\mathbf{I}_{N_R} = \begin{bmatrix} 1 & 0 \\ 0 & 0 \end{bmatrix}, \tag{159}$$

$$\mathbf{I}_{N_L} = \begin{bmatrix} 0 & 0 \\ 0 & 1 \end{bmatrix}. \tag{160}$$

The components of the spatially coupled coefficient matrix ($\mathbf{M}_{OI}$) are given by equations (114) and (115). The diagonal coefficient matrices used in these equations are

$$\mathbf{K}_{OI_i} = \begin{bmatrix} K_{OI_{1,i}} & 0 \\ 0 & K_{OI_{2,i}} \end{bmatrix}, \tag{161}$$

$$\mathbf{K}_{OS_i} = \begin{bmatrix} K_{OS_{1,i}} & 0 \\ 0 & K_{OS_{2,i}} \end{bmatrix}, \tag{162}$$

$$\mathbf{K}_{AI_i} = \begin{bmatrix} K_{AI_{1,i}} & 0 \\ 0 & K_{AI_{2,i}} \end{bmatrix}, \tag{163}$$

$$\mathbf{K}_{AS_i} = \begin{bmatrix} K_{AS_{1,i}} & 0 \\ 0 & K_{AS_{2,i}} \end{bmatrix}. \tag{164}$$

The scattering cross section matrix is a dense matrix

$$\mathbf{\Sigma}_{S_i} = \begin{bmatrix} \sigma_{s_{1,1,i}} & \sigma_{s_{2,1,i}} \\ \sigma_{s_{2,1,i}} & \sigma_{s_{2,2,i}} \end{bmatrix}. \tag{165}$$

If there are I cells in a spatial partition the arrays of incoming fluxes, outgoing fluxes and intrinsic emissions are

$$\overline{\Psi}_{out} = \begin{bmatrix} \psi_{out_{1,\frac{1}{2}}} \\ \psi_{out_{1,\frac{3}{2}}} \\ \psi_{out_{2,\frac{1}{2}}} \\ \psi_{out_{1,\frac{5}{2}}} \\ \psi_{out_{2,\frac{3}{2}}} \\ \vdots \\ \vdots \\ \psi_{out_{1,\mathtt{I}-\frac{1}{2}}} \\ \psi_{out_{2,\mathtt{I}-\frac{3}{2}}} \\ \psi_{out_{1,\mathtt{I}+\frac{1}{2}}} \\ \psi_{out_{2,\mathtt{I}-\frac{1}{2}}} \\ \psi_{out_{2,\mathtt{I}+\frac{1}{2}}} \end{bmatrix}, \quad \overline{\Psi}_{in} = \begin{bmatrix} \psi_{in_{2,\frac{1}{2}}} \\ \psi_{in_{1,\frac{1}{2}}} \\ \psi_{in_{2,\frac{3}{2}}} \\ \psi_{in_{1,\frac{3}{2}}} \\ \psi_{in_{2,\frac{5}{2}}} \\ \vdots \\ \vdots \\ \psi_{in_{1,\mathtt{I}-\frac{3}{2}}} \\ \psi_{in_{2,\mathtt{I}-\frac{1}{2}}} \\ \psi_{in_{1,\mathtt{I}-\frac{1}{2}}} \\ \psi_{in_{2,\mathtt{I}+\frac{1}{2}}} \\ \psi_{in_{1,\mathtt{I}+\frac{1}{2}}} \end{bmatrix}, \quad \overline{E}_A = \begin{bmatrix} 0 \\ E_{A_{1,1}} \\ E_{A_{2,1}} \\ E_{A_{1,2}} \\ E_{A_{2,2}} \\ \vdots \\ \vdots \\ E_{A_{2,\mathtt{I}-1}} \\ E_{A_{2,\mathtt{I}-1}} \\ E_{A_{1,\mathtt{I}}} \\ E_{A_{2,\mathtt{I}}} \\ 0 \end{bmatrix}. \tag{166}$$

Substituting equations (157), (158), and (166) into equation (156) results in

$$\begin{bmatrix} 1 & 0 & -\alpha_L & 0 & \cdots & & \\ -m_{oi_{1,1,1}} & 1 & 0 & -m_{oi_{1,2,1}} & 0 & \cdots & \\ -m_{oi_{2,1,1}} & 0 & 1 & -m_{oi_{2,2,1}} & 0 & \cdots & \\ & & & \ddots & & & \\ & \cdots & 0 & -m_{oi_{1,1,I}} & 1 & 0 & -m_{oi_{1,1,I}} \\ & \cdots & 0 & -m_{oi_{2,1,1}} & 0 & 1 & -m_{oi_{2,2,I}} \\ & & \cdots & 0 & -\alpha_R & 0 & 1 \end{bmatrix} \begin{bmatrix} \psi_{1,\frac{1}{2}} \\ \psi_{1,\frac{3}{2}} \\ \psi_{2,\frac{1}{2}} \\ \vdots \\ \psi_{1,\mathtt{I}+\frac{1}{2}} \\ \psi_{2,\mathtt{I}-\frac{1}{2}} \\ \psi_{2,\mathtt{I}+\frac{1}{2}} \end{bmatrix} =$$

$$\begin{bmatrix} 0 & & \cdots & & & 0 \\ m_{o\mathsf{E}_{2,1,1}} & m_{o\mathsf{E}_{2,2,1}} & 0 & \cdots & & \\ m_{o\mathsf{E}_{1,1,1}} & m_{o\mathsf{E}_{1,2,1}} & 0 & \cdots & & \\ & & & \ddots & & \\ & \cdots & & 0 & m_{o\mathsf{E}_{2,1,I}} & m_{o\mathsf{E}_{2,1,I}} \\ & \cdots & & 0 & m_{o\mathsf{E}_{1,1,1}} & m_{o\mathsf{E}_{1,2,I}} \\ 0 & & & \cdots & & 0 \end{bmatrix} \begin{bmatrix} 0 \\ E_{A_{1,1}} \\ E_{A_{2,1}} \\ \vdots \\ E_{A_{1,I}} \\ E_{A_{2,I}} \\ 0 \end{bmatrix}. \qquad (167)$$

The transport coefficient entries of the left hand side matrix of equation (167) ($m_{OI_{1,1,i}}, m_{OI_{1,2,i}}, m_{OI_{1,2,i}}, m_{OI_{2,2,i}}$) describe the fraction of entering flux in a direction (left or right) that leaves the cell, having scattered any number of times within the cell. A particle enters a cell from one of two possible directions. Having entered a cell in an ordinate, a particle then either transmits to the other side in that ordinate or is reflected backward into the opposite ordinate. Because of this it is useful to think of the transport coefficient entries as reflection or transmission coefficients. The transmission coefficient describes the fraction of particles that enter a cell, scatter any number of times, then exit that cell in the original direction of its flow while a reflection coefficient describes the fraction of particles that enter a cell scatter any number of

times then exit that cell in the opposite direction to its original flow. Defining reflection coefficients as:

$$t_{1,i} = m_{OI\,1,1_i} \ , \tag{168}$$

$$t_{2,i} = m_{OI\,2,2_i} \ , \tag{169}$$

and transmission coefficients as

$$r_{1,\mathrm{i}} = m_{OI\,1,2_i} \ , \tag{170}$$

$$r_{2,\mathrm{i}} = m_{OI\,2,1_i} \ , \tag{171}$$

equation (167) is written

$$\begin{bmatrix} 1 & -\alpha_L & 0 & 0 & \cdots & & 0 \\ -r_{1,1} & 1 & 0 & -t_{1,1} & 0 & \cdots & 0 \\ -t_{2,1} & 0 & 1 & -r_{2,1} & 0 & \cdots & 0 \\ 0 & & & \ddots & & & 0 \\ 0 & \cdots & 0 & -r_{1,I} & 1 & 0 & -t_{1,I} \\ 0 & \cdots & 0 & -t_{2,I} & 0 & 1 & -r_{1,I} \\ 0 & & \cdots & 0 & 0 & -\alpha_R & 1 \end{bmatrix} \begin{bmatrix} \psi_{1,\frac{1}{2}} \\ \psi_{1,\frac{3}{2}} \\ \psi_{2,\frac{1}{2}} \\ \vdots \\ \psi_{1,I+\frac{1}{2}} \\ \psi_{2,I-\frac{1}{2}} \\ \psi_{2,I+\frac{1}{2}} \end{bmatrix} =$$

$$\begin{bmatrix} 0 & 0 & \cdots & & & & 0 \\ m_{oE_{2,1,1}} & m_{oE_{2,2,1}} & 0 & \cdots & & & 0 \\ m_{oE_{1,1,1}} & m_{oE_{1,2,1}} & 0 & \cdots & & & 0 \\ 0 & & & \ddots & & & 0 \\ 0 & \cdots & & & 0 & m_{oE_{2,1,I}} & m_{oE_{2,1,I}} \\ 0 & \cdots & & & 0 & m_{oE_{1,1,1}} & m_{oE_{1,2,I}} \\ 0 & & & \cdots & 0 & 0 & \end{bmatrix} \begin{bmatrix} 0 \\ E_{A_{1,1}} \\ E_{A_{2,1}} \\ \vdots \\ E_{A_{1,I}} \\ E_{A_{2,I}} \\ 0 \end{bmatrix}. \qquad (172)$$

If the spatial quadrature conserves particles and $c \le 1$, then $0 \le r_{m,i} \le 1$, $0 \le t_{m,i} \le 1$, and $r_{m,i} + t_{m,i} \le 1$. If $c = 1$ then $r_{m,i} + t_{m,i} = 1$. If the boundary conditions of the system are vacuum, grey or albedo, then the system is diagonally dominant when $c \le 1$ and weakly diagonally dominant if $c = 1$. Because of this, any 1D transport problem with a unique non-trivial steady state solution results in at least a weakly diagonally dominant system with positive values on the diagonal and negative values off the diagonal. Therefore the 1D slab geometry system with two ordinates is readily solved. If an angular quadrature with two ordinates adequately described the angular flux distribution of a problem we would be able to calculate by inverting the matrix of equation (172) and solve the problem directly.

Unfortunately, a two ordinate angular approximation is most often inadequate. For example, particles that enter a mesh cell parallel to the $+x$-axis are more likely to exit a mesh cell in the $+x$ direction then particles that enter a mesh cell nearly perpendicular to the $+x$ axis. The S_2 angular quadrature does a poor job of modeling

directional dependence for this type of particle transport. Because of this, an S_2 angular quadrature is often an inadequate approximation for angular flux. I sought to overcome the weakness of this coarse approximation in angular distribution yet take advantage of its ability to fully couple cells in space without numerous particle flights. I speculated that because the coarse angular quadrature estimated flux correctly in magnitude these flux values could be used as reasonable estimates for cell entering flux. This required development of a projection scheme between coarse and fine angular quadratures. I also speculated that the approximate edge flux values obtained from the spatially coupled coarse solution could be angularly coupled to the flux locally within a spatial cell in order to approximate angular flux distribution on cell edges. Further, I speculated that the approximate angular flux distribution obtained this way could be used to improve the two ordinate transport coefficients. I expected the improved two ordinate coefficients to in turn improve the approximation for cell incoming flux. I sought to use the computational efficiency of the coarse angle spatially coupled system and the fine angle local space systems with an iteration scheme that effectively coupled the two schemes through transport coefficients.

Solution of an N direction Transport Problem with Approximate Edge Flux.

Explicit solution of equations (113) through (115) is possible, even for very fine angular quadratures, if entering flux ($\bar{\psi}_{in_i}$) is known. Equation (113) may be used to solve for exiting flux for any resolution angular quadrature without creating a system that is impractical to solve since it is done for only a single cell. The inverse matrix of equations (114) and (115), $(I - \mathbf{K}_{AS_i}\, \mathbf{\Sigma}_{S_i})^{-1}$, models scattering within a cell effectively

because it effectively accounts for an infinite number of neutron flights. This can be seen by expanding the matrix in a geometric series:

$$(I - \mathbf{K}_{AS_i}\ \boldsymbol{\Sigma}_{S_i})^{-1} = I + \mathbf{K}_{AS_i}\ \boldsymbol{\Sigma}_{S_i} + \left(\mathbf{K}_{AS_i}\ \boldsymbol{\Sigma}_{S_i}\right)^2 + \cdots + \left(\mathbf{K}_{AS_i}\ \boldsymbol{\Sigma}_{S_i}\right)^k + \ldots. \qquad \left\|\mathbf{K}_{AS_i}\ \boldsymbol{\Sigma}_{S_i}\right\|_2 < 1 \tag{173}$$

The term $\left(\mathbf{K}_{AS_i}\ \boldsymbol{\Sigma}_{S_i}\right)^k$ in this geometric series produces the flux of neutrons that have scattered k times within the cell (without leaving the cell). The first term ,I, accounts for the flux of neutrons that have not scattered since entering the cell. Thus, the series accounts for all numbers of scattering events within the cell for each particle entering the cell or emitted within the cell. If the incoming flux is correct the outgoing flux can be explicitly calculated. In application $\vec{\psi}_{in}$ is not a known quantity. It is an estimate. This estimate can be improved by using equation (113). Given estimated incoming fine angle flux, equation (113) is used to calculate fine angle outgoing flux. This is done for each spatial cell. After each cell outgoing flux is calculated boundary conditions are applied. Outgoing fluxes calculated in this way are incoming fluxes for adjacent cells with fine angle resolution. This leads to an improved incoming flux estimate. I examined whether edge flux produced with a two-ordinate angular quadrature from equation (172) could be used as input for a fine angle flux solution produced by equation (113) which in turn could produce adjusted transport coefficients. I then examined whether the adjusted transport coefficients then improved the approximate flux of the coarse angle estimate. This provided an iteration scheme. I further examined the convergence properties of this scheme. The combination of the fine angle, and coarse angle methods is discussed next.

Combining High Angular Resolution Within-Cell Transport with Low Angular Resolution Spatially-Coupled transport

The previous sections described a method for obtaining exact within cell solutions for edge flux. Continuing the notation developed in these sections, $\vec{\psi}_{in_i}$ is given by equation (93), $\vec{\psi}_{out_i}$ is given by equation (94), E_{A_i} is given by equation (101). The scattering cross section matrix is given by equation (105). The coefficient matrices $\mathbf{K}_{OI_i}, \mathbf{K}_{AI_i}, \mathbf{K}_{OS_i}, \mathbf{K}_{AS_i}, \mathbf{K}_{AE_i}, \mathbf{K}_{OE_i}$, are diagonal matrices of the form given by equation (104). The array of cell average flux is written

$$\vec{\psi}_{A_i} = \begin{bmatrix} \psi_{1,i} \\ \vdots \\ \psi_{N_R,i} \\ \psi_{N_R+1,i} \\ \vdots \\ \psi_{N,i} \end{bmatrix}. \tag{174}$$

With this notation the transport system is

$$\vec{\psi}_{out_i} = \mathbf{K}_{OI_i} \vec{\psi}_{in_i} + \mathbf{K}_{OS_i} \boldsymbol{\Sigma}_{S_i} \vec{\psi}_{A_i} + \mathbf{K}_{OE_i} \vec{E}_{A_i}, \tag{175}$$

$$\vec{\psi}_{A_i} = \mathbf{K}_{AI_i} \vec{\psi}_{in_i} + \mathbf{K}_{AS_i} \boldsymbol{\Sigma}_{S_i} \vec{\psi}_{A_i} + \mathbf{K}_{AE_i} \vec{E}_{A_i}. \tag{176}$$

The flux of particles is transported through the cells of a spatial mesh as though the particles were moving in representative directions. In discrete ordinates each component of the flux vector describes the flow of particles, through a surface patch of solid angle on the unit sphere. Figure 2 shows the flux exiting a cell edge in the left ($\mu < 0$) and right ($\mu > 0$) hemispheres for both coarse and fine angular refinements. A

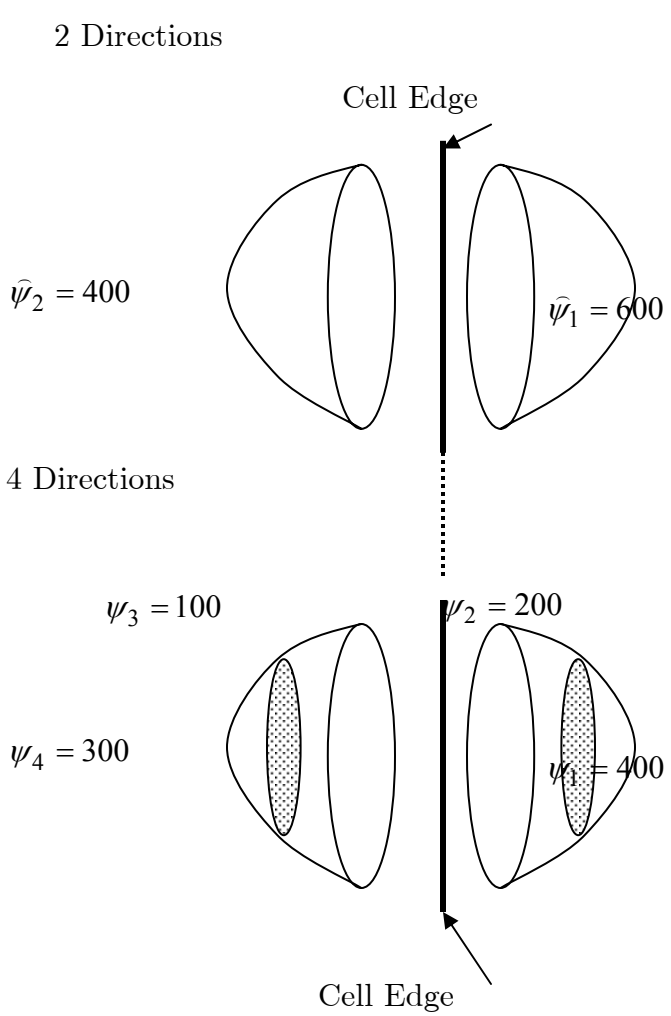

coarse angular quadrature of two directions is depicted in the top set of hemispheres and a finer angular quadrature of four directions is depicted in the bottom set of

Figure 2: Angular Flux Exiting a Cell Edge through 2 Ordinates and 4 Ordinates

hemispheres. The notation $\widehat{\psi}$ denotes a flux associated with a coarse angular quadrature. The symbol ψ denotes a flux from a finer quadrature. Elements one and four are the caps of the hemispheres and elements two and three are the bands closes to the cell edge denoting that these fluxes are in fact inclined at a steeper angle to the x axis which passes through the tip of the polar cap.

The subscript m denotes an ordinate in a two direction angular quadrature whose surface elements are the two hemispheres in Figure 2. The total flux exiting a

hemisphere, $\widehat{\psi}_{m,i+\frac{1}{2}}$, is calculated by summing all the finer angular quadrature fluxes exiting the same hemisphere.

$$\widehat{\psi}_{1,i\pm\frac{1}{2}}=\sum_{n=1}^{N_R}\psi_{n,i\pm\frac{1}{2}} \qquad i=\{1,2,\cdots \mathrm{I}\}, \tag{177}$$

$$\widehat{\psi}_{2,i\pm\frac{1}{2}}=\sum_{n=N_R+1}^{N_L}\psi_{n,i\pm\frac{1}{2}} \qquad i=\{1,\cdots,\mathrm{I}\}. \tag{178}$$

In a similar way the average flux in a spatial cell in a hemisphere denoted as, $\widehat{\psi}_{m,i}$, is

$$\widehat{\psi}_{1,i}=\sum_{n=1}^{N_R}\psi_{n,i} \qquad i=\{1,\cdots,\mathrm{I}\}, \tag{179}$$

and

$$\widehat{\psi}_{2,i}=\sum_{n=N_R+1}^{N}\psi_{n,i} \qquad i=\{1,\cdots,\mathrm{I}\}. \tag{180}$$

Further the average particles scattered per volume in the solid angle whose average particle direction is in one of the hemispheres of Figure 2 is denoted $\widehat{S}_{A_{m,i}}$. It is calculated by summing the particles per solid angle exiting the associated hemisphere

$$\widehat{S}_{A_{1,i}}=\sum_{n=1}^{N_R}\sum_{n'=1}^{N}\sigma_{s_{n',n,i}}\psi_{n',i} \qquad i=\{1,\cdots,\mathrm{I}\}, \tag{181}$$

and

$$\widehat{S}_{A_{2,i}}=\sum_{n=N_R+1}^{N}\sum_{n'=1}^{N}\sigma_{s_{n',n,i}}\psi_{n',i} \qquad i=\{1,\cdots,\mathrm{I}\}. \tag{182}$$

The average particles per volume emitted in the solid angle whose average particle direction is in one of the hemispheres of Figure 2 is denoted $\widehat{E}_{A_{m,i}}$. It is calculated by summing the particles per solid angle exiting the associated hemisphere

$$\widehat{E}_{A_{1,i}} = \sum_{n=1}^{N_R} E_{An,i} \qquad i = \{1, \cdots, \mathrm{I}\}, \tag{183}$$

$$\widehat{E}_{A_{2,i}} = \sum_{n=N_R}^{N_L} E_{An,i} \qquad i = \{1, \cdots, \mathrm{I}\}. \tag{184}$$

As in the previous sections N_R denotes the number of rightward flux ordinates and N_L the number leftward

$$N = N_R + N_L . \tag{185}.$$

Defining $\overline{\overline{\psi}}_{in_i}, \overline{\overline{\psi}}_{out_i}, \overline{\overline{\psi}}_{A_i}$ as the coarse angular quadrature inbound, outbound, and cell average angular flux arrays in cell i, they are written as

$$\overline{\overline{\psi}}_{in_i} = \begin{bmatrix} \widehat{\psi}_{1,i-\frac{1}{2}} \\ \widehat{\psi}_{2,i+\frac{1}{2}} \end{bmatrix}, \tag{186}$$

$$\overline{\overline{\psi}}_{out_i} = \begin{bmatrix} \widehat{\psi}_{1,i+\frac{1}{2}} \\ \widehat{\psi}_{2,i-\frac{1}{2}} \end{bmatrix}, \tag{187}$$

$$\overline{\overline{\psi}}_{A_i} = \begin{bmatrix} \widehat{\psi}_{1,i} \\ \widehat{\psi}_{2,i} \end{bmatrix}, \tag{188}$$

$$\overline{\overline{E}}_{A_i} = \begin{bmatrix} \widehat{E}_{A_{1,i}} \\ \widehat{E}_{A_{2,i}} \end{bmatrix}. \tag{189}$$

Defining the array

$$\mathbf{I}_{2,N} = \begin{bmatrix} 1 & \cdots & 1 & 0 & \cdots & 0 \\ 0 & \cdots & 0 & 1 & \cdots & 1 \end{bmatrix}, \tag{190}$$

where the rows of $\mathbf{I}_{2,N}$ have N elements consisting of N_R or N_L ones or zeros. This matrix facilitates writing coarse quantities as the sum of fine quantities. These coarse fluxes in compact form are

$$\overline{\overline{\psi}}_{in_i} = \mathbf{I}_{2,N}\, \overline{\psi}_{in_i}\,, \tag{191}$$

$$\overline{\overline{\psi}}_{out_i} = \mathbf{I}_{2,N}\, \overline{\psi}_{out_i}\,, \tag{192}$$

$$\overline{\overline{\psi}}_{A_i} = \mathbf{I}_{2,N}\, \overline{\psi}_{A_i}\,, \tag{193}$$

$$\overline{\overline{E}}_{A_i} = \mathbf{I}_{2,N}\, \overline{E}_{A_i}\,. \tag{194}$$

The transport equations for these two directions are given by equations (109) and (110). Operating on these equations with $I_{2,N}$ results in:

$$\overline{\overline{\psi}}_{out_i} = \mathbf{I}_{2,N}\, \mathbf{K}_{OI_i}\, \overline{\psi}_{in_i} + \mathbf{I}_{2,N}\, \mathbf{K}_{OS_i}\, \boldsymbol{\Sigma}_{S_i}\, \overline{\psi}_{A_i} + \mathbf{I}_{2,N}\, \mathbf{K}_{OE_i}\, \overline{E}_{A_i}\,, \tag{195}$$

$$\overline{\overline{\psi}}_{A_i} = \mathbf{I}_{2,N} \left(\mathbf{K}_{AI_i}\, \overline{\psi}_{in_i} \right) + \mathbf{I}_{2,N} \left(\mathbf{K}_{AS_i}\, \boldsymbol{\Sigma}_{S_i}\, \overline{\psi}_{A_i} \right) + \mathbf{I}_{2,N} \left(\mathbf{K}_{AE_i}\, \overline{E}_{A_i} \right). \tag{196}$$

Equations (195) and (196) result in vectors of length 2 that are obtained from the matrix multiplication of the 2xN matrix of equation (190) with the vectors of length N from equations (109) and (110). The first term of the two component array resulting from equation (195) is

$$\widehat{\psi}_{1,i+\frac{1}{2}} = \sum_{n=1}^{N_R}\left(K_{OI_{n,i}} \ \psi_{n,i-\frac{1}{2}} \right) + \sum_{n=1}^{N_R}\left(K_{OS_{n,i}} \sum_{n'=1}^{N} \sigma_{s_{n',n,i}} \psi_{n',i} \right) + \sum_{n=1}^{N_R}\left[K_{OE_{n,i}} \, \mathrm{E}_{A_{n,i}} \right]. \tag{197}$$

This term is the flux exiting the right hand side of a spatial cell in a single direction. It is calculated by adding the contributions from fine angular quadrature fluxes entering the left hand side of the spatial cell, scattered within the cell, or emitted within the cell multiplied by their respective spatial quadrature coefficients. Similarly the second term of equation (195) is the flux exiting the left edge

$$\widehat{\psi}_{2,i-\frac{1}{2}} = \sum_{n=N_R+1}^{N}\left(K_{OI_{n,i}} \ \psi_{n,i+\frac{1}{2}} \right) + \sum_{n=N_R+1}^{N}\left[K_{OS_{n,i}} \sum_{n'=1}^{N} \sigma_{s_{n',n,i}} \psi_{n',i} \right] + \sum_{n=N_R+1}^{N}\left[K_{OE_{n,i}} \, E_{A_{n,i}} \right]. \tag{198}$$

The first term of equation (196) is cell average flux streaming rightward

$$\widehat{\psi}_{1,i} = \sum_{n=1}^{N_R}\left(K_{AI_{n,i}} \ \psi_{n,i-\frac{1}{2}} \right) + \sum_{n=1}^{N_R}\left[K_{AS_{n,i}} \sum_{n'=1}^{N} \sigma_{s_{n',n,i}} \psi_{n',i} \right] + \sum_{n=1}^{N_R}\left[K_{AE_{n,i}} E_{A_{n,i}} \right]. \tag{199}$$

It is calculated by adding the contributions from fine quadrature fluxes entering the left hand side of the spatial cell, scattered within the cell, or emitted within the cell multiplied by their respective transport coefficients. Similarly the second term resulting from equation (196) is the cell average flux streaming leftward

$$\begin{aligned}\widehat{\psi}_{2,i} = & \sum_{n=N_R+1}^{N}\left(K_{AI_{n,i}}\ \psi_{n,i+\frac{1}{2}}\right) \\ & + \sum_{n=N_R+1}^{N}\left[K_{AS_{n,i}}\sum_{n'=1}^{N}\sigma_{s_{n',n,i}}\psi_{n',i}\right] \\ & + \sum_{n=N_R+1}^{N}\left[K_{AE_{n,i}}E_{A_{n,i}}\right].\end{aligned} \tag{200}$$

The goal is to transform the transport equations, (175) and (176), which have N directions and are not practical to solve into equivalent equations with only two directions that are practical to solve. This transformation can be done by multiplying equations (197) through (200) by an appropriately chosen factor, one , obtained from equations (177) through (184). As an example, equation (197) and (198) can be written as

$$\widehat{\psi}_{1,i+\frac{1}{2}} = \sum_{n=1}^{N_R}\left(K_{OI_{n,i}} \frac{\psi_{n,i-\frac{1}{2}}}{\sum_{n=1}^{N_R}\psi_{n,i-\frac{1}{2}}} \right)\widehat{\psi}_{1,i-\frac{1}{2}}$$
$$+\sum_{n=1}^{N_R}\left(K_{OS_{n,i}} \frac{\sum_{n'=1}^{N}\sigma_{s_{n',n,i}}\psi_{n',i}}{\sum_{n=1}^{N_R}\sum_{n'=1}^{N}\sigma_{s_{n',n,i}}\psi_{n',i}} \right)\widehat{S}_{A_{1,i}} \qquad (201)$$
$$+\sum_{n=1}^{N_R}\left[K_{OE_{n,i}} \frac{\mathrm{E}_{A_{n,i}}}{\sum_{n=1}^{N_R}E_{A_{n,i}}} \right]\widehat{E}_{A_{1,i}},$$

$$\widehat{\psi}_{2,i-\frac{1}{2}} = \sum_{n=N_R+1}^{N}\left(K_{OI_{n,i}} \frac{\psi_{n,i+\frac{1}{2}}}{\sum_{n=N_R+1}^{N}\psi_{n,i+\frac{1}{2}}} \right)\widehat{\psi}_{2,i+\frac{1}{2}}$$
$$+\sum_{n=N_R+1}^{N}\left[K_{OS_{n,i}} \frac{\sum_{n'=1}^{N}\sigma_{s_{n',n,i}}\psi_{n',i}}{\sum_{n=N_R+1}^{N}\sum_{n'=1}^{N}\sigma_{s_{n',n,i}}\psi_{n',i}} \right]\widehat{S}_{A_{2,i}} \qquad (202)$$
$$+\sum_{n=N_R+1}^{N}\left[K_{OE_{n,i}} \frac{E_{A_{n,i}}}{\sum_{n=N_R+1}^{N}E_{A_{2,i}}} \right]\widehat{E}_{A_{2,i}}.$$

Note that these two equations are in the form of equations (42) and (43) for two directions. However, the transport coefficients are not calculated from the coarse angular quadrature. They are calculated from the fine angular quadrature transport coefficients and fluxes. The two direction transport effective spatial quadrature coefficients are

$$K_{OI_{1,i}} = \sum_{n=1}^{N_R} \left(K_{OI_{n,i}} \frac{\psi_{n,i-\frac{1}{2}}}{\sum_{n=1}^{N_R} \psi_{n,i-\frac{1}{2}}} \right), \tag{203}$$

$$K_{OS_{1,i}} = \sum_{n=1}^{N_R} \left(K_{OS_{n,i}} \frac{\sum_{n'=1}^{N} \sigma_{s_{n',n,i}} \psi_{n',i}}{\sum_{n=1}^{N_R} \sum_{n'=1}^{N} \sigma_{s_{n',n,i}} \psi_{n',i}} \right), \tag{204}$$

$$K_{OE_{1,i}} = \sum_{n=1}^{N_R} \left(K_{OE_{n,i}} \frac{\mathrm{E}_{A_{n,i}}}{\sum_{n=1}^{N_R} E_{A_{n,i}}} \right), \tag{205}$$

$$K_{OI_{2,i}} = \sum_{n=N_R+1}^{N} \left(K_{OI_{n,i}} \frac{\psi_{n,i+\frac{1}{2}}}{\sum_{n=N_R+1}^{N} \psi_{n,i+\frac{1}{2}}} \right), \tag{206}$$

$$K_{OS_{2,i}} = \sum_{n=N_R+1}^{N} \left(K_{OS_{n,i}} \frac{\sum_{n'=1}^{N} \sigma_{s_{n',n,i}} \psi_{n',i}}{\sum_{n=N_R+1}^{N} \sum_{n'=1}^{N} \sigma_{s_{n',n,i}} \psi_{n',i}} \right), \tag{207}$$

$$K_{OE_{2,i}} = \sum_{n=N_R+1}^{N} \left(K_{OE_{n,i}} \frac{E_{A_{n,i}}}{\sum_{n=N_R+1}^{N} E_{A_{2,i}}} \right). \tag{208}$$

Each of these effective transport coefficients can be thought of as a weighted sum of N-direction spatial quadrature coefficients. The weights are the terms in each of the brackets of the above equations that multiply the fine angle transport coefficients. Note that the sum of each of these terms over its respective summation index is one. For instance the sum of the weights of equation (203) are

$$1 = \sum_{n=1}^{N_R} \left(\frac{\psi_{n,i-\frac{1}{2}}}{\sum_{n=1}^{N_R} \psi_{n,i-\frac{1}{2}}} \right). \tag{209}$$

For this reason the array of weights for the positive direction fluxes denoted by

$$\begin{bmatrix} \dfrac{\psi_{1,i-\frac{1}{2}}}{\sum_{n=1}^{N_R} \psi_{n,i-\frac{1}{2}}} \\ \vdots \\ \dfrac{\psi_{N_R,i-\frac{1}{2}}}{\sum_{n=1}^{N_R} \psi_{n,i-\frac{1}{2}}} \end{bmatrix} \tag{210}$$

represents a distribution of flux over the positive direction hemisphere. The array of edge flux weights for the positive direction for cell i will be denoted by the more convenient notation

$$\vec{f}_{+,i} = \begin{bmatrix} f_{1,i-\frac{1}{2}} \\ \vdots \\ f_{N_R,i-\frac{1}{2}} \end{bmatrix} = \begin{bmatrix} \dfrac{\psi_{1,i-\frac{1}{2}}}{\sum_{n=1}^{N_R} \psi_{n,i-\frac{1}{2}}} \\ \vdots \\ \dfrac{\psi_{N_R,i-\frac{1}{2}}}{\sum_{n=1}^{N_R} \psi_{n,i-\frac{1}{2}}} \end{bmatrix}. \tag{211}$$

Additionally, the array of edge flux weights for the negative direction for cell i will be denoted by

$$\vec{f}_{-,i} = \begin{bmatrix} f_{N_R+1,i+\frac{1}{2}} \\ \vdots \\ f_{N,i+\frac{1}{2}} \end{bmatrix} = \begin{bmatrix} \dfrac{\psi_{N_{R+1},i+\frac{1}{2}}}{\sum_{n=N_R+1}^{N} \psi_{n,i+\frac{1}{2}}} \\ \vdots \\ \dfrac{\psi_{N,i+\frac{1}{2}}}{\sum_{n=N_R+1}^{N} \psi_{n,i+\frac{1}{2}}} \end{bmatrix}. \tag{212}$$

The flux weight array for the cell average scattered source in the positive direction for cell i is

$$\vec{f}_{S_{+},i} = \begin{bmatrix} f_{S_{1},i} \\ \vdots \\ f_{S_{N_R},i} \end{bmatrix} = \begin{bmatrix} \dfrac{\sum_{n'=1}^{N} \sigma_{s_{n',1,i}} \psi_{n',i}}{\sum_{n=1}^{N_R} \sum_{n'=1}^{N} \sigma_{s_{n',n,i}} \psi_{n',i}} \\ \vdots \\ \dfrac{\sum_{n'=1}^{N} \sigma_{s_{n',N_R,i}} \psi_{n',i}}{\sum_{n=1}^{N_R} \sum_{n'=1}^{N} \sigma_{s_{n',n,i}} \psi_{n',i}} \end{bmatrix}. \tag{213}$$

The flux weight array for the cell average scattered source in the negative direction for cell i is

$$\vec{f}_{S_{-},i} = \begin{bmatrix} f_{SN_R+1,i} \\ \vdots \\ f_{SN,i} \end{bmatrix} = \begin{bmatrix} \dfrac{\sum_{n'=1}^{N} \sigma_{s_{n',N_R+1,i}} \psi_{n',i}}{\sum_{n=N_R+1}^{N} \sum_{n'=1}^{N} \sigma_{s_{n',n,i}} \psi_{n',i}} \\ \vdots \\ \dfrac{\sum_{n'=1}^{N} \sigma_{s_{n',N,i}} \psi_{n',i}}{\sum_{n=N_R+1}^{N} \sum_{n'=1}^{N} \sigma_{s_{n',n,i}} \psi_{n',i}} \end{bmatrix}. \tag{214}$$

The array of flux weights for the cell emission source in the positive direction for cell i is

$$\vec{f}_{E_{+,i}} = \begin{bmatrix} f_{E_{1,i}} \\ \vdots \\ f_{E_{N_R,i}} \end{bmatrix} = \begin{bmatrix} \dfrac{\mathrm{E}_{A_{1,i}}}{\sum_{n=1}^{N_R} E_{A_{n,i}}} \\ \vdots \\ \dfrac{\mathrm{E}_{A_{N_R,i}}}{\sum_{n=1}^{N_R} E_{A_{n,i}}} \end{bmatrix}. \tag{215}$$

The array of flux weights for the cell emission source in the negative direction for cell i is

$$\vec{f}_{E_{-,i}} = \begin{bmatrix} f_{E_{N_R+1,i}} \\ \vdots \\ f_{E_{N,i}} \end{bmatrix} = \begin{bmatrix} \dfrac{E_{A_{N_R+1,i}}}{\sum_{n=N_R+1}^{N} E_{A_{n,i}}} \\ \vdots \\ \dfrac{E_{A_{N,i}}}{\sum_{n=N_R+1}^{N} E_{A_{n,i}}} \end{bmatrix}. \tag{216}$$

If equations (199) and (200) are multiplied by the appropriate identity formed by rearranging equations (177) through (184), as was done for the edge flux the two components of the cell average flux are

$$\widehat{\psi}_{1,i} = \sum_{n=1}^{N_R} \left(K_{AI_{n,i}} \frac{\psi_{n,i-\frac{1}{2}}}{\sum_{n=1}^{N_R} \psi_{n,i-\frac{1}{2}}} \right) \widehat{\psi}_{1,i-\frac{1}{2}} + \sum_{n=1}^{N_R} \left[K_{AS_{n,i}} \frac{\sum_{n'=1}^{N} \sigma_{s_{n',n,i}} \psi_{n',i}}{\sum_{n=1}^{N_R} \sum_{n'=1}^{N} \sigma_{s_{n',n,i}} \psi_{n',i}} \right] \widehat{S}_{A_{1,i}} + \sum_{n=1}^{N_R} \left[K_{AE_{n,i}} \frac{\mathrm{E}_{A_{n,i}}}{\sum_{n=1}^{N_R} E_{A_{n,i}}} \right] \widehat{E}_{A_{1,i}}, \tag{217}$$

and

$$\widehat{\psi}_{2,i} = \sum_{n=N_R+1}^{N} \left(K_{AI_{n,i}} \frac{\psi_{n,i+\frac{1}{2}}}{\sum_{n=N_R+1}^{N} \psi_{n,i+\frac{1}{2}}} \right) \widehat{\psi}_{2,i+\frac{1}{2}} + \sum_{n=N_R+1}^{N} \left[K_{AS_{n,i}} \frac{\sum_{n'=1}^{N} \sigma_{s_{n',n,i}} \psi_{n',i}}{\sum_{n=N_R+1}^{N} \sum_{n'=1}^{N} \sigma_{s_{n',n,i}} \psi_{n',i}} \right] \widehat{\psi}_{2,i} + \sum_{n=N_R+1}^{N} \left[K_{AE_{n,i}} \frac{E_{A_{n,i}}}{\sum_{n=N_R+1}^{N} E_{A_{n,i}}} \right] \widehat{E}_{A_{2,i}}. \tag{218}$$

The resulting two-direction effective spatial quadrature coefficients for the contributions of edge flux scattered source and emission source to cell average source are

$$K_{AI_{1,i}} = \sum_{n=1}^{N_R} \left(K_{AI_{n,i}} \frac{\psi_{n,i-\frac{1}{2}}}{\sum_{n=1}^{N_R} \psi_{n,i-\frac{1}{2}}} \right), \tag{219}$$

$$K_{AS_{1,i}} = \sum_{n=1}^{N_R} \left(K_{AS_{n,i}} \frac{\sum_{n'=1}^{N} \sigma_{s_{n',n,i}} \psi_{n',i}}{\sum_{n=1}^{N_R} \sum_{n'=1}^{N} \sigma_{s_{n',n,i}} \psi_{n',i}} \right), \tag{220}$$

$$K_{AE_{1,i}} = \sum_{n=1}^{N_R} \left[K_{AE_{n,i}} \frac{\mathrm{E}_{A_{n,i}}}{\sum_{n=1}^{N_R} E_{A_{n,i}}} \right], \tag{221}$$

$$K_{AI_{2,i}} = \sum_{n=N_R+1}^{N} \left(K_{AI_{n,i}} \frac{\psi_{n,i+\frac{1}{2}}}{\sum_{n=N_R+1}^{N} \psi_{n,i+\frac{1}{2}}} \right), \tag{222}$$

$$K_{AS_{2,i}} = \sum_{n=N_R+1}^{N} \left(K_{AS_{n,i}} \frac{\sum_{n'=1}^{N} \sigma_{s_{n',n,i}} \psi_{n',i}}{\sum_{n=N_R+1}^{N} \sum_{n'=1}^{N} \sigma_{s_{n',n,i}} \psi_{n',i}} \right), \tag{223}$$

$$K_{AE_{2,i}} = \sum_{n=N_R+1}^{N} \left[K_{AE_{n,i}} \frac{E_{A_{n,i}}}{\sum_{n=N_R+1}^{N} E_{A_{n,i}}} \right]. \tag{224}$$

The weights used to collapse the fine angle average flux spatial quadrature coefficients are the same as the flux weights used to collapse the edge flux transport coefficients. Equations (203) through (224) provide a mechanism to collapse an N direction angular quadrature into an equivalent two direction angular quadrature then calculate edge flux and average flux values across the entire spatial domain. If the edge and average fluxes were, known these ratios could be correctly calculated and the number of particles exiting a cell edge can be calculated directly. Once this is done, the particles crossing a cell edge in the direction of either hemisphere of Figure 2 can be calculated. It remains to apportion this flux into each of the ordinates of the fine angle quadrature.

The flux and source weights already discussed provide the mechanism to apportion the coarse quadrature flux found from solution of the spatially coupled transport system into fine directions. $\tilde{A}$ is used to denote identify fine-angle fluxes calculated by apportioning a spatially-coupled coarse-angle flux. For instance, $\tilde{\psi}_{n,i-\frac{1}{2}}$, represents the apportioned flux in ordinate n at edge $i-\frac{1}{2}$. This flux is calculated by multiplying the corresponding coarse angle flux with its appropriate flux weight $\hat{\psi}_{m,i-\frac{1}{2}}\, f_{n,i-\frac{1}{2}}$. The array of positive direction flux is calculated by multiplying the positive direction coarse flux by the array of positive direction flux weights

$$\vec{\tilde{\psi}}_{in_{L_i}} = \hat{\psi}_{1,i-\frac{1}{2}}\ \vec{f}_{+,i-\frac{1}{2}} \quad , \tag{225}$$

$$\vec{\tilde{\psi}}_{in_{R_i}} = \hat{\psi}_{2,i+\frac{1}{2}}\ \vec{f}_{-,i+\frac{1}{2}} \quad , \tag{226}$$

An angle space distribution iteration is shown schematically in Figure 3. The iteration begins with approximate fine angle edge flux.

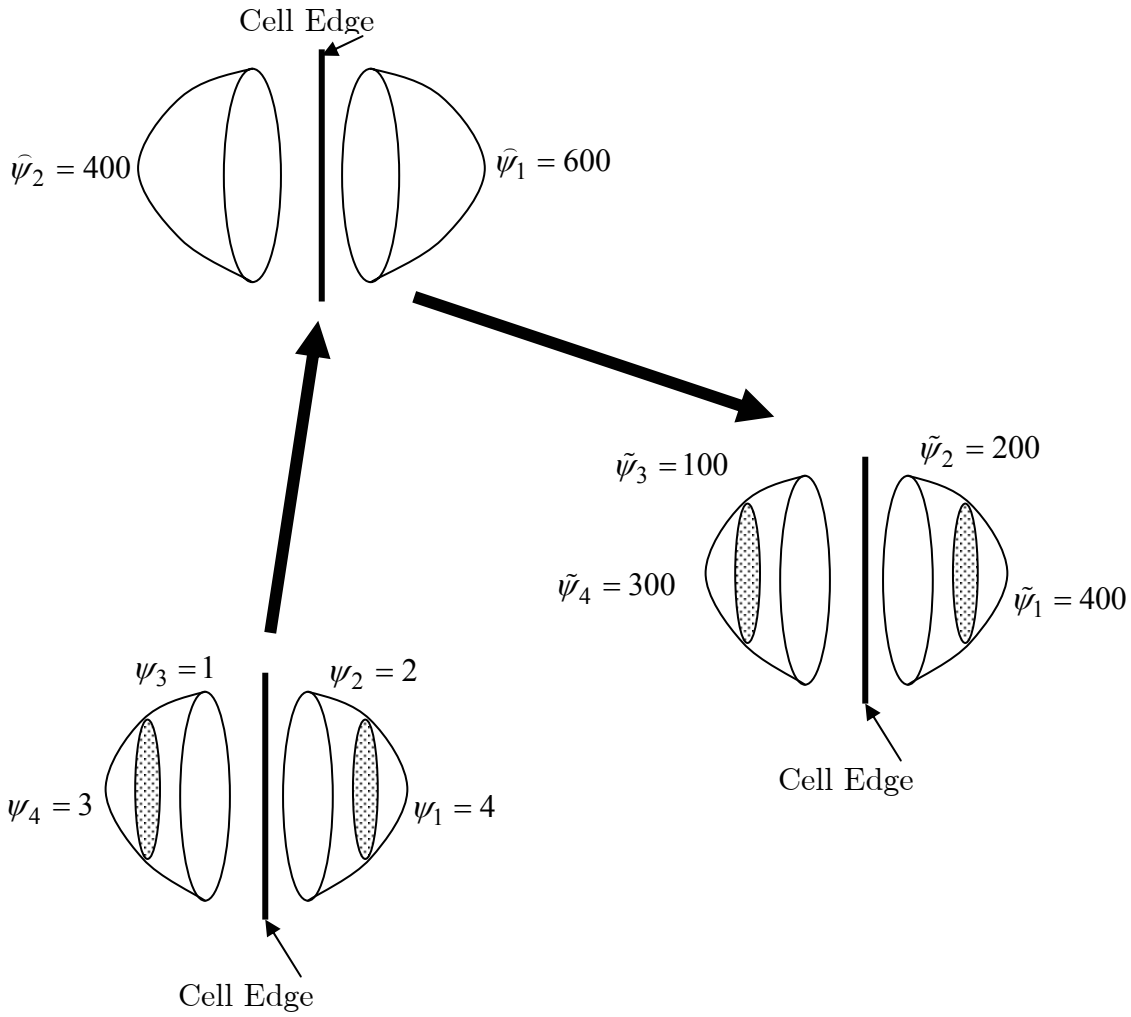

Figure 3: Apportioning two elements into N elements using Iteration Flux Weights

In Figure 3 there are four initial fine fluxes exiting the lower left hemispheres $\psi_1 = 4, \psi_2 = 2, \psi_3 = 1, \psi_4 = 3$. These fluxes have corresponding weights of $f_1 = \frac{4}{6}, f_2 = \frac{2}{6}, f_3 = \frac{1}{4}, f_4 = \frac{3}{4}$. These weights are used to collapse the fine angle transport coefficients to two directions for the center hemispheres. These two direction coefficients are then used in a spatially coupled system to calculate new fluxes that have accounted for particle scatter across the problem space. In this example this results in two flux values exiting the top hemispheres. This flux is then apportioned into the

original four directions using flux weights as shown in the right hemispheres. This results in four fluxes of $\psi_1 = 400, \psi_2 = 200, \psi_3 = 100, \psi_4 = 300$ in the example given. These flux solutions may not be correct, but they are of the right order of magnitude because they account for infinite particle scatters within spatial cells and across the spatial domain.

The use of approximate fine angle fluxes to collapse their respective spatial quadrature coefficients into effective spatial quadrature coefficients, followed by computation of transport coefficients, which are then used to compute spatially coupled two direction fluxes, which are apportioned back into improved estimates of fine angle flux, leads to an iterative scheme.

The vector of incoming cell edge fluxes for I spatial cells is estimated. Equation (112) is used to calculate cell outgoing edge fluxes and equation (111) is used to calculate cell average fluxes. These calculated fluxes are used to calculate flux weights with equations (211) through (216). A flux solution is then found using collapsed the effective transport coefficients for the flux exiting a hemisphere in the $+\mu$ direction and the flux exiting a hemisphere in the $-\mu$ direction. This two direction flux is then apportioned into the original N directions for a flux solution.

The flux solution arrived at with estimated flux, calculating approximate flux weights and approximate transport coefficients is an estimate that fully accounts for particle scatters across the spatial domain and within each spatial cell. The flux solution is not dependent on numerous source iterations to account for the scatters to estimate the scattering source. It fully accounts for particle scatters without iteration.

This straightforward numerical method using an estimated edge flux to collapse cell quadrature coefficients, use these to convert them to cell transport coefficients, calculate a two-direction spatially-coupled flux, then apportion that flux back into the fine ordinates to obtain an improved estimate of edge fluxes was the basis of the iteration scheme developed and investigated. This transport scheme had significant computational efficiency when compared with SI. Operationally this iteration works in the following way:

- calculate fluxes using two-direction effective transport coefficients,
- apportion this flux into fine ordinates as an initial estimate for edge fluxes,

- calculate updated fine angle edge fluxes,
- use these updated edge fluxes to calculate weights
- use the weights to collapse the spatial quadrature coefficients into effective two-ordinate spatial quadrature coefficients
- use these to form the effective two-ordinate transport coefficients
- apportion the flux calculated in this way into fine ordinates,
- calculate a better estimate of edge flux, weights and transport coefficients,
- proceed until convergence tolerance is met.

The entire scheme amounts to iteration on flux distribution and collapsed transport coefficients. The algorithm for the Angular-Spatial Distribution Iteration (ASDI) method using a step characteristic spatial quadrature is shown in Algorithm 4.

Initialize

Obtain an initial guess for cell edge, and zeroth moment angular flux

Use 2 direction quadrature to estimate cell coupling coefficients

Calculate 2 Direction angular flux

Apportion flux into to N directions

Repeat

update cell edge flux

solve fine angle resolution fluxes within spatial cells

use flux weights to generate improved coarse angle cell coupling coefficients

calculate spatially coupled coarse angle edge flux

The results of implementation of this algorithm in Fortran 95 code and comparison with SI are presented and discussed in the next chapter.

III. SC Experimental Results

I set out to design a transport method that is: robust, efficient (requires few iterations to converge), computationally effective (converges rapidly as measured by compute time), remains so when confronted with material discontinuities and is readily parallelizable. After deriving the method, developing the algorithms and implementing these algorithms in FORTRAN code I designed experiments to test 4 of the 5 desirable characteristics. I designed experiments to test the methods accuracy, effectiveness and computationally efficiency first without material discontinuities then with material discontinuities. I did not test parallelizability leaving this for future research.

I first experimented with an optically thick homogeneous material. I varied this homogeneous material from absorber (low scattering ratio) to scatterer (scattering ratio nearly one) in order to test ASDI against SI for two types of problems: one in which SI converged readily and one for which it converged slowly.

In the second experiment I investigated the effect of periodic material discontinuity on the comparative performance of ASDI. To do this I chose two materials of the same dimension. I placed an emission source in one material and no source in the other material. Both materials were 1 MFP wide. The emitter had a scattering ratio of one. The non-emitter's scattering ratio varied from 0.0 to 1.0 as in the homogeneous material. This two material pattern was repeated 10 times creating a periodic material discontinuity.

In addition to scattering ratio I further investigated the effect of spatial refinement, angular refinement and convergence criterion on robustness, effectiveness, and efficiency for both the homogeneous and periodic problems. I did this by setting the scattering ratio to 0.98 in the homogeneous material of problem 1 and the non-emitter of problem 2 instead of allowing this parameter to vary. The parameters I then varied in turn were spatial refinement, angular refinement and convergence tolerance.

I tested ASDI's accuracy by checking its solution against a benchmark to ensure it met the convergence tolerance required. The first benchmark I used was an

unaccelerated SI allowed to converge to the same convergence tolerance as ASDI. This provided a straightforward and reliable benchmark but only for test problems that were absorptive in which SI did not falsely converge. For those problems in which SI did falsely converge I took advantage of SI's ability to recognize a correct answer instead of its ability to calculate a correct answer. First an initial guess of zero was used and a conventional SI solution was found. This solution could be off by as much as four orders of magnitude because of false convergence. In this case the flux solution was discarded but the iterations required to obtain the solution were recorded. I then input ASDI solution to SI as an initial guess and allowed SI to iterate the same number of times it used to obtain its falsely converged solution. My assumption was that SI would recognize a fixed point. I allowed SI to iterate the same number of times it took to obtain its falsely converged solution to ensure that it had enough iteration to drift away from the ASDI solution if the initial value (i.e. the ASDI solution) was not a fixed point. For instance if SI required 100000 iterations to converge on an answer I recorded this but discarded its flux solution. I then passed SI the ASDI solution and allowed it to iterate 100000 times without checking it for convergence. After completing these 100000 iterations the new SI (SI_ASDI) solution was compared with the ASDI solution using $\varepsilon_{\text{SRD}}(\text{ASDI,SI\_ASDI})$. This symmetric relative difference was then compared with the desired convergence tolerance. If it was tighter than this desired convergence tolerance it demonstrated reliable accuracy. After ensuring accuracy effectiveness was tested, I examined computational efficiency. I tested this by comparing ASDI and SI compute times.

Problem 1 Optically Thick Homogeneous Material

The first test problem studied is a 100 cm thick homogeneous slab with a vacuum boundary on the right, a symmetry boundary on the left, a uniform isotropic source,

source, and a total cross section of $1.0\,\mathrm{cm}^{-1}$. A diagram of this problem is shown in Figure 4.

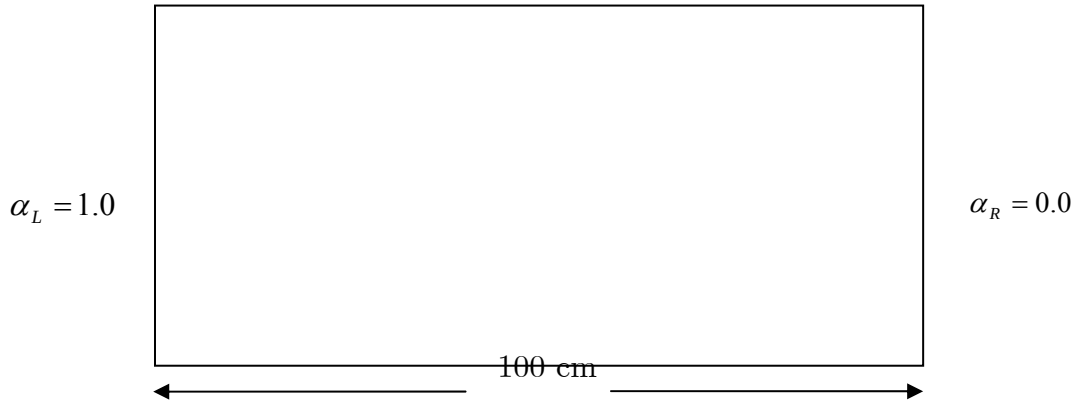

Figure 4 Problem 1

In the study of this problem and other problems the terms refinement factor and scattering ratio fraction are introduced. Refinement factor is an integer that describes the number of partitions chosen for the spatial domain in a mesh. For instance the spatial domain of problem 1 was 100 cm. Refinement factors used were {1, 2, 4, 8, 10, 16, 32, 64, 100,128} designating the number of cell partitions. These refinement factors correspond with cell widths of $\{100, 50, 25, 12.5, 10, \frac{100}{16}, \frac{100}{32}, \frac{100}{64}, 1, \frac{100}{128}\}$ cm for problem 1. Scattering ratio fraction is a real number used as a coefficient that multiplies a base scattering ratio defined by the user. Scattering ratio fraction is used order to vary problem scattering ratio over a range of interest for the numerical experiment. For instance, in problem 1 the base scattering ratio was 1.0. The scattering ratio fraction varied from 0.0 through 1.0. These factors were used to vary the parameters under study across a full range of interest.

The ASDI method provides a useful transport tool only if it provides reliable and usably accurate numerical solutions. The first experiment tested the ASDI solution robustness as scattering ratio varied. Figure 5 displays two plots. These are the symmetric relative difference versus scattering ratio of the ASDI solution and the SI solution (ASDI_SI) and of the ASDI solution and the SI solution after being given the ASDI solution (ASDI_SI-ASDI). The convergence tolerance chosen was 10^{-6} for both

SI and ASDI. At a scattering ratio of 0.6 the ASDI and SI solutions differ by more than the chosen convergence tolerance. This difference increases as the scattering ratio increases. Both methods agree within the convergence tolerance for scattering ratios below 0.6. These plots show that SI produces unreliable answers at scattering ratios as low as 0.6 but ASDI continues to provide the accurate answers are validated by SI's fixed point recognition for all scattering ratios.

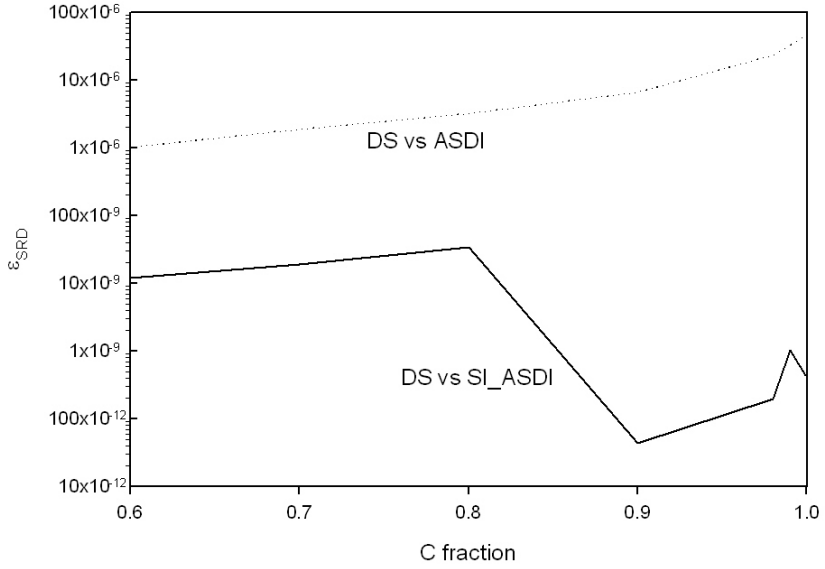

Figure 5: Symmetric Relative Difference ε_{SRD} between the ASDI solution and the SI solution as scattering ratio varies. Angular quadrature is DE-8, refinement is 50 ($\sigma\Delta x = 2\,\mathrm{MFPs}$), convergence tolerance is 10^{-6}.

Figure 6 shows iteration count versus scattering ratio (c) with an angular refinement of 8, a mesh width of 2 MFPs and a convergence tolerance of 10^{-6}. SI iteration count increases with c, climbing steeply as c approaches unity. This demonstrates the classic weakness of SI for diffusive problems. The ASDI solution converges in two or three iterations regardless of scattering ratio demonstrating its usefulness especially for diffusive problems.

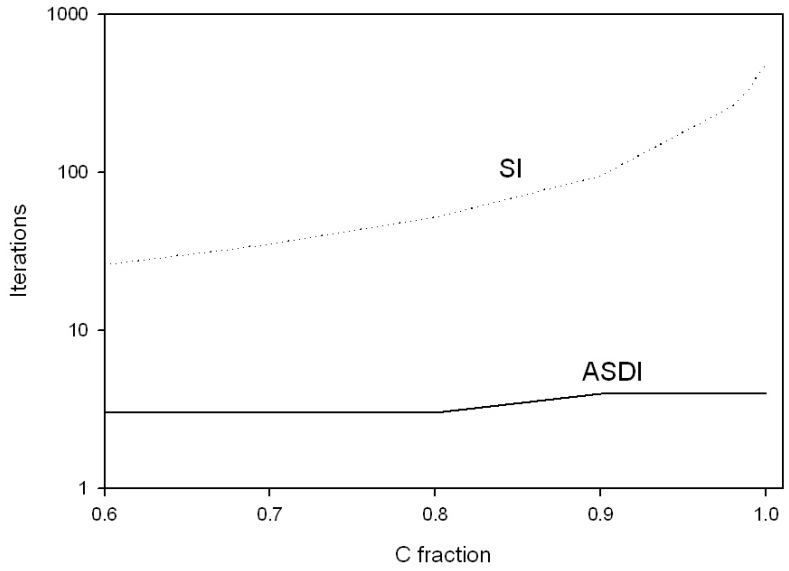

Figure 6 Plot of iteration count versus scattering ratio. Angular quadrature is DE-8, refinement is 50 ($\Delta x = 2\,MFPs$), convergence tolerance is 10^{-6}.

The low iteration count of the ASDI method displayed in Figure 6 is encouraging. It is not a practical improvement over SI unless computational cost is also reduced. Figure 7 displays compute time versus scattering ratio. The amount of compute time needed by the ASDI method is insensitive to the scattering ratio and compares favorably to SI even when SI converges rapidly. This demonstrates that we have not paid excessive computational efficiency costs to obtain the method's desirable robustness and effectiveness.

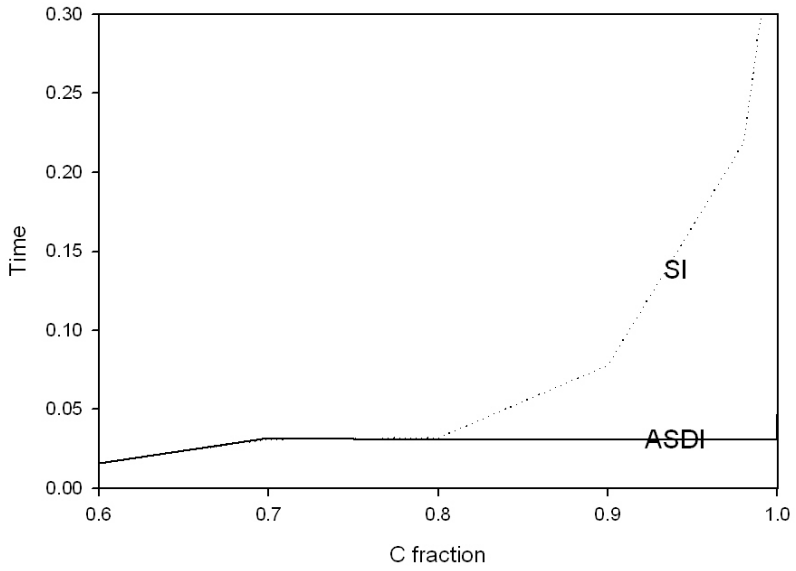

Figure 7 Plot of compute time (seconds) versus scattering ratio. Angular quadrature is DE-8, refinement is 50 ($\sigma\Delta x = 2\,MFPs$), convergence tolerance is 10^{-6}.

The results shown in Figure 5 through Figure 7 demonstrate the effect of scattering ratio on the ASDI and SI methods. These results were obtained with a fixed refinement of 50 mesh cells ($\Delta x = 2.0\,\text{cm}$), convergence tolerance fixed at 10^{-6}, and angular quadrature fixed at $n = 8$. Spatial refinement, angular refinement, and convergence tolerance are also parameters that are expected to have an impact on robustness, effectiveness, and efficiency of a method. The next series of plots investigates the effect of changing these parameters. These three parameters were studied with a scattering ratio of 0.98 making the homogeneous material a good scatterer. This scattering ratio was chosen to test the performance of ADSI in a diffusive problem.

Figure 8 shows the relative difference between SI and ASDI solutions as the spatial mesh is refined. The difference between the answers is greater than the convergence tolerance because with a scattering ratio of 0.98 SI suffers from false convergence. If SI is fed the ASDI solution it again recognizes this solution as a fixed point for all spatial refinements.

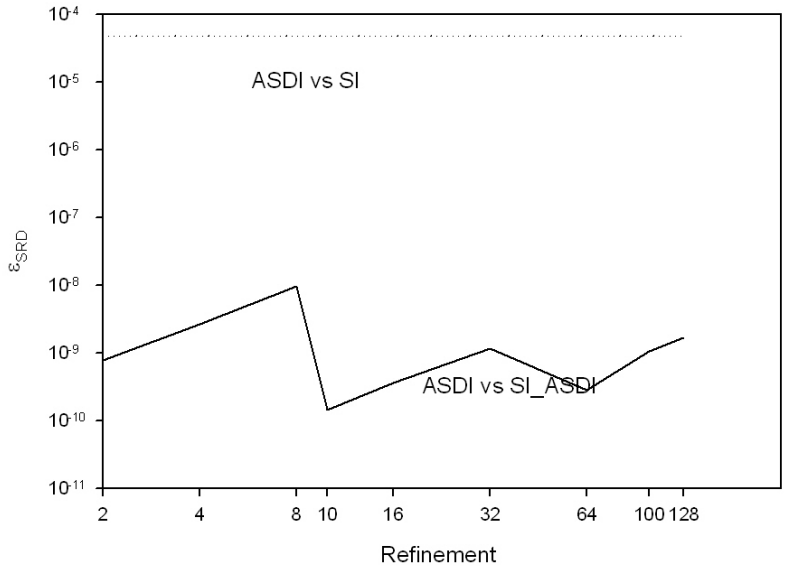

Figure 8 Plot of Symmetric Relative Difference ε_{SRD} between ASDI solution and SI solutions for as cell mesh is refined. Angular quadrature is DE-8, scattering ratio is 1.0, convergence tolerance is 10^{-6}.

SI recognition of the ASDI solution as a fixed point for all spatial refinements provides convincing evidence of the accuracy of its solution. I was able to further test this accuracy because by computing and comparing the ASDI convergence rate with the known convergence rate of SC. An analytic solution was available for problem 1. This was done for a DE-4 angular quadrature and a scattering ratio of 1.0 with spatial refinement varying from 1000 (cell width = $1.25\text{x}10^{-2}$cm) through 10 (cell width=10 cm). ASDI solutions are not expected to be the same as the analytic solution because ASDI is a numerical approximation of the analytic solution dependent on mesh refinement. However, because SC is known to be second order convergent in space the method can be checked against the analytic solution to determine if the order of convergence is 2. Figure 9 shows symmetric relative difference (ε_{SRD}) between the ASDI solution and an exact solution plotted against the spatial mesh refinement factor (R_F) on a Log-Log graph for a scattering ratio of 1.0. Figure 10 shows this for a scattering ratio of 0.9. ε_{SRD} appears as a straight line on both plots whose slope is two.

A line with a slope of two, which is the convergence order of SC, has been overlaid on the data plot. This agreement of ASDI's convergence rate with the known SC convergence rate for a scattering ratio of 1.0 and 0.9 combined with SI recognition of ASDI solutions as fixed points demonstrate the method's robustness.

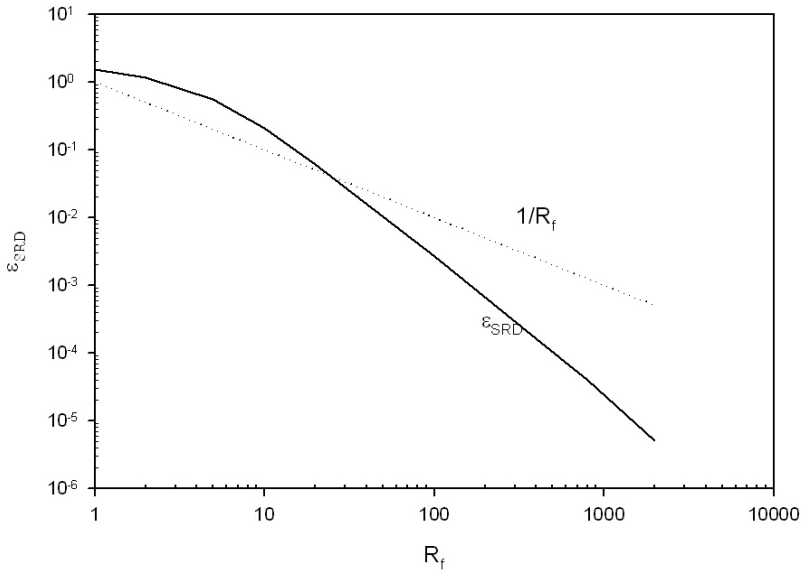

Figure 9: Plot of Symmetric Relative Difference ε_{SRD} between the ASDI solution and an analytic solution as cell mesh is refined between 10 MFPs and 0.1 MFPs. Angular quadrature is DE-8, scattering ratio is 1.0, convergence tolerance is 10^{-6}.

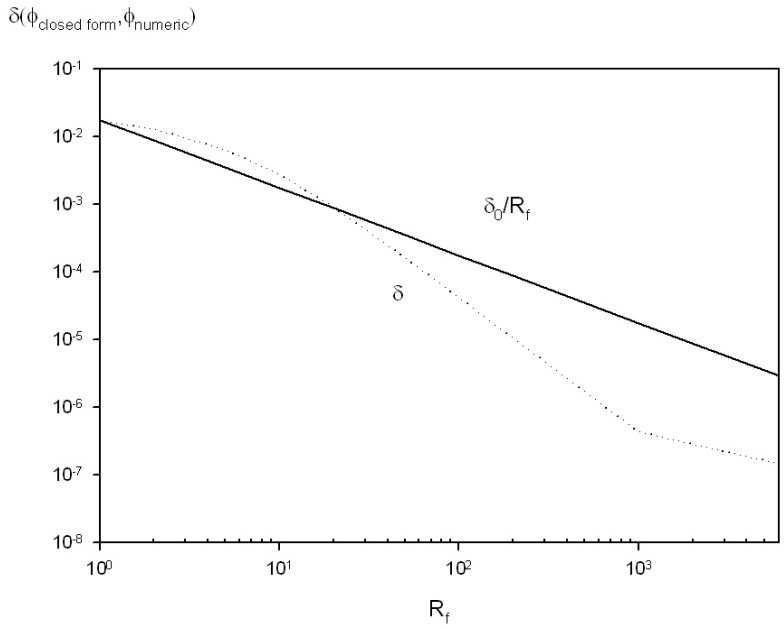

Figure 10: Plot of Symmetric Relative Difference ε_{SRD} between the ASDI solution and an analytic solution 1 as cell mesh is refined between 10 MFPs and 0.1 MFPs. Angular quadrature is DE-8, scattering ratio is 0.9, convergence tolerance is 10^{-6}.

Figure 11 shows the iteration count of the ASDI and SI methods as the mesh is refined. SI iteration remains flat, at 500 iterations, as the mesh is refined and ASDI iteration count increases from 4 iterations for a coarse mesh to 17 iterations for a fine mesh indicating ASDI is an effective method. SI appears insensitive to the cell refinement. I drew no conclusions about this SI characteristic from this because of its false convergence.

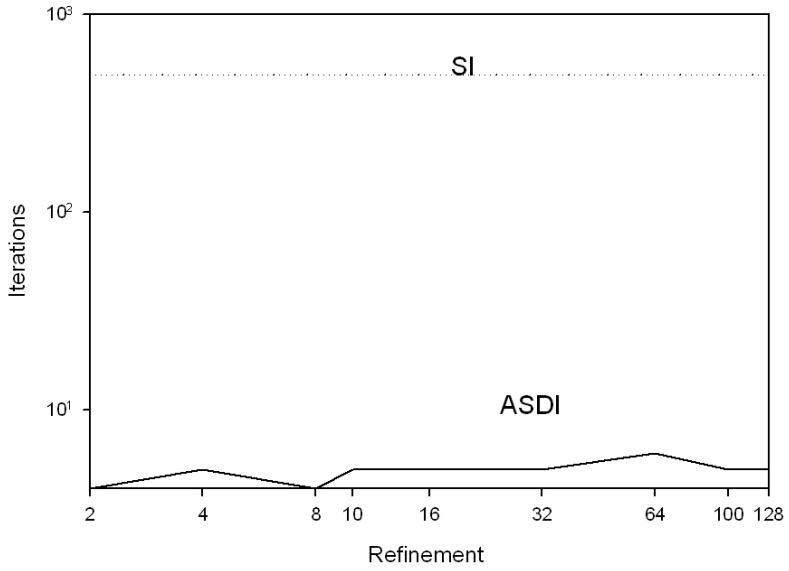

Figure 11 Plot of iteration count as cell mesh is refined. Angular quadrature is DE-8, scattering ratio is 1.0, convergence tolerance is 10^{-6}.

Figure 12 shows the compute times required for the SI and ASDI solutions as the spatial mesh is refined. The spatial refinement increases compute time for both methods. ASDI requires less compute time than SI for the scattering ratio chosen. This indicates that ASDI will not require disproportionately more time than SI regardless of mesh size. The true value of ASDI is that it converges to the correct solution without requiring large compute time, something that SI can not do.

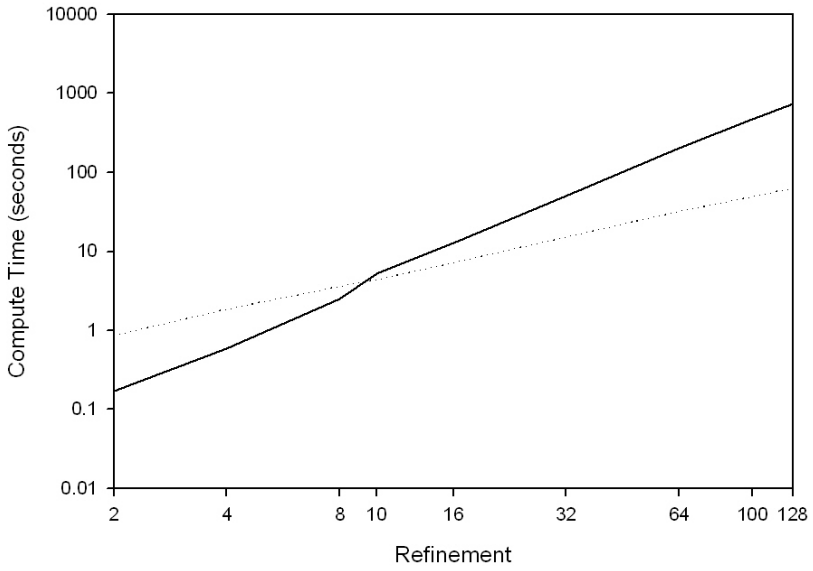

Figure 12 Plot of compute time required for the ASDI and SI solutions as cell mesh is refined. Angular quadrature is DE-8, scattering ratio is 1.0, convergence tolerance is 10^{-6}.

The convergence tolerance used to test previous problems was 10^{-6} on angular flux. This is a fairly tight convergence tolerance and it is suitable for most engineering applications. However some applications may require tighter tolerances. The effect of tightening convergence tolerance from 10^{-6} to 10^{-11} on symmetric relative difference, iteration count, and compute time is shown next. Figure 13 shows that the accuracy of the converged SI solution does not meet the accuracy required by the specified convergence tolerance regardless of how tight that tolerance is, whereas the ASDI method continues to provide reliably accurate solutions for any tolerance without round off error or instability. Examination of Figure 14 and Figure 15 reveals that this accuracy is achieved with modest increase in iterations required or compute time.

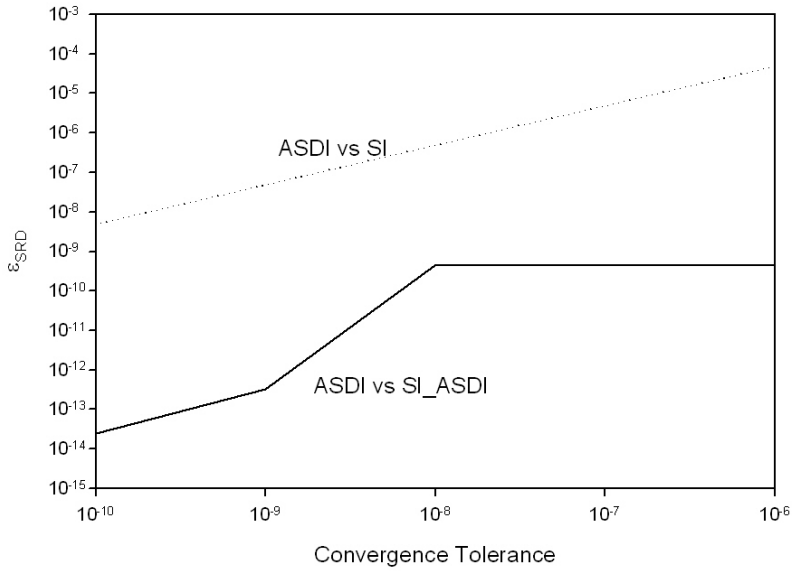

Figure 13 Plot of symmetric relative difference versus convergence tolerance. Angular quadrature is DE-8, scattering ratio is 1.0, cell size is 2 MFPs.

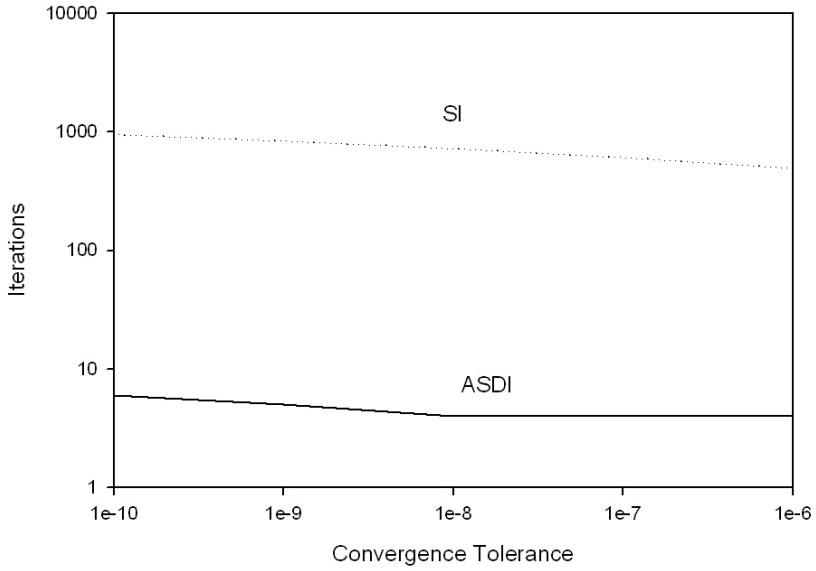

Figure 14 Plot of iterations versus convergence tolerance for ASDI and SI. Angular quadrature is DE-8, scattering ratio is 1.0, cell size is 2 MFPs.

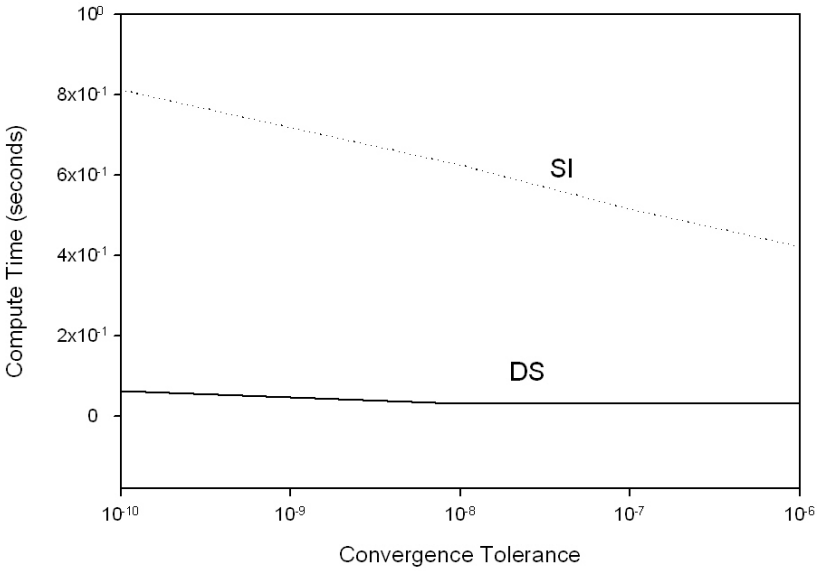

Figure 15 Plot of compute time versus convergence tolerance for ASDI and SI.

Angular quadrature is DE-8, scattering ratio is 1.0, cell size is 2 MFPs.

The effect of increasing angular refinement is shown in Figure 16 through Figure 18 shows that SI remains inaccurate and has increased computational cost as the angular quadrature is refined. ASDI continues to provide reliably accurate solutions without an increase in iteration count or compute time beyond an angular quadrature of 2. ASDI achieves a quick solution for an angular quadrature of 2 because its global spatial solution was designed with this angular quadrature. Such a coarse angular quadrature is not likely to meet most engineering needs. However ASDI's rapid convergence for even fine angular quadratures indicates usefulness for engineering problems requiring higher angular refinement.

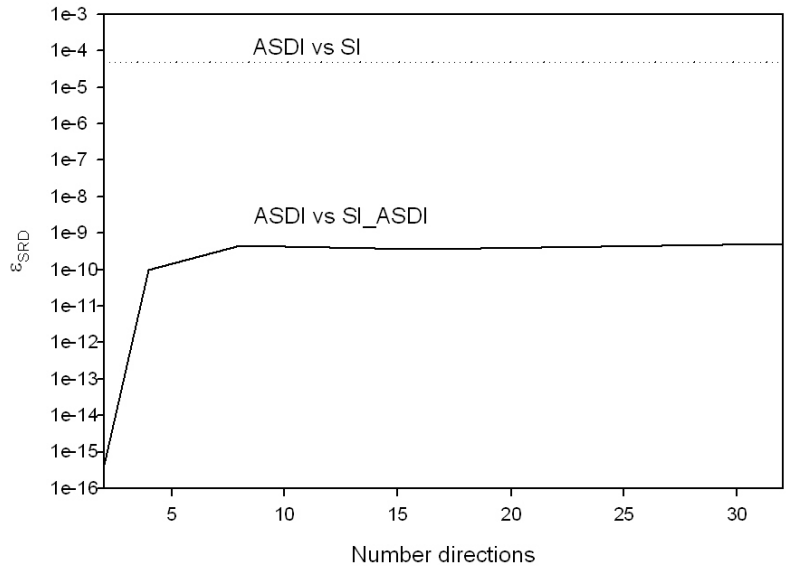

Figure 16 Plot of symmetric relative difference versus angular quadrature. Convergence tolerance is 10^{-6} scattering ratio is 1.0, cell size is 2 MFPs.

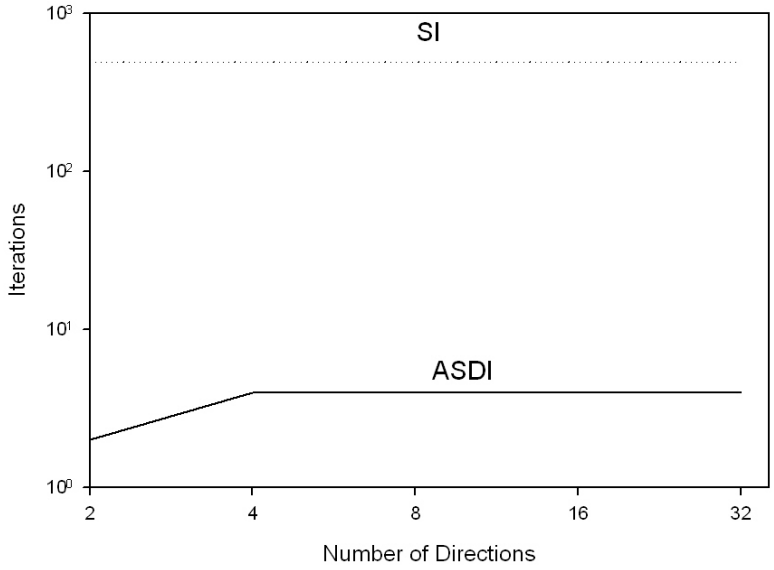

Figure 17 Plot of iterations versus angular quadrature for ASDI and SI. Convergence tolerance is 10^{-6} scattering ratio is 1.0, cell size is 2 MFPs.

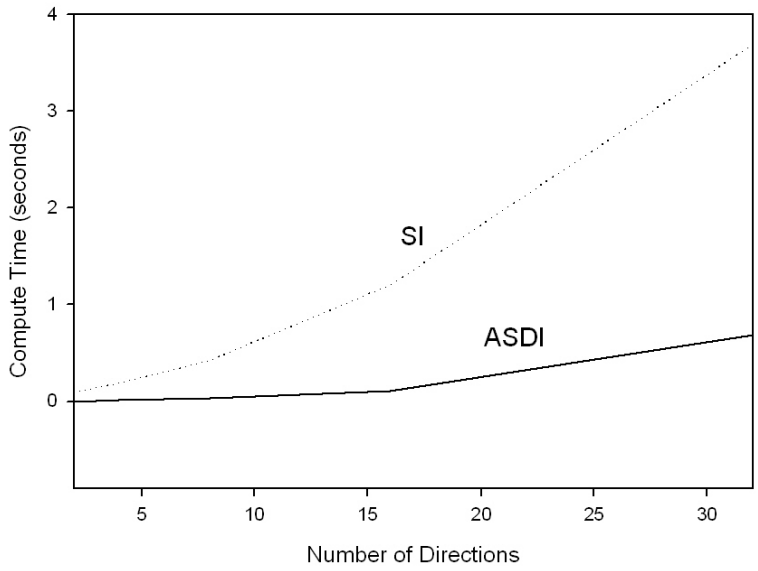

Figure 18 Plot of compute time versus angular quadrature for ASDI and SI.

Convergence tolerance is 10^{-6} scattering ratio is 1.0, cell size is 2 MFPs.

This section demonstrated the strength of the ASDI method for a homogeneous material. The most important characteristic examined was accuracy for each of the parameters studied. Each experiment showed that ASDI was reliably accurate within the convergence tolerance required whereas SI was not. This reliable accuracy across all parameters studied demonstrates that the method is robust for this homogeneous problem. The next section examines the method's performance when applied to a heterogeneous material.

Periodic: Two Regions Repeated 10 Times

The second test problem investigated was slab with a symmetry boundary on the left side and a vacuum boundary on the right side. Two materials of 1 cm cell width are

placed side by side. This two material pattern is repeated 10 times for a total length of 20 cm. Material I had a total cross section of $1.0\,\mathrm{cm}^{-1}$, a scattering ratio of 1.0, and a uniform source of $1.0\,\mathrm{cm}^{-3}$. Its material properties remain fixed for all experiments. Material II has a total cross section of $1.0\,\mathrm{cm}^{-1}$, a baseline scattering ratio of 1.0, and no source. Material II's parameters were varied during the experiments. A diagram of these two materials is shown in Figure 19.

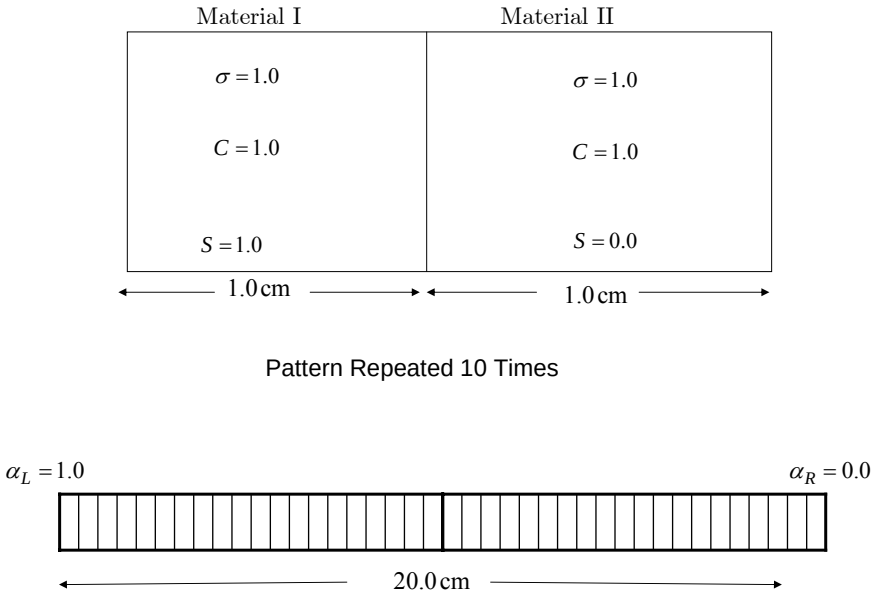

Figure 19 Problem 2

In the next set of experiments I tested the method for accuracy, effectiveness, and efficiency for varying scattering ratio fraction, refinement factor, convergence tolerance and angular refinement as was done in problem 1.

The first set of experiments for problem 2 tested the ASDI method's accuracy, effectiveness and efficiency versus scattering ratio fraction in Material II. Scattering ratio fraction was varied from 0.0 to 1.0. Angular refinement for this experiment was 8, refinement factor was 1 and convergence tolerance was 10^{-6}.

Accuracy is the first parameter presented. Figure 20 displays the symmetric relative difference between ASDI and SI ($\varepsilon_{\text{SRD}}(\text{ASDI,SI\_ASDI})$) and between ASDI and SI given the ASDI solution ($\varepsilon_{\text{SRD}}(\text{ASDI,SI\_ASDI})$). The plots show that ASDI provides reliably accurate solutions for all scattering ratios while SI provides reliably accurate solutions only through scattering ratios of 0.6.

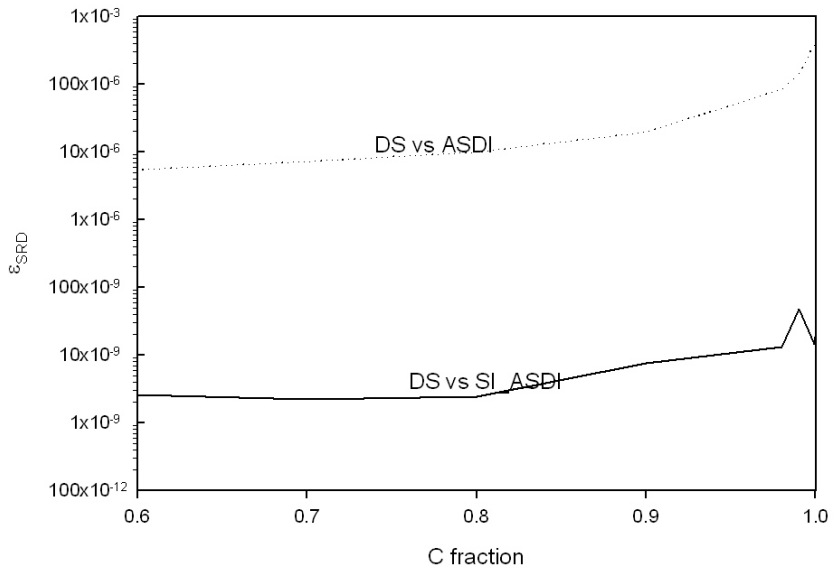

Figure 20: Symmetric Relative Difference ε_{SRD} between the ASDI solution and the SI solution as scattering ratios vary. Angular quadrature is DE-8, convergence tolerance is 10^{-6}, refinement is 50.

The effectiveness of the method is tested next. Figure 21 shows the method iteration count versus scattering ratio fraction for material II. This plot shows that ASDI converges in four or five iterations regardless of scattering ratio demonstrating its effectiveness for diffusive heterogeneous materials. Iteration count for SI increases with scattering ratio. This count climbs steeply as scattering ratio approaches 1.0.

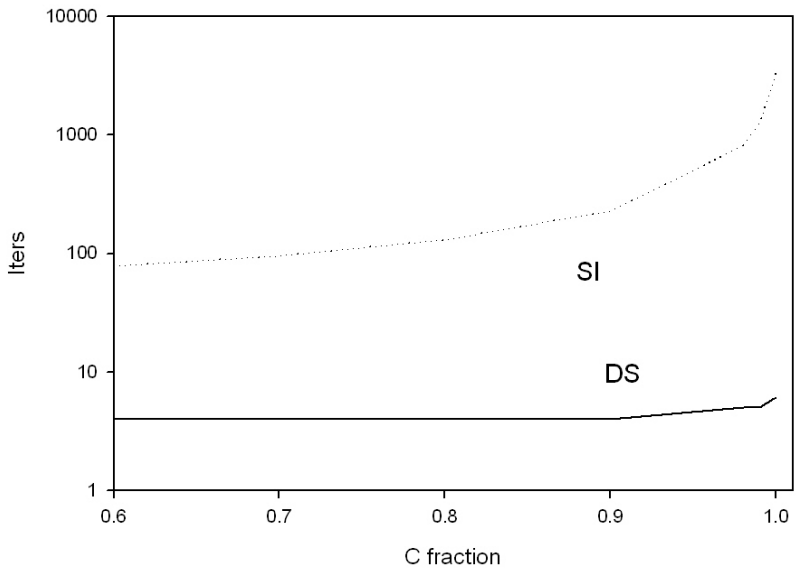

Figure 21: Plot of iteration count versus scattering ratio fraction. Angular quadrature is DE-8, convergence tolerance is 10^{-6}, refinement is 50.

Efficiency of the method is tested next. Figure 22 shows compute time versus scattering ratio fraction for material II. This figure shows that ASDI compute time is less than 0.1 seconds for all scattering ratios tested. Comparison of the ASDI and SI compute times demonstrate that ASDI is more computationally efficient than SI even when material II is a strong absorber and SI converges rapidly. The figure also shows that in materials that are strong scatterers SI compute time climbs rapidly.

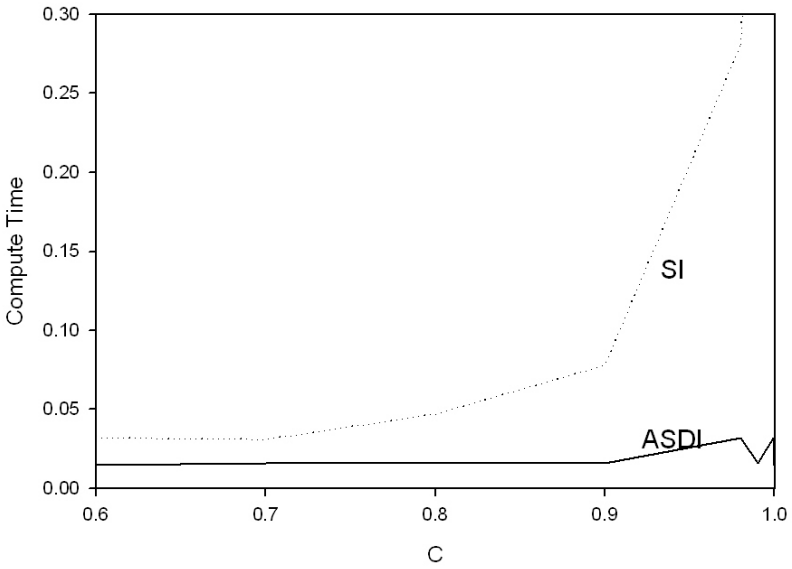

Figure 22: Plot of compute time (seconds) versus scattering ratio. Angular quadrature is DE-8, convergence tolerance is 10^{-6}, refinement is 50.

The next set of experiments demonstrate method accuracy, effectiveness and efficiency while refinement factor varies for material II. Scattering ratio for material II was fixed at 1.0. This tested ASDI in a highly diffusive material. A material discontinuity occurs even though cross sections and scattering ratios are the same because intrinsic sources are emitted only in material I. The refinement factor for material II was varied between 1 and 66.

Accuracy was tested first. Figure 23 displays the symmetric relative difference between ASDI and SI ($\varepsilon_{\text{SRD}}(\text{ASDI,SI\_ASDI})$) and between ASDI and SI given the ASDI solution ($\varepsilon_{\text{SRD}}(\text{ASDI,SI\_ASDI})$). The plots show that ASDI provides reliably accurate solutions for all refinement factors but SI does not.

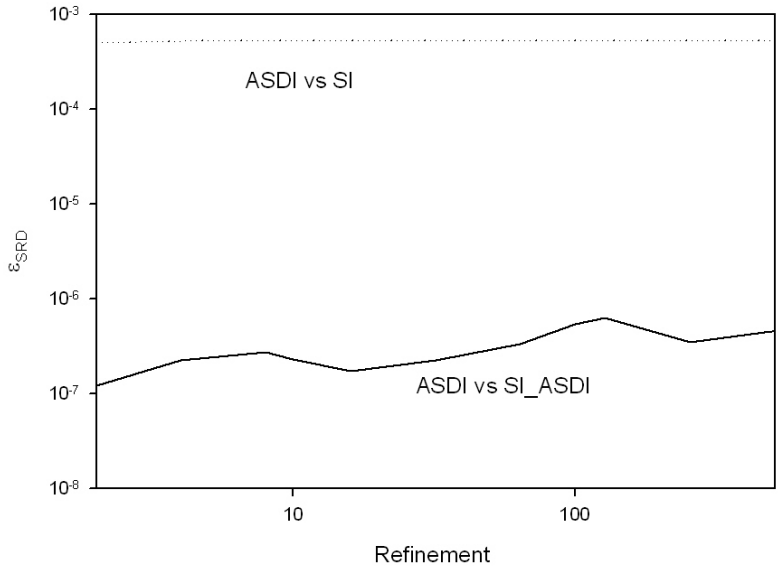

Figure 23: Plot of Symmetric Relative Difference ε_{SRD} between ASDI solution and SI solutions as cell mesh is refined. Angular quadrature is DE-8, scattering ratios are baseline values, convergence tolerance is 10^{-6}.

Effectiveness was next tested. Figure 24 shows that ASDI converges on a solution in less than 8 iterations for a refinement factor of 1 growing slightly as refinement factor is increased then remaining constant for refinement factors above 16. SI requires many more iterations than ASDI and provides unreliable solutions for these refinement factors since this is a diffusive problem.

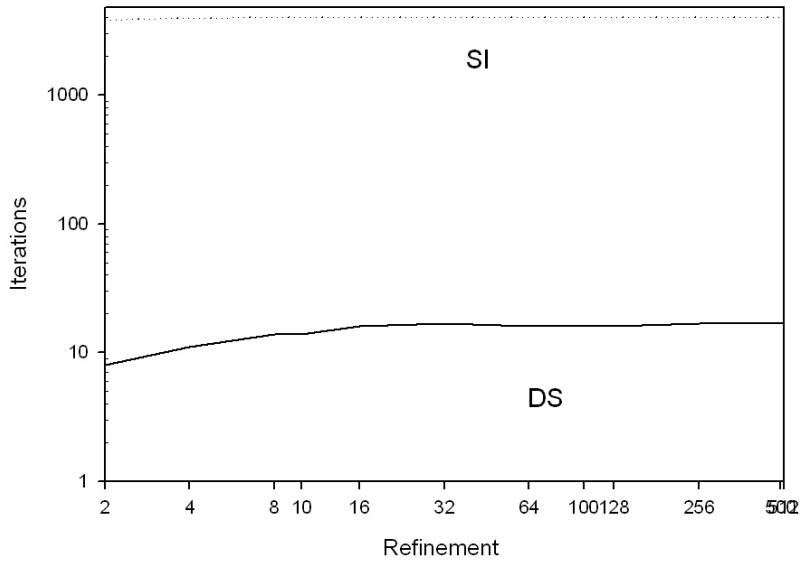

Figure 24 Plot of iteration count as cell mesh is refined. Angular quadrature is DE-8, scattering ratios are baseline values, convergence tolerance is 10^{-6}.

Computational efficiency was next tested. Figure 25 demonstrates that ASDI requires less compute time than SI regardless of mesh size for the baseline scattering ratios selected. However, as spatial mesh is refined the compute time of ASDI is nearly the same as the compute time of SI. The relatively comparable compute times of SI and ASDI do not indicate that SI is just as efficient as ASDI for these fine spatial meshes because SI does not provide reliably accurate answers. ASDI does not require excessive compute time at all refinement factors.

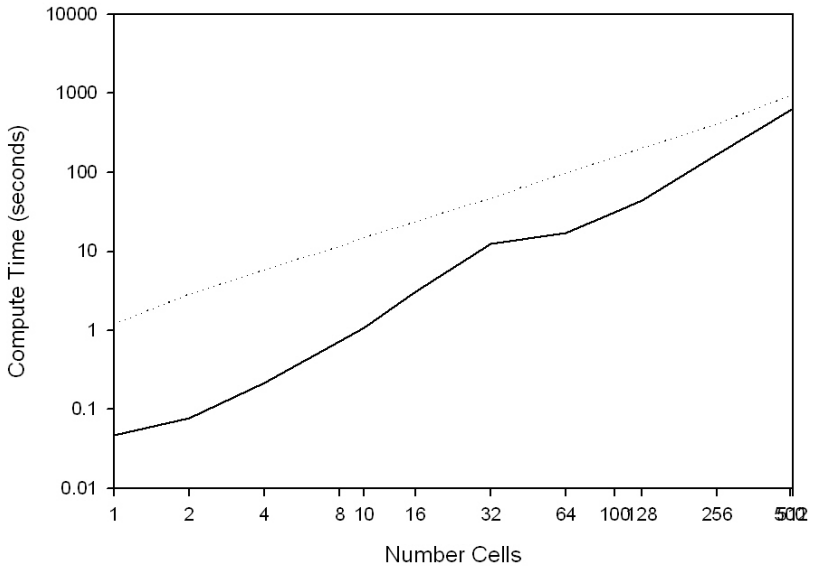

Figure 25: Plot of compute time as cell mesh is refined. Angular quadrature is DE-8, scattering ratios are baseline values, convergence tolerance is 10^{-6}.

Accuracy, effectiveness and computational efficiency were further tested with fixed scattering ratio and refinement factor for varying convergence tolerance and angular refinement. These results are not shown here. As in problem 1 these results indicate that ASDI remains reliably accurate, effective and efficient as these parameters vary.

These experiments demonstrate the strength of the ASDI method for a 2 region periodic material. The experiments demonstrate that ASDI was always reliably accurate and that the parameters with the greatest impact on iteration count and compute time were scattering ratio and refinement factor. The experiments presented kept cross sections constant but varied spatial refinement. In order to fully stress material discontinuity in this periodic material I next examined the impact of varying both scattering ratio and cross section simultaneously in material II. I varied scattering ratio fraction from 0.0 to 1.0 and cross section from $10^{-7}\,\mathrm{cm}^{-1}$ to $10^{+7}\,\mathrm{cm}^{-1}$. I examined the impact of varying these two parameters on accuracy, effectiveness and efficiency at a refinement factor of 1.

A 3D plot of ASDI the symmetric relative difference between ASDI and SI ($\varepsilon_{\mathrm{SRD}}(\mathrm{ASDI,SI\_ASDI})$) and between ASDI and SI given the ASDI solution

($\varepsilon_{\mathrm{SRD}}(\mathrm{ASDI},\mathrm{SI\_ASDI})$)is shown in Figure 26. This plot shows that ASDI is reliably accurate across the wide range of material properties tested

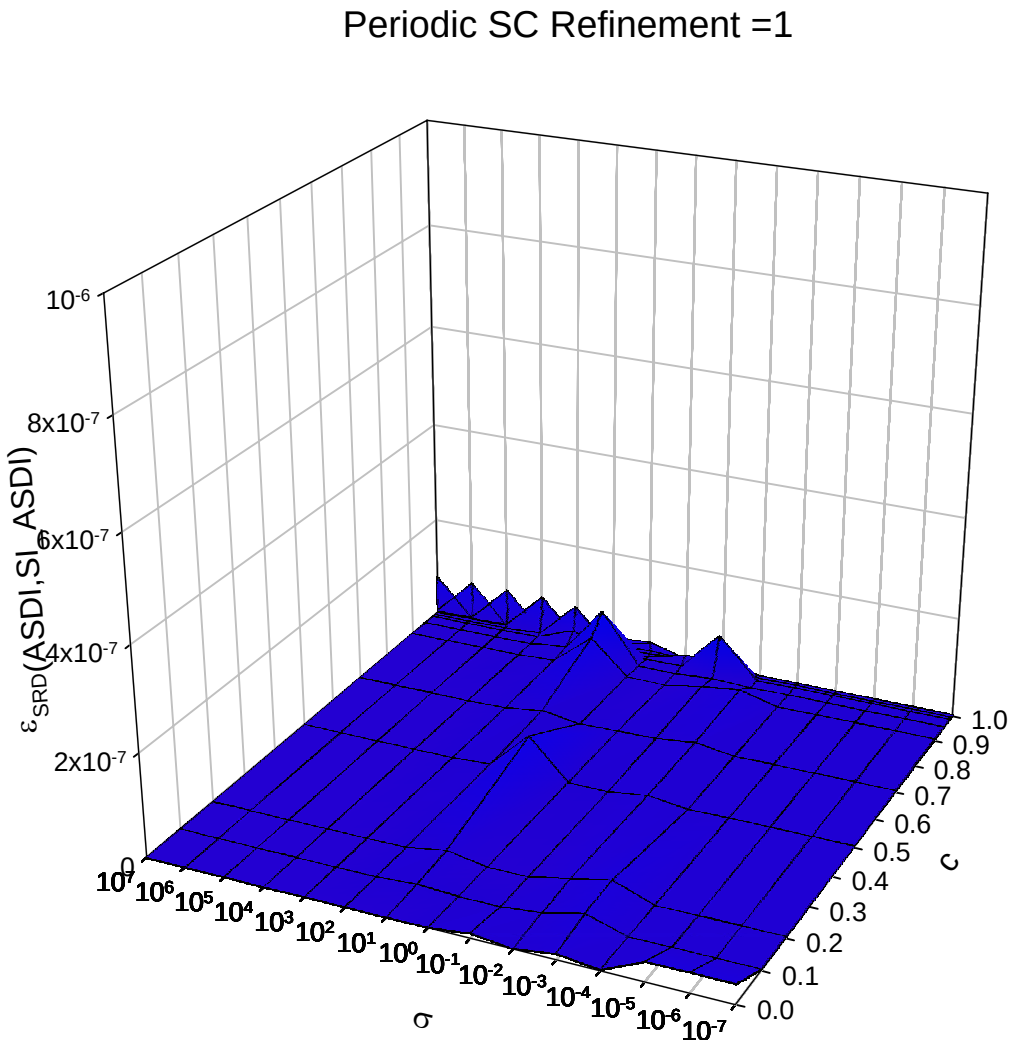

Figure 26: 3D Plot of ASDI symmetric relative difference between ASDI and SI ($\varepsilon_{\mathrm{SRD}}(\mathrm{ASDI,SI\_ASDI})$) and between ASDI and SI given the ASDI solution ($\varepsilon_{\mathrm{SRD}}(\mathrm{ASDI,SI\_ASDI})$) as scattering ratio and cross section vary . Angular quadrature is DE-8, convergence tolerance is 10^{-6}, refinement factor is 1.

A 3D plot of ASDI iteration count versus cross section and scattering ratio is shown in Figure 27.

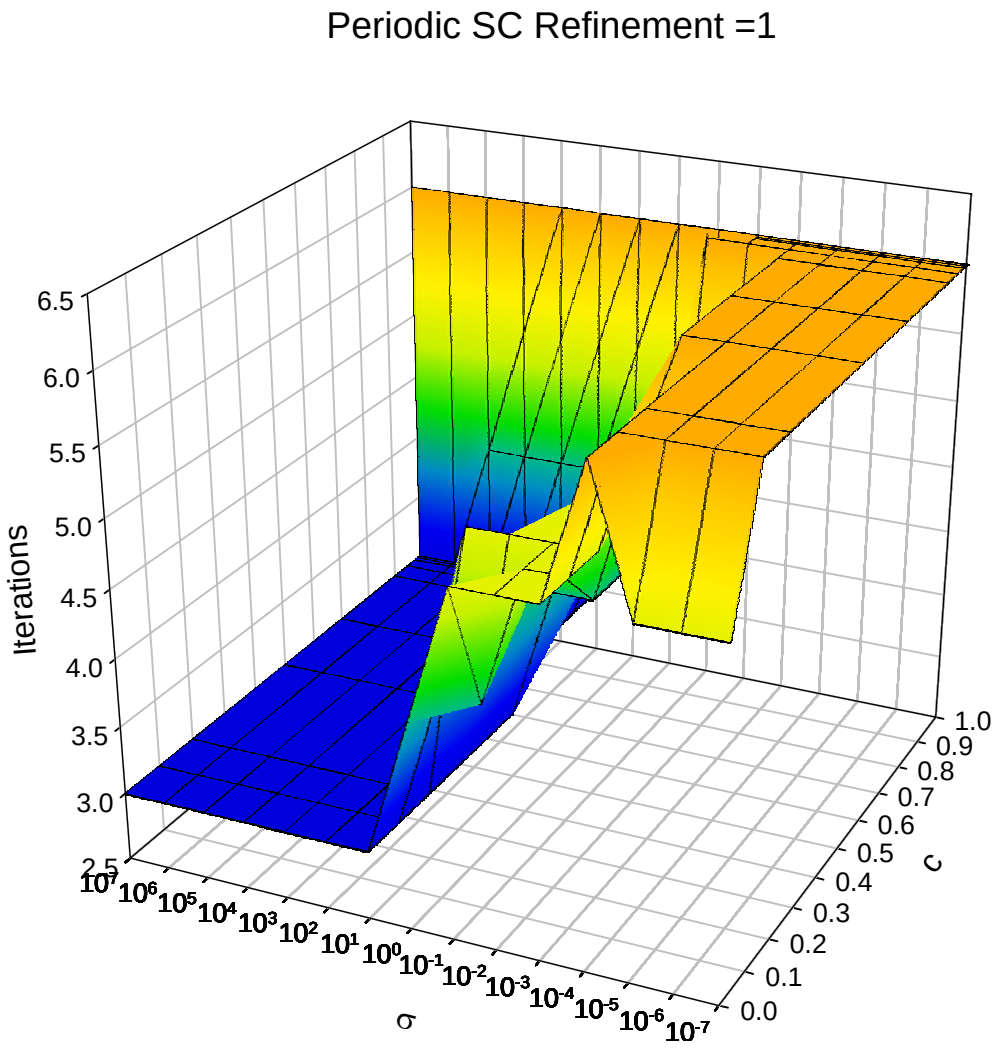

Figure 27: 3D Plot of ASDI iteration count as scattering ratio and cross section vary . Angular quadrature is DE-8, convergence tolerance is 10^{-6}, refinement factor is 1.

This figure demonstrates that ASDI is not sensitive to either scattering ratio or cross section taking at most 7 iterations to converge regardless of the sharpness of material discontinuity. Again, a low iteration count is not useful if computational cost is prohibitive. A comparison of the time required for ASDI and SI to solve the problem is shown in Figure 28. The ratio of the ASDI compute time to SI compute time is shown in the figure, if this ratio is less than 1.0 then ASDI takes less time than SI. This is the case for almost all combinations of scattering ratio and cross section. SI takes less compute time than ASDI when scattering ratios that are not diffusive. Even in these problems where SI is computationally efficient ASDI compute times is of the same order

of magnitude but more importantly provides reliably accurate answers across a broader range of parameters. SI provides unreliable answers because it converges falsely even when material II is a strong absorber. The false convergence of SI occurs because material I is diffusive.

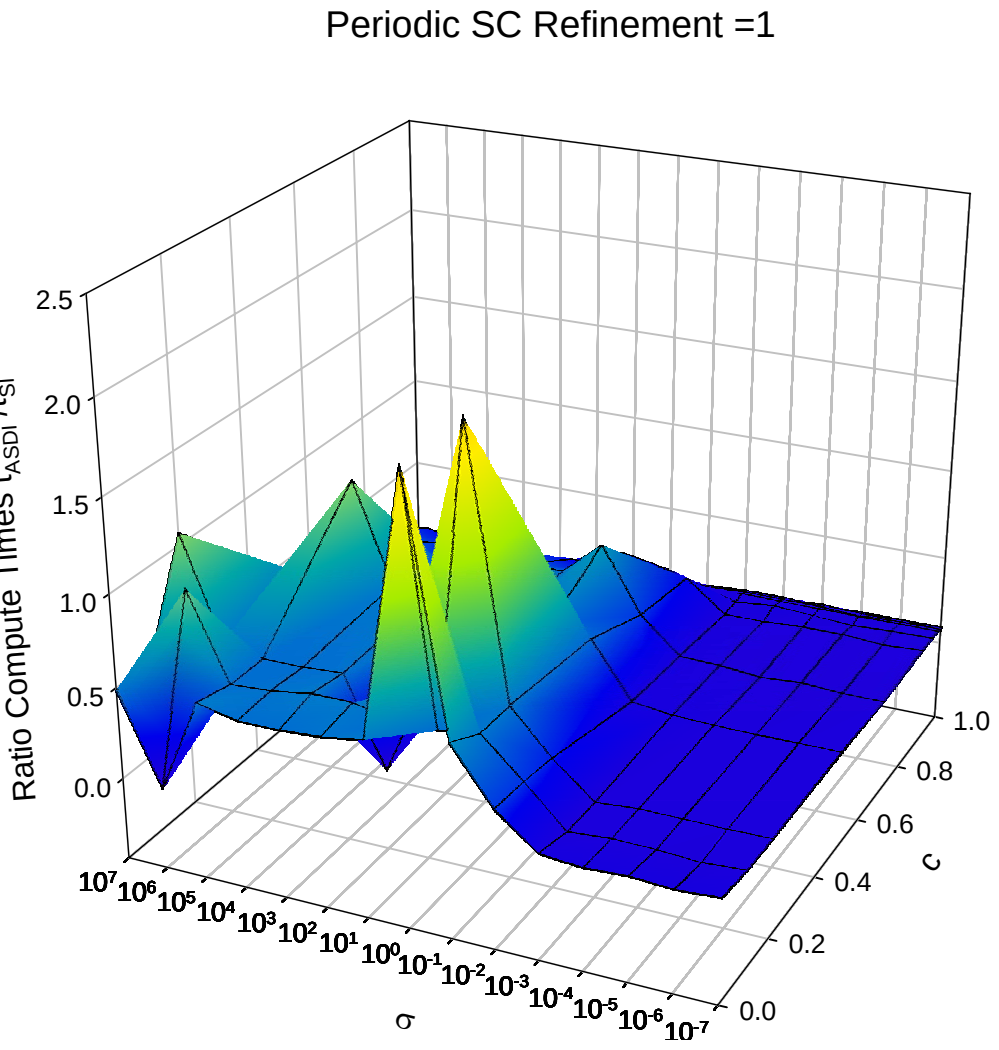

Figure 28: 3D Plot of the ratio ASDI compute time to SI Compute time as scattering ratio and cross section vary . Angular quadrature is DE-8, convergence tolerance is 10^{-6}, refinement factor is 1.

These experiments demonstrate that ASDI is reliably accurate for all the parameters studied and therefore robust. The method dramatically reduces iteration count and required computing time for diffusive problems compared with SI.

IV Solution of the Discrete Ordinates (S_n) Transport Equations with EC

This chapter introduces cell transport coefficients for the EC spatial quadrature. The derivation of this spatial quadrature was done by Mathews, Minor, and Sjoden in 1993. I adopt their notation for limits of integration and leftward or rightward directed fluxes and flux moments. With this notation the cell average source is

$$Q_{n,i} = \int_0^{\Delta x_i} \frac{dx}{\Delta x_i} Q_n(x), \tag{227}$$

$$Q_{n,i} = S_{A_{n,i}} + E_{A_{n,i}}, \tag{228}$$

where Δx_i is the width of a spatial cell whose left edge is $x_{i-\frac{1}{2}}$ and whose right edge is the $x_{i+\frac{1}{2}}$. The average scattered source in cell i is

$$S_{A_{n,i}} = \int_0^{\Delta x_i} \frac{dx}{\Delta x_i} S_n(x). \tag{229}$$

The average intrinsic particle emission in cell i is

$$E_{A_{n,i}} = \int_0^{\Delta x_i} \frac{dx}{\Delta x_i} E_n(x). \tag{230}$$

The SC spatial quadrature assumed that the both source distributions were constant. However, the EC spatial quadrature assumes that the distribution of scattered source is exponential. The distribution of emission source is assumed to be constant for this discussion. An alternative to a constant emission source is to assume it has the same exponential distribution as the scattered particle source

distribution. If this is done the averaging of the emission source is handled in the same way as the scattered source. Extension for an exponentially distributed emission source is obvious.

EC Transport coefficients

The scattered source distribution for EC is exponential

$$\mathrm{S}_{n,i}(x) = a_{n,i}\, e^{-\beta_{\mathrm{n,i}}\frac{x}{\Delta x_i}}. \tag{231}$$

The parameters $a_{n,i}$ and $\beta_{n,i}$ are chosen to match available information about the source, typically its average, equation **(38)** and first spatial moment

$$S_{x_{n,i}} = \int_0^{\Delta x_i} \frac{dx}{\Delta x_i} 3\,\mathrm{P}_1(x)\, S_{n,i}(x), \tag{232}$$

where $\mathrm{P}_1(x)$ is a shifted Legendre polynomial:

$$\mathrm{P}_1(x) = 2\frac{x}{\Delta x_i} - 1, \tag{233}$$

defined in the interval $-\frac{\Delta x_i}{2}$ to $\frac{\Delta x_i}{2}$. In practice $S_{A_{n,i}}, S_{x_{n,i}}$ are not calculated from equations (38) and (232) but are accumulated from angular flux moments

$$S_{A_{n,i}} = \sum_{n'=1}^{N} \sigma_{s_{n',n,i}} \psi_{A_{n',i}} \tag{234}$$

$$S_{x\,n,i} = \sum_{n'=1}^{N} \sigma_{s_{n',n,i}} \psi_{x_{n',i}} \,. \tag{235}$$

EC transport equations for cell edge flux are

$$\psi_{n,i+\frac{1}{2}} = \psi_{n,i-\frac{1}{2}} e^{-\left|\varepsilon_{n,i}\right|} + \frac{a_{n,i}\,\Delta x_i}{|\mu_n|} e^{-\beta_{n,i}}\, \mathcal{M}_o\left(\left|\varepsilon_{n,i}\right| - \beta_{n,i}\right), \qquad \mu_n > 0 \tag{236}$$

$$\psi_{n,i-\frac{1}{2}} = \psi_{n,i+\frac{1}{2}} e^{-\left|\varepsilon_{n,i}\right|} + \frac{a_{n,i}\,\Delta x_i}{|\mu_n|} e^{-\beta_{n,i}}\, \mathcal{M}_o\left(\left|\varepsilon_{n,i}\right| - \beta_{n,i}\right). \qquad \mu_n < 0 \tag{237}$$

See page 31 of the Mathews, Sjoden and Minor work (reference 7) where these equations are clearly derived. Optical path length, $\varepsilon_{n,i}$, was given previously as equation (56). The transport equations for cell average flux are

$$\psi_{A_{n,i}} = \psi_{n,i-\frac{1}{2}}\, \mathcal{M}_o\left(\left|\varepsilon_{n,i}\right|\right) + \frac{a_{n,i}\,\Delta x_i}{|\mu_n|}\, \mathcal{M}_o\left(\left|\varepsilon_{n,i}\right|, \beta_{n,i}\right) \qquad \mu_n > 0 \tag{238}$$

$$\psi_{A_{n,i}} = \psi_{n,i+\frac{1}{2}}\, \mathcal{M}_o\left(\left|\varepsilon_{n,i}\right|\right) + \frac{a_{n,i}\,\Delta x_i}{|\mu_n|}\, \mathcal{M}_o\left(\left|\varepsilon_{n,i}\right|, \beta_{n,i}\right) \qquad \mu_n < 0 \tag{239}$$

The transport equations for cell first spatial flux moments are

$$\begin{aligned} \psi_{x_{n,i}} = {} & 3\psi_{n,i-\frac{1}{2}}\left[\, \mathcal{M}_o\left(\left|\varepsilon_{n,i}\right|\right) - 2\,\mathcal{M}_1\left(\left|\varepsilon_{n,i}\right|\right) \right] \; + \\ & 3\,\frac{a_{n,i}\,\Delta x_i}{|\mu_n|}\left[\, \mathcal{M}_o\left(\left|\varepsilon_{n,i}\right|, \beta_{n,i}\right) - 2\,\mathcal{M}_1\left(\left|\varepsilon_{n,i}\right|, \beta_{n,i}\right) \right], \qquad \mu_n > 0 \end{aligned} \tag{240}$$

$$\begin{aligned} \psi_{x_{n,i}} = {} & 3\psi_{n,i+\frac{1}{2}}\left[\, \mathcal{M}_o\left(\left|\varepsilon_{n,i}\right|\right) - 2\,\mathcal{M}_1\left(\left|\varepsilon_{n,i}\right|\right) \right] \; + \\ & 3\,\frac{a_{n,i}\,\Delta x_i}{|\mu_n|}\left[\, \mathcal{M}_o\left(\left|\varepsilon_{n,i}\right|, \beta_{n,i}\right) - 2\,\mathcal{M}_1\left(\left|\varepsilon_{n,i}\right|, \beta_{n,i}\right) \right]. \qquad \mu_n < 0 \end{aligned} \tag{241}$$

Examination of these equations reveals they are in the form of equations (42) through (45). The transport coefficients are obvious. The first transport coefficient from the first term of equation (236) or (237) relates outgoing flux to incoming flux. It is

$$K_{OI\,n,i} = e^{-\varepsilon_{n,i}} \,. \tag{242}$$

The second transport coefficient from the second term of equation (236) or (237) describes the contribution of within cell scattering to the cell outgoing flux. It is

$$K_{OS\,n,i} = \frac{\Delta x_i}{|\mu_n|} e^{-|\beta_{n,i}|}\, \mathcal{M}_o\left(|\varepsilon_{n,i}| - \beta_{n,i}\right). \tag{243}$$

The third transport coefficient from the first term of equations (238) or (239) describes contribution of flux entering a cell edge to cell average flux. It is

$$K_{AI\,n,i} = \mathcal{M}_o\left(|\varepsilon_{n,i}|\right). \tag{244}$$

The fourth transport coefficient from the second term of equations (238) or (239) describes contribution of cell scattering to cell average flux. It is

$$K_{AS\,n,i} = \frac{\Delta x_i}{|\mu_n|} e^{-|\beta_{n,i}|}\, \mathcal{M}_o\left(|\varepsilon_{n,i}|, \beta_{n,i}\right). \tag{245}$$

The fifth and sixth transport coefficients depend on whether a particle enters a cell right or left edge. These coefficients capture flux spatial first moment information the negative sign on equation (241) reflect that a flux gradient appears different to particles streaming in ordinates that have equal direction cosines but in opposing directions. The fifth transport coefficient, from the first term of equations (240) or (241), describes contribution of flux entering an edge to cell first moment flux. It is

$$K_{X_I\,n,i} = 3\left[\mathcal{M}_o\left(|\varepsilon_{n,i}|\right) - 2\,\mathcal{M}_1\left(|\varepsilon_{n,i}|\right)\right] \quad , \tag{246}$$

The sixth transport coefficient, from the second term of equations (240) or (241), describes contribution of cell scattering to cell first moment flux. It is

$$K_{X_S\,n,i} = 3\,\frac{\Delta x_i}{|\mu_n|}\left[\mathcal{M}_o\left(|\varepsilon_{n,i}|, \beta_{n,i}\right) - 2\,\mathcal{M}_1\left(|\varepsilon_{n,i}|, \beta_{n,i}\right)\right] \quad , \tag{247}$$

Comparison of equations (242) through equation (245) shows that the difference between SC transport coefficients and EC transport coefficients is that $\beta_{n,i} = 0$ for SC because its spatial first moment is defined to be zero.

The cell EC transport equations may be written in vector notation as

$$\vec{\psi}_{out_i} = \mathbf{K}_{OI_i} \vec{\psi}_{in_i} + \mathbf{K}_{OS_i}\left(\vec{\beta}_i\right) \vec{S}_{A_i} + \mathbf{K}_{OE_i} \vec{E}_{A_i}\,, \tag{248}$$

$$\vec{\psi}_{A_i} = \mathbf{K}_{AI_i} \vec{\psi}_{in_i} + \mathbf{K}_{AS_i}\left(\vec{\beta}_i\right) \vec{S}_{A_i} + \mathbf{K}_{AE_i} \vec{E}_{A_i}\,, \tag{249}$$

$$\vec{\psi}_{x_i} = \mathbf{K}_{\mathbf{x}I_i} \vec{\psi}_{in_i} + \mathbf{K}_{\mathbf{x}S_i} \vec{S}_{A_i}\,, \tag{250}$$

$$\vec{S}_{A_i} = \mathbf{\Sigma}_S \vec{\psi}_{Ai}\,, \tag{251}$$

$$\vec{S}_{x_i} = \mathbf{\Sigma}_S \vec{\psi}_{x_i}\,, \tag{252}$$

where

$$\vec{\beta}_i = \begin{bmatrix} \beta_{1,i} \\ \vdots \\ \beta_{N_R,i} \\ \beta_{N_R+1,i} \\ \vdots \\ \beta_{N,i} \end{bmatrix}. \tag{253}$$

where each of the coefficient matrices is dependent on the associated element of $\vec{\beta}_i$. For the same reason that assembly of a fully spatially and directionally coupled system of equations was impractical to solve for SC it is even more impractical for EC. This is because of the additional first moment equations (250) and the inherent nonlinearity in $\vec{\beta}_i$. (7:29,30).
However, if the incoming edge flux is known $\vec{\beta}_i$ can be found by iteration. The logic of this iteration is shown in Algorithm 5.

Initialize

estimate edge flux $\vec{\psi}_{in}$

calculate cell coupling coefficients for $\mathbf{K}\left(\vec{\beta}^{(\ell+1)}\right)$

Do

calculate $\vec{\beta}^{(\ell)}\left(\vec{S}_A^{(\ell)}, \vec{S}_x^{(\ell)}\right)$

calculate $\mathbf{K}\left(\vec{\beta}^{(\ell+1)}\right)$

calculate $\vec{\psi}_A^{(\ell+1)}\left(\vec{\psi}_{in}\right)$

calculate $\vec{\psi}_x^{(\ell+1)}\left(\vec{\psi}_{in}\right)$

calculate $\vec{S}_A^{(\ell+1)}$

calculate $\vec{S}_x^{(\ell+1)}$

calculate new $\vec{\beta}^{(\ell+1)}\left(\vec{S}_{A_i}, \vec{S}_{x_i}\right)$

End do when $\varepsilon_{SRD}\left(\vec{\beta}_i^{(\ell+1)}, \vec{\beta}_i^{(\ell)}\right)$ *converged*

Equations (89) through (252) are used in the beta iteration algorithm.

Once $\vec{\beta_i}$ is known, edge flux is also found by iteration. Outgoing edge flux is calculated from equation (89) and $\vec{\psi}_{A_i}$ is calculated from (90). This is done for each cell and then boundary conditions are applied. The outgoing edge flux calculated for a cell is used as the incoming edge flux for an adjacent cell. The logic of this iteration is shown in Algorithm 6.

initialize flux

$$\vec{\beta} = \vec{\beta}_{converged}$$

$$\vec{\psi}_{in}^{(0)} = \vec{\psi}_{in}^{(b)}$$

Do all cells

$$calculate\ \vec{\psi}_{out}^{(\ell)}\left(\vec{\psi}_{in}^{(\ell)}, \mathbf{K}\left(\vec{\beta}\right)\right)\ for\ all\ cells$$

apply boundary conditions

$$update\ \vec{\psi}_{in}^{(\ell+1)}\ from\ adjacent\ cell\ outflow$$

$$End\ do\ when\ \varepsilon_{SRD}\left(\vec{\psi}_{in}^{(\ell+1)}, \vec{\psi}_{in}^{(\ell)}\right)\ for\ current\ \vec{\beta}$$

3. A

Analysis of Algorithm 5 and Algorithm 6 reveals that these two algorithms are linked through $\vec{\beta}_i$ and edge flux $\vec{\psi}_{in}$. Changing $\vec{\beta}$ leads to new transport coefficients which lead to new flux $\vec{\psi}_{in_i}$. Updated $\vec{\psi}_{in_i}$ leads to new estimates for $\vec{\beta}$. The interdependence of these two algorithms suggests the following iteration scheme to couple outgoing edge flux iteration with beta iteration.

Initialize

estimate initial flux $\bar{\psi}_{in}^{(0)}$

estimate $\vec{\beta}^{(0)}$

calculate cell coupling coefficients for $\mathbf{K}\left(\vec{\beta}^{(0)}\right)$

Do

Do

calculate $\vec{\beta}^{(\ell)}\left(\bar{S}_A^{(\ell)}, \bar{S}_x^{(\ell)}\right)$

calculate $\mathbf{K}\left(\vec{\beta}^{(\ell+1)}\right)$

calculate $\bar{\psi}_A^{(\ell+1)}\left(\bar{\psi}_{in}^{(b)}\right)$

calculate $\bar{\psi}_x^{(\ell+1)}\left(\bar{\psi}_{in}^{(b)}\right)$

calculate $\bar{S}_A^{(\ell+1)}$

calculate $\bar{S}_x^{(\ell+1)}$

calculate new $\vec{\beta}^{(\ell+1)}\left(\bar{S}_{A_i}, \bar{S}_{x_i}\right)$

2.

initialize flux $\bar{\psi}_{in}^{(0)} = \bar{\psi}_{in}^{(b)}$

Do all cells

calculate $\bar{\psi}_{out}^{(\ell)}\left(\bar{\psi}_{in}^{(\ell)}, \mathbf{K}\left(\vec{\beta}\right)\right)$ *for all cells*

apply boundary conditions

update $\bar{\psi}_{in}^{(\ell+1)}$ *from adjacent cell outflow*

End do when $\varepsilon_{SRD}\left(\bar{\psi}_{in}^{(\ell+1)}, \bar{\psi}_{in}^{(\ell)}\right)$ *for current* $\vec{\beta}$

Algorithm 6 solves for refined edge flux. It accounts for all within cell scattering through inversion of the scattering source as was done for SC. The

beta iteration loop defines source distribution and facilitates calculation of cell transport coefficients. The coupled beta edge flux iteration loop solves for within cell scattering and accounts source distribution, it does not explicitly couple cells across the spatial domain. However, if beta is held fixed at a current iteration estimate edge flux can be calculated from equations (89) and (90) just as was done for SC. These equations can be collapsed with flux weights, as was done for SC, using equations (197) through (202). The spatially coupled transport equations are then readily solved as in chapter 2 using equation (172). This suggests the following iteration scheme, Algorithm 8 that accounts for refined angle within cell transport, the exponential source distribution, and particle transport across cells in the spatial domain.

! obtain an initial guess for $\vec{\psi}_{in_i}$

! obtain an initial guess for $\vec{\beta}_i$

! calculate cell coupling coefficients for $K(\beta)$

Do

estimate initial flux $\bar{\psi}_{in}^{(0)}$

estimate $\vec{\beta}^{(0)}$

calculate cell coupling coefficients for

$$\mathbf{K}\left(\vec{\beta}^{(0)}\right)$$

Do

Do

calculate $\vec{\beta}^{(\ell)}\left(\bar{S}_A^{(\ell)}, \bar{S}_x^{(\ell)}\right)$

calculate $\mathbf{K}\left(\vec{\beta}^{(\ell+1)}\right)$

calculate $\bar{\psi}_A^{(\ell+1)}\left(\bar{\psi}_{in}^{(b)}\right)$

calculate $\bar{\psi}_x^{(\ell+1)}\left(\bar{\psi}_{in}^{(b)}\right)$

calculate $\bar{S}_A^{(\ell+1)}$

calculate $\bar{S}_x^{(\ell+1)}$

calculate new $\vec{\beta}^{(\ell+1)}\left(\bar{S}_{A_i}, \bar{S}_{x_i}\right)$

End do $\varepsilon_{SRD}\left(\vec{\beta}_i^{(\ell+1)}, \vec{\beta}_i^{(\ell)}\right)$ *converged*

use refined angular edge flux to collapse transport coefficients

calculate $\bar{\bar{\psi}}_{in_i}$

apportion coarse $\bar{\bar{\psi}}_{in_i}$ to obtain new fine $\vec{\bar{\psi}}_{in_i}$

End Do when $\varepsilon_{SRD}\left(\bar{\psi}_{in}^{(b)}, \vec{\bar{\psi}}_{in}\right)$ less than convergence tolerance

1.

lgorithm 8: EGAngular and Spatially Coupled Flux Iteration

Algorithm 8 couples the angular and spatially explicit edge flux solutions in a scheme that accounts for infinite scatters from cell to cell and within a cell

as was done for SC but adds the inner loop to solve for $\overline{\beta}_i$ then iterates the edge flux and beta iteration schemes to get a best value for edge flux distribution. This estimate is used to update collapsed transport coefficients which are used to calculate spatially coupled coarse edge flux and to apportion this coarse edge flux back into fine flux components. The apportioned edge flux updates the cell incoming edge flux and the iteration scheme proceeds again. The iteration scheme of Algorithm 8 effectively accounts for infinite particle flights in a single iteration. Results of this algorithm implemented as Fortran 95 code are discussed in the next chapter.

V. EC Experimental Results

After showing that the ASDI method met my evaluation criteria: robust (reliably accurate for the problems intended), efficient (requires few iterations to converge), effective (converges rapidly as measured by compute time) with SC, I implemented the method using EC. I used the same suite of experiments to test the methods accuracy, effectiveness and computationally efficiency for the EC experiments as I did for SC.

To review, the first experiment had an optically thick homogeneous material. I varied this homogeneous material from absorber (low scattering ratio) to scatterer (scattering ratio nearly one) in order to test ASDI against SI for problems which converged readily and one for problems which converged slowly.

The second experiment investigated the effect of periodic material discontinuity on the comparative performance of ASDI by using two materials of the same dimension. There was an emission source in one material and no source in the other material. Both materials were 1 MFP wide. The emitter had a scattering ratio of one. The non-emitter's scattering ratio varied from 0.0 to 1.0 as in the homogeneous material. This two material pattern was repeated 10 times creating a periodic discontinuity in the materials.

I again investigated the effect of scattering ratio, spatial refinement, angular refinement and convergence criterion on robustness, effectiveness, and efficiency for both the homogeneous and periodic problems. The parameters I varied in turn were: scattering ratio, spatial refinement, angular refinement and convergence tolerance. I examined these parameters for a homogeneous then a two material problem. Further, I evaluated ASDI with EC over a complete range of scattering ratios and cross sections, just as was done for ASDI with SC and displayed in figures 26, 27, and 28.

As I did with SC, I tested ASDI's accuracy by checking its solution against a benchmark to ensure it met the convergence tolerance required. The benchmarks were the same as those used for SC.

Problem 1 Optically Thick Homogeneous Material

The first test problem studied is a 100 cm thick homogeneous slab with a vacuum boundary on the right, a symmetry boundary on the left, a uniform isotropic source, and a total cross section of $1.0\,\mathrm{cm}^{-1}$. Figure 4, although shown in chapter 3 is redisplayed in this chapter for the reader's convenience.

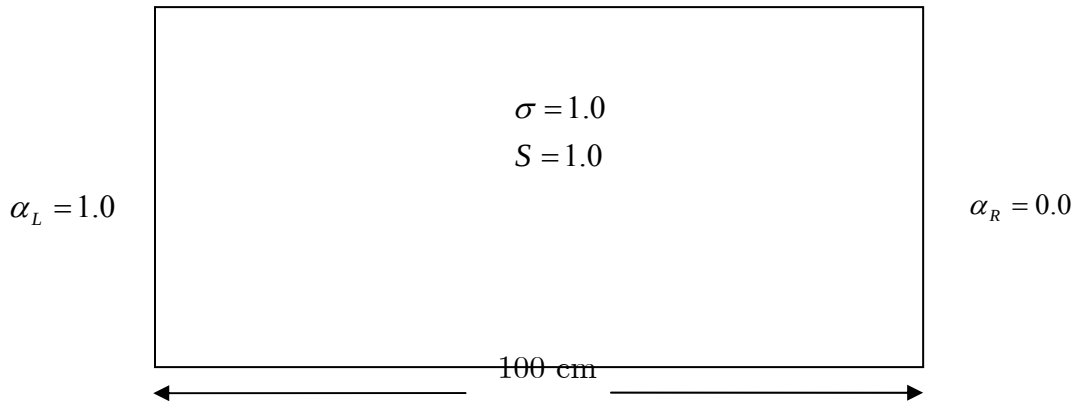

Figure 4 Problem 1

The first experiment tested the EC ASDI solution robustness as scattering ratio varied. Figure 29 displays two plots. These are the symmetric relative difference versus scattering ratio of the ASDI solution and the SI solution (ASDI_SI) and of the ASDI solution and the SI solution after being given the ASDI solution (ASDI_SI-ASDI). The convergence tolerance chosen was 10^{-6} for both SI and ASDI. The SI Solution after having been given the ASDI solution was allowed to iterate the same number of times that it took to arrive at its converged solution without the ASDI start point. For this problem this is between 30 and 500 iterations. The plot shows that the ASDI solution never deviates from this solution by more than the convergence tolerance required. This demonstrates ASDI's reliable accuracy at all scattering ratios. At a scattering of 0.6 and above the SI solution differs by more than the chosen convergence tolerance demonstrating SI's unreliable solutions. This difference increases as the scattering ratio increases. These plots show that SI produces unreliable answers at scattering ratios as low as 0.6 but ASDI provides reliably accurate answers validated by SI's fixed point

recognition. In figure 6 $\varepsilon_{SRD}(ASDI, SI\_ASDI)$ increases from a low value of 10^{-6} and a high value of $5.0 * 10^{-6}$. This range of values is within the required convergence tolerance.

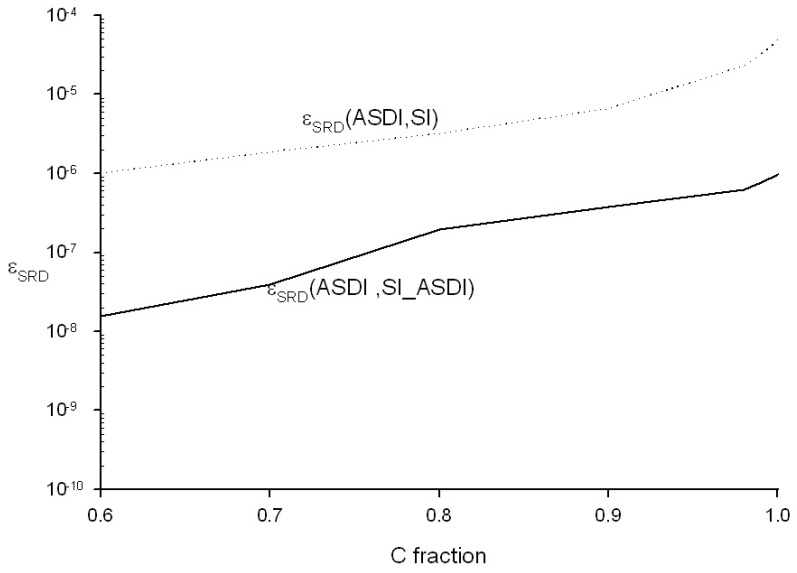

Figure 29: Symmetric Relative Difference ε_{SRD} between the ASDI solution and the SI solution as scattering ratio varies. Angular quadrature is DE-8, refinement is 50 ($\sigma\Delta x = 2\,\mathrm{MFPs}$), convergence tolerance is 10^{-6}.

Figure 30 shows iteration count versus scattering ratio (c) with an angular refinement of 8, a mesh width of 2 MFPs and a convergence tolerance of10^{-6}. As in SC, iteration count increases with scattering ratio, climbing steeply as c approaches unity. This again demonstrates the classic weakness of SI for problems with little or no absorption. With exponential characteristic spatial quadrature each of these iterations requires the non-linear root finding of the source distribution parameter ($\beta_{n,i}$) for every direction in every cell. This root finding can be computationally expensive. The ASDI solution converges in six or less iterations regardless of scattering ratio, demonstrating its effectiveness even for problems with little or no absorption.

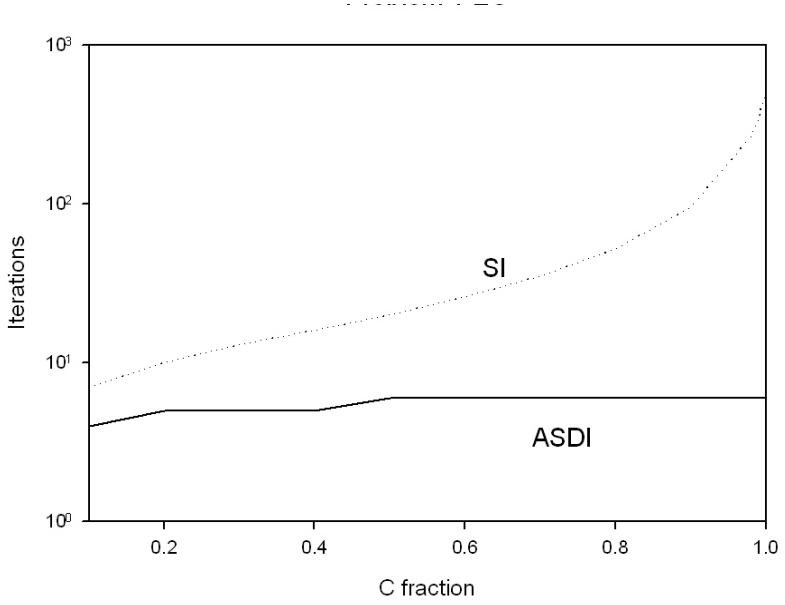

Figure 30 Plot of iteration count versus scattering ratio. Angular quadrature is DE-8, refinement is 50 ($\Delta x = 2\,MFPs$), convergence tolerance is 10^{-6}.

As pointed out previously the low iteration count of the ASDI method with EC displayed in Figure 30 is not a practical improvement over SI unless computational cost is also reduced. Figure 31 displays compute time versus scattering ratio. The amount of compute time needed by the ASDI method is less than 0.3 seconds regardless of the scattering ratio. Even when SI converges more rapidly than ASDI and provides reliably accurate solutions, i.e. at scattering ratios below 0.6, ASDI compute time is the same order of magnitude as SI. The plot confirms that the beta feedback mechanisms of the ASDI method with EC do not converge slowly as the scattering ratio goes to one. This demonstrates that the method does not require excessive compute time with the EC spatial quadrature at least for the homogeneous material.

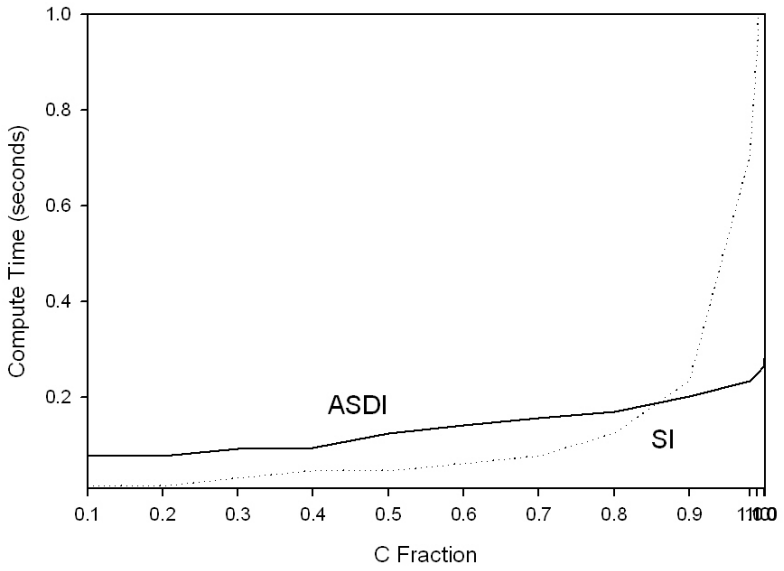

Figure 31 Plot of compute time (seconds) versus scattering ratio. Angular quadrature is DE-8, refinement is 50 ($\sigma\Delta x = 2\,MFPs$), convergence tolerance is 10^{-6}.

The results shown in Figure 30 were obtained with a fixed refinement of 50 mesh cells ($\Delta x = 2.0\,\text{cm}$), convergence tolerance fixed at 10^{-6}, and an angular quadrature fixed at $n = 8$. Spatial refinement, angular refinement, and convergence tolerance are also parameters that are expected to have an impact on robustness, effectiveness, and efficiency of the ASDI method used with the EC spatial quadrature. The next series of plots investigates the effect changing these parameters have on ASDI performance with the EC spatial quadrature. These three parameters were studied with a scattering ratio of 0.98 making the homogeneous material a good scatterer.

Figure 32 shows the relative difference between SI, ASDI and an estimated best solution which is SI after being given the ASDI solution and allowed to iterate enough times to confirm a fixed point. The difference between the ASDI solution and the SI-ASDI solution is less than the convergence tolerance for all refinements whereas the difference between SI and the SI-ASDI answers is greater than the convergence tolerance. This is because SI converges falsely in this optically thick problem with little or no absorption.

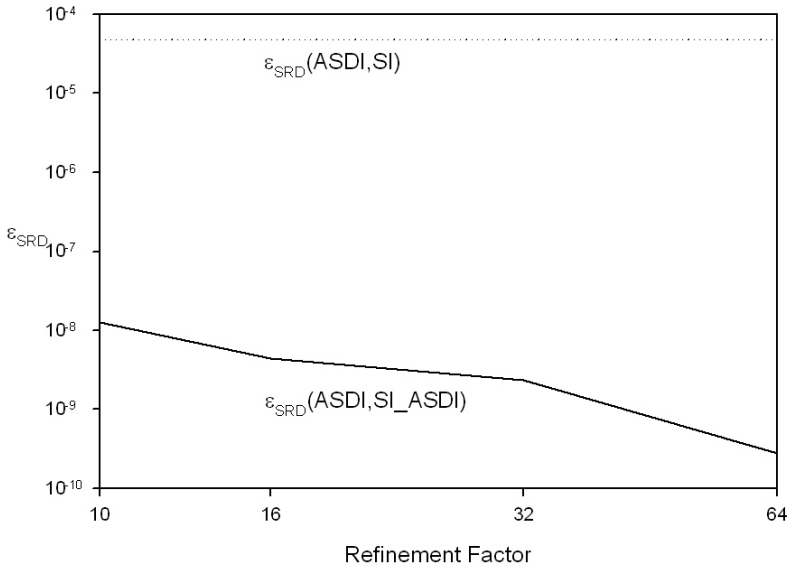

Figure 32 Plot of Symmetric Relative Difference ε_{SRD} between ASDI solution and SI solutions for as cell mesh is refined. Angular quadrature is DE-8, scattering ratio is 1.0, convergence tolerance is 10^{-6}.

SI recognition of the ASDI solution as a fixed point for all spatial refinements provides convincing evidence of the accuracy of its solution. I was able to further test this accuracy because an analytic solution was available for problem 1. I computed and compared the ASDI convergence rate with the known convergence rate of EC. This was done for a DE-4 angular quadrature and a scattering ratio of 1.0 with spatial refinement varying from 10 (cell width=10 cm) through 1000 (cell width = $1.25\text{x}10^{-2}$ cm). I did not expect the ASDI solutions be the same as the analytic solution for coarse spatial meshes because the spatial quadrature is a numerical approximation. However, because EC is known to be fourth order convergent in space, the method can be checked against the analytic solution to determine if the order of spatial convergence is four. Figure 33 shows symmetric relative difference (ε_{SRD}) between the ASDI solution and an exact solution plotted against the spatial mesh refinement factor (R_F) for a scattering ratio of 1.0. ε_{SRD} appears as a straight line on both plots whose slope is 3.86. A line with a slope of four, the convergence order of EC, has been overlaid on the data plot. This

agreement of ASDI's convergence rate with the known EC convergence rate for a scattering ratio of 1.0 combined with SI recognition of ASDI solutions as fixed points demonstrate the method's robustness. The preservation of EC fourth order convergence with spatial refinement provides strong evidence that the ASDI method is not changing the spatial convergence properties of the EC spatial quadrature.

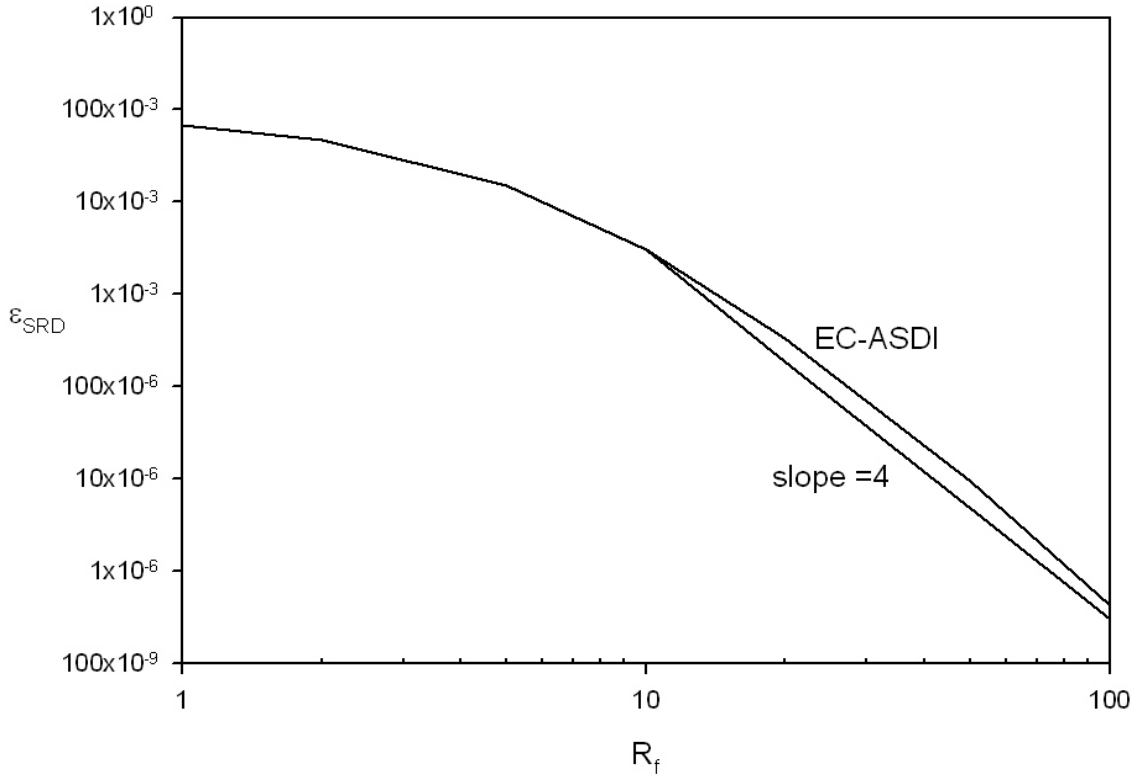

Figure 33: Plot of Symmetric Relative Difference ε_{SRD} between the ASDI solution and an analytic solution as cell mesh is refined between 10 MFPs and 0.1 MFPs. Angular quadrature is DE-8, scattering ratio is 1.0, convergence tolerance is 10^{-6}.

Figure 34 shows the iteration count of the ASDI and SI methods as the mesh is refined. SI iteration remains flat, at 500 iterations, ASDI iteration count is seven or less iterations through mesh refinements of 64. This indicates that the number of iterations required for convergence is not dependent on the mesh refinement for ASDI even when applied to the non-linear EC spatial quadrature.

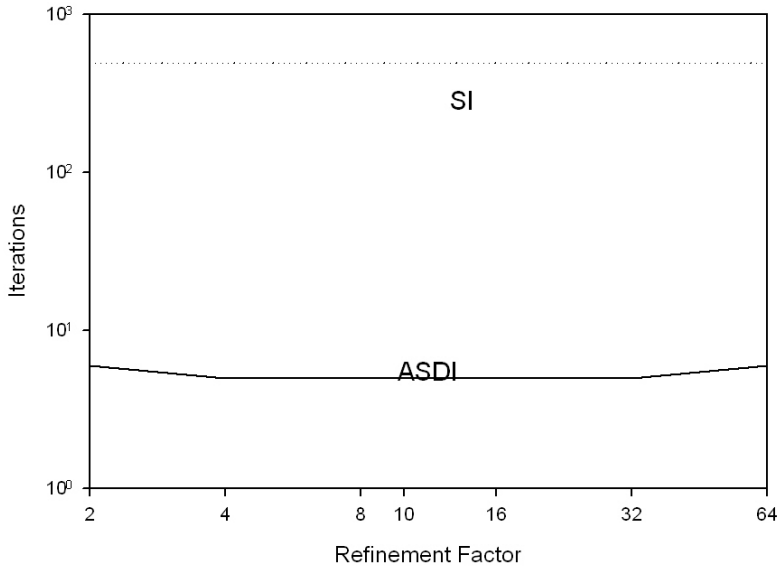

Figure 34 Plot of iteration count as cell mesh is refined. Angular quadrature is DE-8, scattering ratio is 1.0, convergence tolerance is 10^{-6}.

Figure 35 shows the compute times required for the SI and ASDI solutions as the spatial mesh is refined. The spatial refinement increases compute time for both methods. ASDI requires less compute time than SI through a refinement of 32. Although the ASDI method requires more compute time than SI for refinements above 32. This behavior was also observed for ASDI applied to SC in figure 12. The plots indicate that for a fine enough mesh source iteration will converge faster than ASDI. However, SI will not converge to reliable and accurate solutions. The additional time used to compute ASDI approximations results accurate solutions. The plot indicates that ASDI will not require disproportionately more time than SI for refined spatial meshes and will converge to the correct solution. The results observed for EC are similar to those obtained for SC indicating the beta subroutine is working as intended.

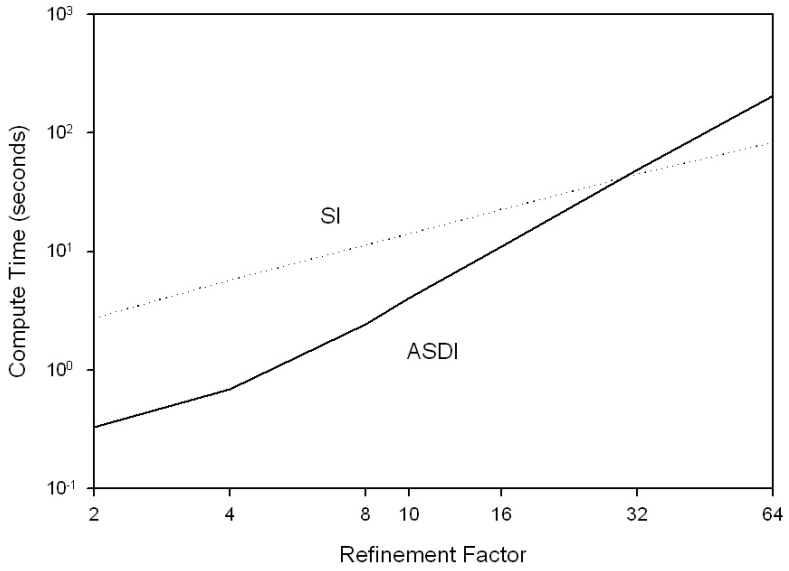

Figure 35 Plot of compute time required for the ASDI and SI solutions as cell mesh is refined. Angular quadrature is DE-8, scattering ratio is 1.0, convergence tolerance is 10^{-6}.

The convergence tolerance used to test previous problems was 10^{-6} on angular flux. This is a fairly tight convergence tolerance and it is suitable for most engineering applications. However, some applications may require tighter tolerances. The effect of tightening convergence tolerance from $10^{-6}$to 10^{-11} on symmetric relative difference, iteration count, and compute time is shown next. Figure 36 shows that the accuracy of the converged SI solution does not meet the accuracy required by the specified convergence tolerance regardless of how tight that tolerance is, whereas the ASDI method continues to provide reliably accurate solutions for any tolerance without round off error or instability. Examination of Figure 36 and Figure 37 reveals that this accuracy is achieved with modest increase in iterations required and compute time for the ASDI method applied to EC. These results are similar to those obtained for SC and displayed in Figures 13, 14, and 15.

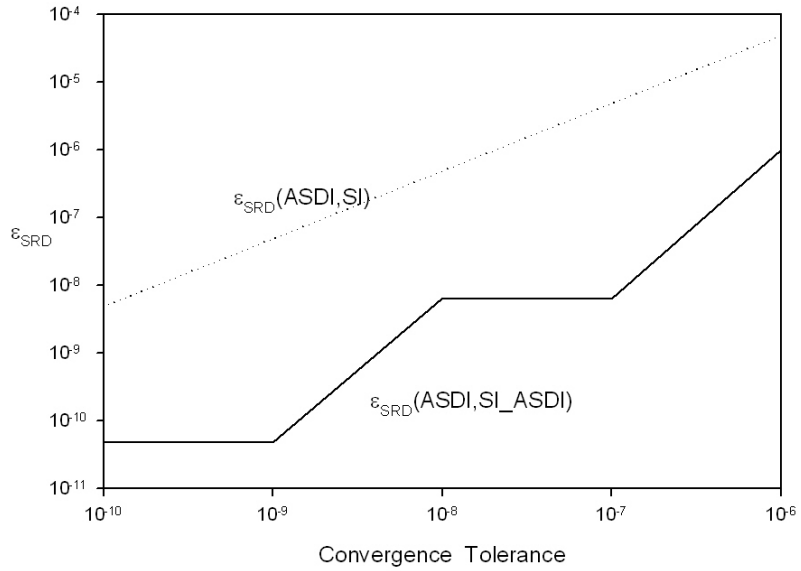

Figure 36 Plot of symmetric relative difference versus convergence tolerance. Angular quadrature is DE-8, scattering ratio is 1.0, cell size is 2 MFPs.

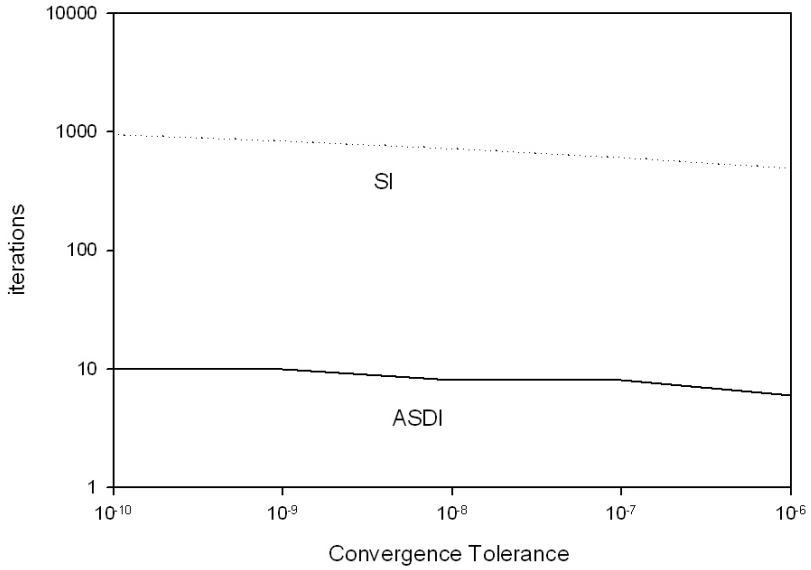

Figure 37 Plot of iterations versus convergence tolerance for ASDI and SI. Angular quadrature is DE-8, scattering ratio is 1.0, cell size is 2 MFPs.

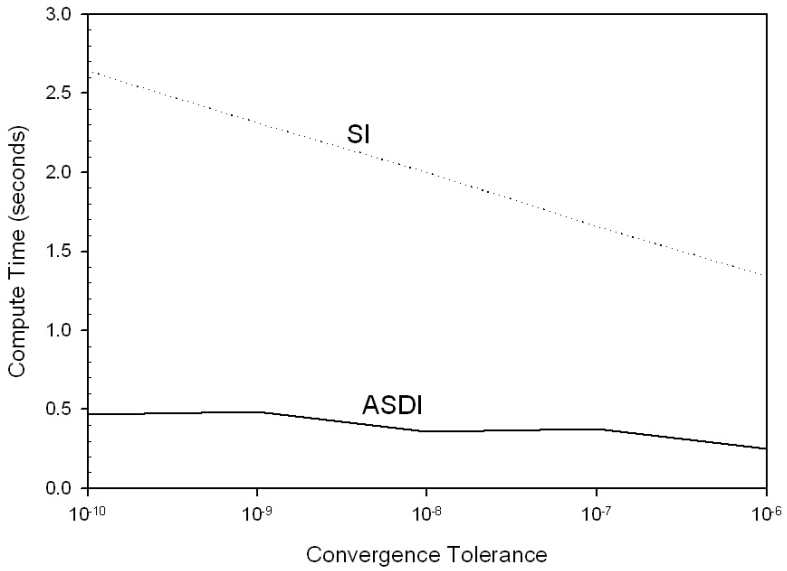

Figure 38 Plot of compute time versus convergence tolerance for ASDI and SI. Angular quadrature is DE-8, scattering ratio is 1.0, cell size is 2 MFPs.

The effect of increasing angular refinement for ASDI applied to EC is shown in Figure 39 through Figure 41. These plots demonstrate that ASDI continues to provide reliably accurate solutions without significantly increasing iteration count and with practical compute times as the number of ordinates in the angular quadrature is increased. SI, as expected, remains inaccurate and increases computational cost as the angular quadrature is refined. As with ASDI applied to SC, ASDI applied to EC converges with the least iteration and most rapid compute times when the angular quadrature has only two directions. ASDI achieves a quick solution for this coarse angular quadrature because the global spatial routine solves the same problem on the first iteration as the fine angle routine. After the first iteration both edge flux and beta are nearly correct and converge rapidly with successive iteration. Unfortunately such a

coarse angular quadrature is not likely to meet most engineering needs. Figure 39 and Figure 40 display the same convergence reliability characteristics and iteration count versus number of directions for EC as was observed with SC in Figure 16 and Figure 17. This is encouraging because the increased angular refinement requires increasing the number of calls to the beta root finding algorithm. The increased number of beta root finding problems does not affect reliability or significantly increase compute times. However, comparison of Figure 41, which shows ASDI-EC compute time versus angular refinement, and Figure 18, which shows ASDI-SC, compute time versus angular refinement, demonstrates that compute time increases more steeply for ASDI-EC than it does for ASDI-SC. The steeper increase in compute time for EC occurs because beta must be found for every direction is every cell..

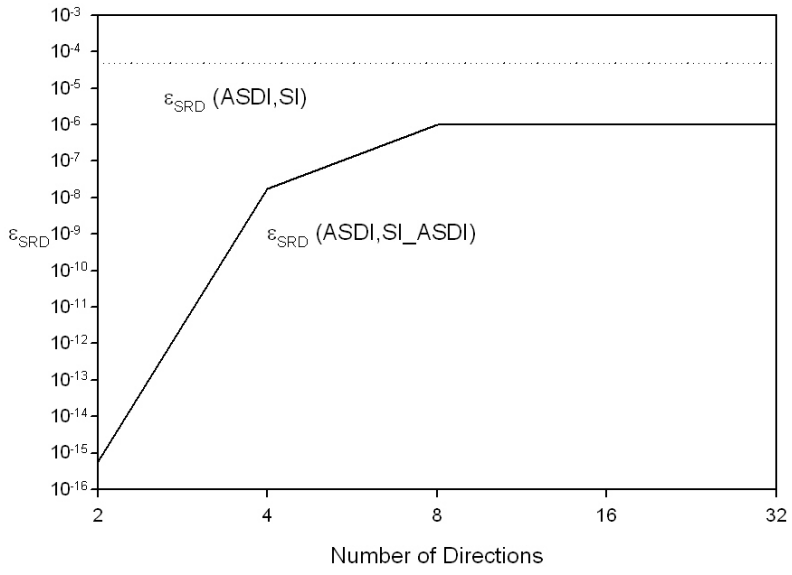

Figure 39 Plot of symmetric relative difference versus angular quadrature. Convergence tolerance is 10^{-6} scattering ratio is 1.0, cell size is 2 MFPs.

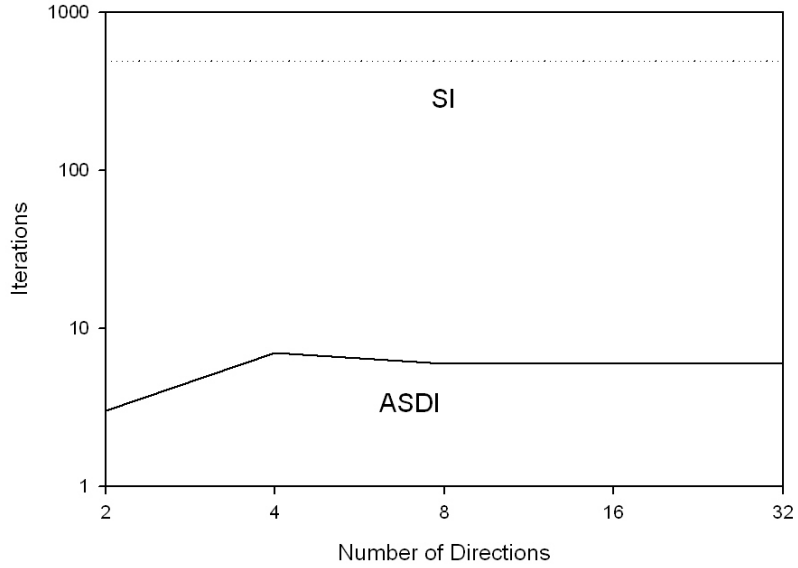

Figure 40 Plot of iterations versus angular quadrature for ASDI and SI. Convergence tolerance is 10^{-6} scattering ratio is 1.0, cell size is 2 MFPs.

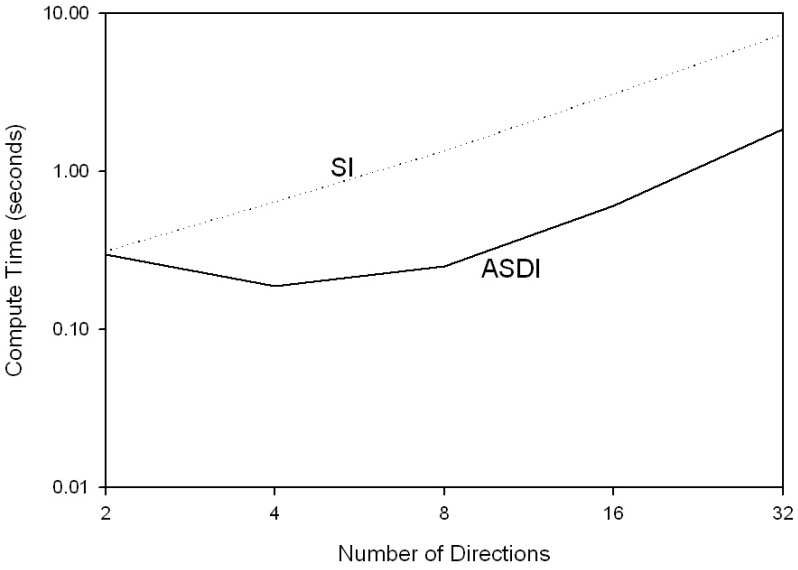

Figure 41 Plot of compute time versus angular quadrature for ASDI and SI. Convergence tolerance is 10^{-6} scattering ratio is 1.0, cell size is 2 MFPs.

This section demonstrated the strength of the ASDI method with the EC spatial quadrature for a homogeneous material. The most important characteristic examined was accuracy for each of the parameters studied. Each experiment showed that ASDI applied to EC was reliably accurate within the convergence tolerance required whereas SI was not. The application of ASDI to the non-linear EC method demonstrated very similar results to the method's application to SC. This confirmed the hypothesis that beta could be found and fixed for each iteration resulting in an algorithm that was similar to that which obtained outstanding result with SC. The EC algorithm essentially adds a root finding subroutine. This result shows that the ASDI method is not limited to a linear spatial quadrature. It indicates a more general application. The method's reliable accuracy, low iteration count, and fast compute times across all parameters studied demonstrate that the method is robust, effective and efficient with EC for this homogeneous problem. The next section examines the method's performance when applied to a heterogeneous material.

Periodic: Two Regions Repeated 10 Times

The second test problem investigated is the same problem investigated second with SC. It is a slab with a symmetry boundary on the left side and a vacuum boundary on the right side. Two materials of 1 cm cell width are placed side by side. This two material pattern is repeated 10 times for a total length of 20 cm. Material I had a total cross section of $1.0\,\mathrm{cm}^{-1}$, a scattering ratio of 1.0, and a uniform source of $1.0\,\mathrm{cm}^{-3}$. Its material properties remain fixed for all experiments. Material II had a total cross section of $1.0\,\mathrm{cm}^{-1}$, a baseline scattering ratio of 1.0, and no source. Material II's parameters were varied during the experiments. A diagram of these two materials was first shown in chapter three with Figure 19. It is redisplayed here for the reader's convenience.

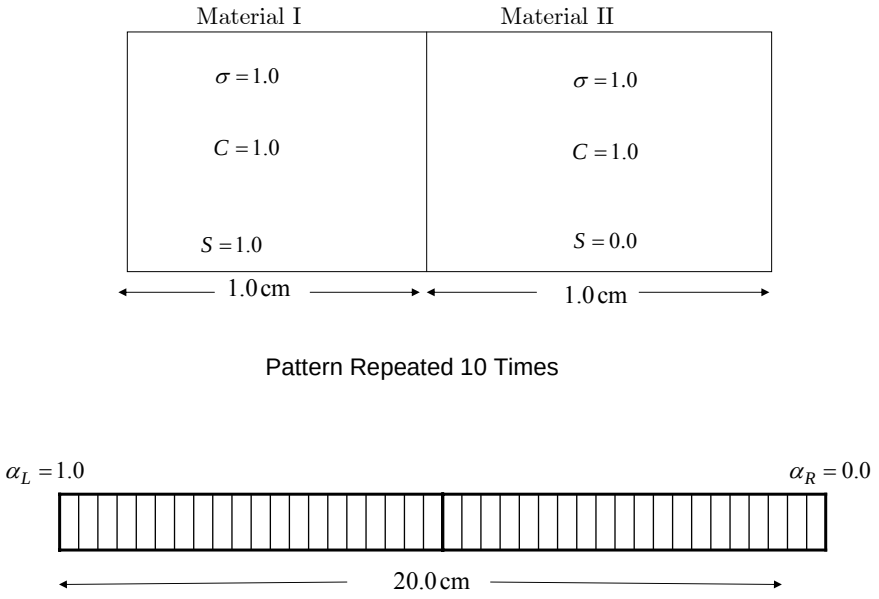

Figure 19 Problem 2

As with SC the first set of experiments for problem two tested the ASDI method's accuracy, effectiveness and efficiency versus scattering ratio fraction in Material II. Scattering ratio fraction was varied from 0.0 to 1.0. Angular refinement for this experiment was 8, refinement factor was 1 and convergence tolerance was 10^{-6}.

Accuracy is the first parameter presented. Figure 42 displays the symmetric relative difference between ASDI and SI ($\varepsilon_{\mathrm{SRD}}(\mathrm{ASDI,SI\_ASDI})$) and between ASDI and SI given the ASDI solution ($\varepsilon_{\mathrm{SRD}}(\mathrm{ASDI,SI\_ASDI})$). The plots show that ASDI applied to EC provides reliably accurate solutions for all scattering ratios while SI provides reliably accurate solutions only through scattering ratios of 0.6. The reliably accuracy of Figure 42 for EC is similar to the reliable accuracy of Figure 20 for SC. This shows that the beta convergence does not effect reliable accuracy of the method, even in problems that are not homogeneous.

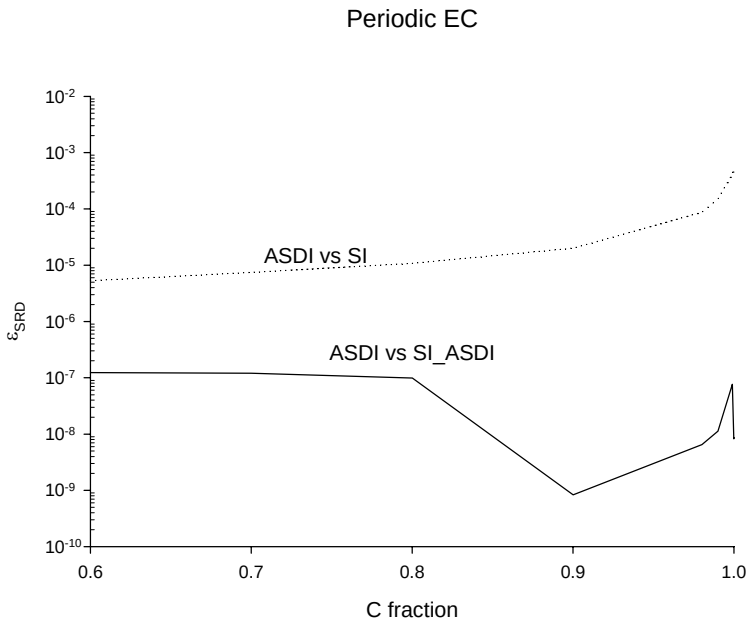

Figure 42: Symmetric Relative Difference ε_{SRD} between the ASDI solution and the SI solution as scattering ratios vary. Angular quadrature is DE-8, convergence tolerance is 10^{-6}, refinement is 50.

The effectiveness of the method was tested next. Figure 43 shows the method iteration count versus scattering ratio fraction for material II. This plot shows that ASDI converges in less than six iterations regardless of scattering ratio demonstrating its effectiveness, even when applied to EC, for heterogeneous materials with little or no absorption. These results are similar to those obtained from SC and demonstrate that beta convergence did not degrade effectiveness.

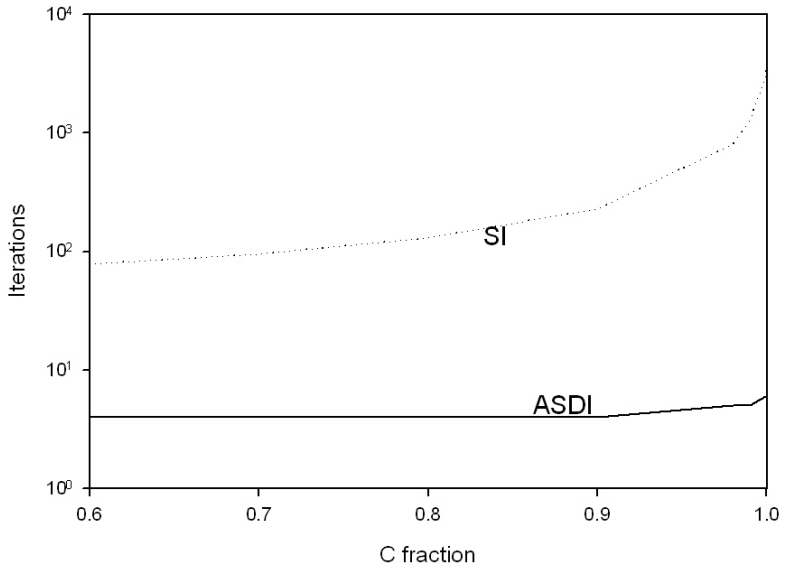

Figure 43: Plot of iteration count versus scattering ratio fraction. Angular quadrature is DE-8, convergence tolerance is 10^{-6}, refinement is 50.

Efficiency of the method is tested next. Figure 44 shows compute time versus scattering ratio fraction for material II. This figure shows that ASDI compute time is less than 0.1 seconds for all scattering ratios tested. Comparison of the ASDI and SI compute times demonstrate that ASDI is more computationally efficient than SI even when material II is a strong absorber and SI converges rapidly. The figure also shows that as scattering ratio approaches one in material II SI compute time climbs steeply but ASDI compute times do not. These results are similar to the compute times displayed in Figure 22 for SC. The results demonstrate that, although the beta convergence loop was added to the ASDI algorithm for EC, the algorithm does not require excessive compute time.

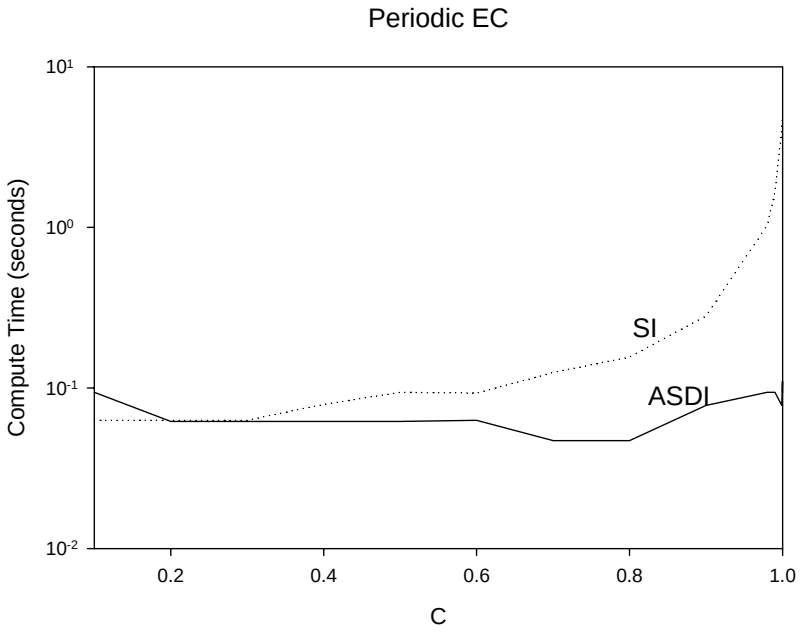

Figure 44: Plot of compute time (seconds) versus scattering ratio. Angular quadrature is DE-8, convergence tolerance is 10^{-6}, refinement is 50.

The next set of experiments for problem two demonstrate method accuracy, effectiveness and efficiency while refinement factor varies for material II. Scattering ratio for material II was fixed at 1.0. This tested ASDI in materials with little or no absorption. A material discontinuity exists even though cross sections and scattering ratios are the same because intrinsic sources are emitted only in material I. The refinement factor for material II was varied between 1 and 66.

Accuracy was tested first. Figure 45 displays the symmetric relative difference between ASDI and SI ($\varepsilon_{\text{SRD}}(\text{ASDI,SI\_ASDI})$) and between ASDI and SI given the ASDI solution ($\varepsilon_{\text{SRD}}(\text{ASDI,SI\_ASDI})$). The plots show that ASDI provides reliably accurate solutions for all refinement factors but SI does not.

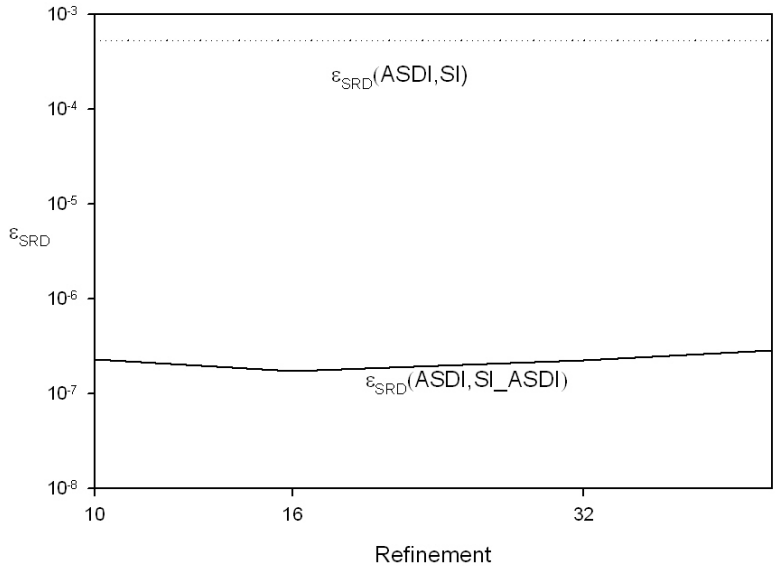

Figure 45: Plot of Symmetric Relative Difference ε_{SRD} between ASDI solution and SI solutions as cell mesh is refined. Angular quadrature is DE-8, scattering ratios are baseline values, convergence tolerance is 10^{-6}.

Effectiveness was next tested. Figure 46 shows that ASDI converges on a solution in less than 8 iterations for a refinement factor of 1 growing slightly as refinement factor is increased then remaining constant for refinement factors above 16. SI requires many more iterations than ASDI and provides unreliable solutions for these refinement factors.

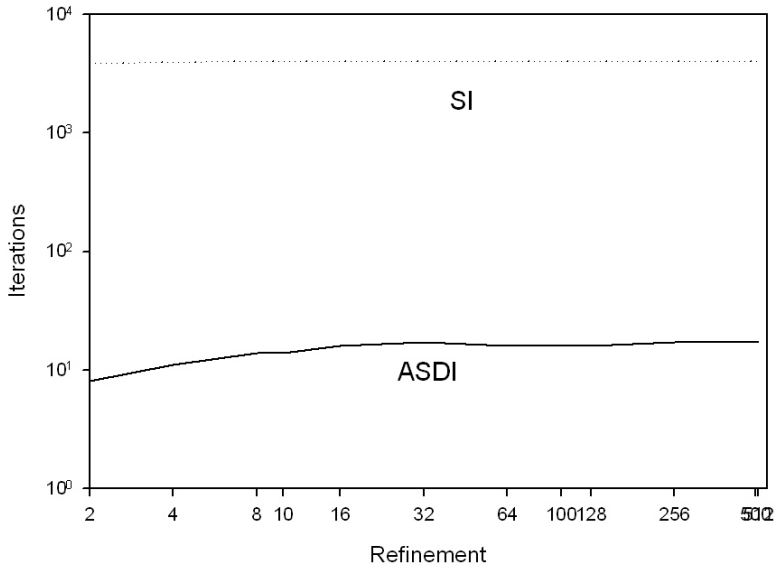

Figure 46 Plot of iteration count as cell mesh is refined. Angular quadrature is DE-8, scattering ratios are baseline values, convergence tolerance is 10^{-6}.

Computational efficiency was next tested. Figure 47 demonstrates that ASDI requires less compute time than SI regardless of mesh size for the baseline scattering ratios selected. However, as spatial mesh is refined the compute time of ASDI is nearly the same as the compute time of SI. The relatively comparable compute times of SI and ASDI do not indicate that SI is just as efficient as ASDI for these fine spatial meshes because SI does not provide reliably accurate answers. ASDI does not require excessive compute time regardless of refinement factors.

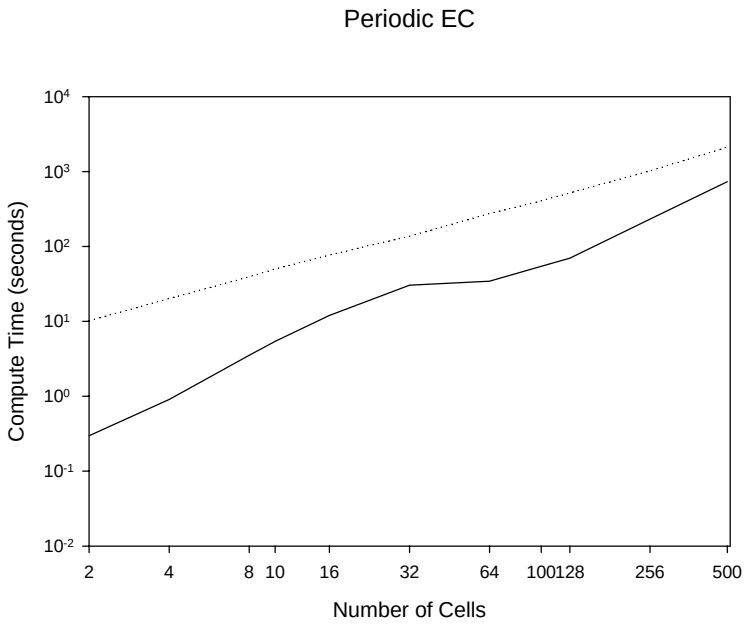

Figure 47: Plot of compute time as cell mesh is refined. Angular quadrature is DE-8, scattering ratios are baseline values, convergence tolerance is 10^{-6}.

Accuracy, effectiveness and computational efficiency were further tested with fixed scattering ratio and refinement factor for varying convergence tolerance and angular refinement with similar results. As in problem 1 these results indicate that ASDI remains reliably accurate, effective and efficient as these parameters vary. This is the same conclusion drawn for SC and provides strong confirmation that the non-linearity of the EC spatial quadrature algorithm does not prevent applying the ASDI algorithm to EC which is what I set out to do.

These experiments demonstrate the strength of the ASDI method for a two region periodic material. The experiments show that ASDI was always reliably accurate and that the parameters with the greatest impact on iteration count and compute time were scattering ratio and refinement factor. The experiments presented kept cross sections constant but varied spatial refinement. In order to fully stress material discontinuity in this periodic problem I next examined the impact of varying both scattering ratio and cross section simultaneously in material II, just as I did with SC. I varied scattering ratio fraction from 0.0 to 1.0 and cross section from 10^{-7}cm^{-1} to

$10\,\mathrm{cm}^{-1}$. This range of cross sections is not the same as the range of cross sections used for SC (i.e. $10^{-7}\,\mathrm{cm}^{-1}$ to $10^{7}\,\mathrm{cm}^{-1}$). That is because the exponential characteristic method as currently implemented can be used for optical thicknesses ($\frac{\sigma\Delta x}{\mu}$) of about 80. The limitation in cross section results from numerically poor conditioning in the calculation of EC transport coefficients. It is not a limitation of the ASDI method. I examined the impact of varying these two parameters on accuracy, effectiveness and efficiency at a refinement factor of 1.

A 3D plot of symmetric relative difference between ASDI and SI ($\varepsilon_{\mathrm{SRD}}(\mathrm{ASDI,SI})$) and between ASDI and SI given the ASDI solution ($\varepsilon_{\mathrm{SRD}}(\mathrm{ASDI,SI\_ASDI})$) is shown in Figure 48. This plot shows that ASDI is reliably accurate across the range of material properties tested. The plot shows a spike in $\varepsilon_{SRD}(ASDI, SI\_ASDI)$ at cross sections of approximately $10\,cm^{-1}$. Since this spike is in the region that is below the convergence tolerance that was required (10^{-6}) I draw no conclusions. The spike indicates that cross section values greater than $10\,cm^{-1}$ might be unreliable.

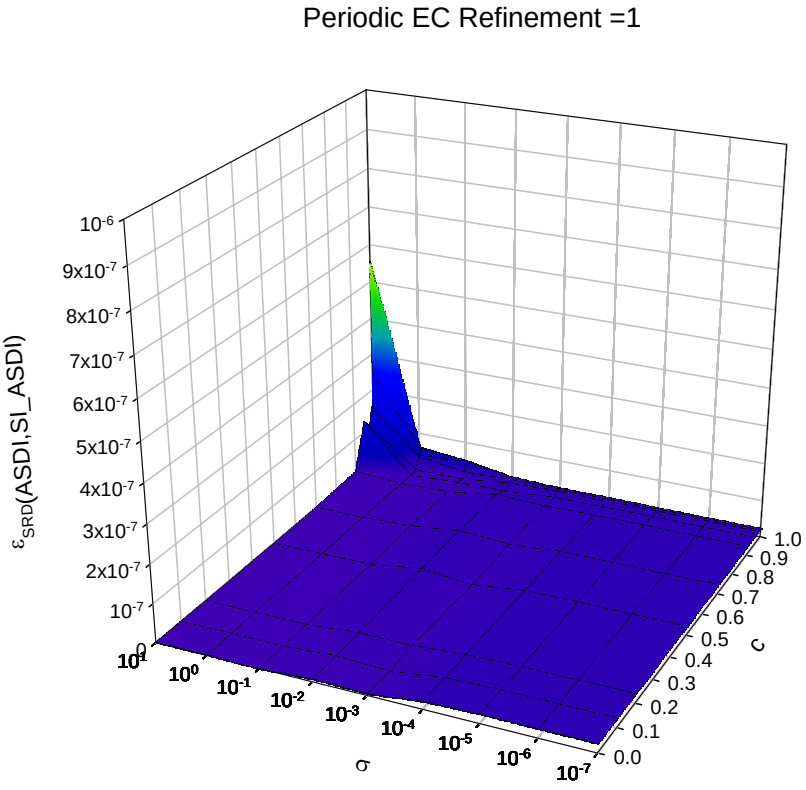

Figure 48: 3D Plot of ASDI symmetric relative difference between ASDI and SI ($\varepsilon_{\mathrm{SRD}}(\mathrm{ASDI,SI\_ASDI})$) and between ASDI and SI given the ASDI solution ($\varepsilon_{\mathrm{SRD}}(\mathrm{ASDI,SI\_ASDI})$) as scattering ratio and cross section vary . Angular quadrature is DE-8, convergence tolerance is 10^{-6}, refinement factor is 1.

A 3D plot of ASDI iteration count versus cross section and scattering ratio is shown in Figure 49.

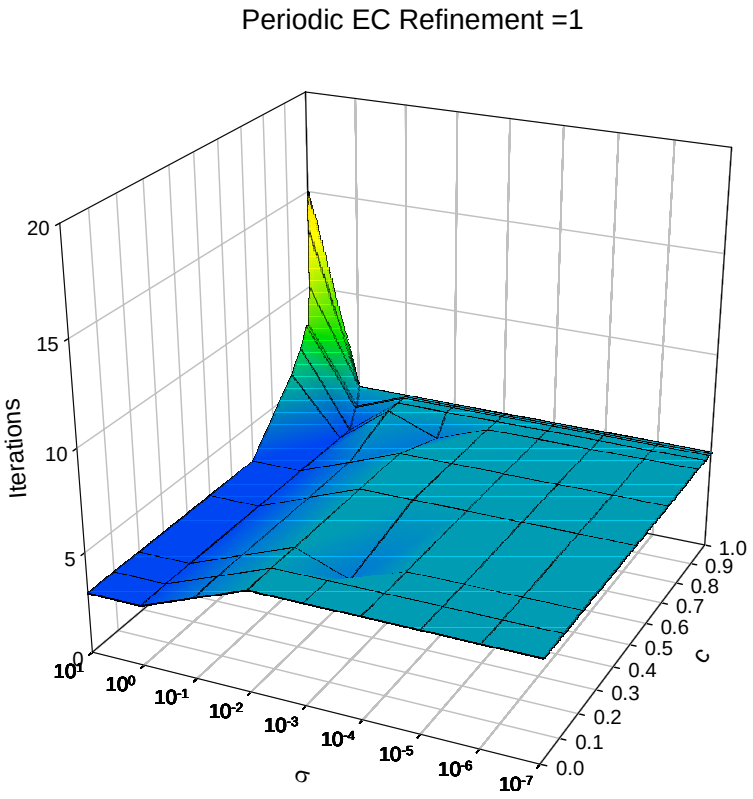

Figure 49: 3D Plot of ASDI iteration count as scattering ratio and cross section vary . Angular quadrature is DE-8, convergence tolerance is 10^{-6}, refinement factor is 1.

This figure demonstrates that ASDI is not sensitive to scattering ratio for cross sections less than $1 cm^{-1}$. For cross sections less than $1 cm^{-1}$ ASDI takes 7 iterations or less to converge. Iteration count increases sharply near scattering ratios of one and cross sections of $10 cm^{-1}$. Further investigation is needed to determine the reason for this increase in iteration count. It was not present with ASDI applied to SC as displayed in Figure 27.

As with SC a low iteration count is not useful if computational cost is prohibitive. A comparison of the time required for ASDI and SI to solve the problem is shown in Figure 50. The ratio of the ASDI compute time to SI compute time is shown in the figure, if this ratio is less than 1.0 then ASDI takes less time than SI. This is the case for cross sections less than $10^{-2} cm^{-1}$. The figure shows that SI takes one tenth the compute time of ASDI for cross sections greater than $10^{-2} cm^{-1}$ with scattering ratios of

0.1. In this region SI converges in 9/100 second and ASDI converges in 60/100 second. SI converges very rapidly because the problem is absorptive in more than half problem material. However, SI converges falsely. This false convergence occurs because half the problem (material one) has little or no absorption even when the scattering ratio of material two is nearly zero. In general, SI takes less compute time than ASDI when scattering ratios are less than 0.6 and cross sections are greater than $10^{-2}\,cm^{-1}$. In this domain SI converges in nearly no time at all. Even in these problems ASDI compute times are practical and competitive with SI compute times. More importantly, ASDI provides reliably accurate answers across the full range of cross section and scattering ratio parameters just as it did with SC. Further research is required to determine if the greater compute times required for cross sections greater than $10^{-2}\,cm^{-1}$ result from the calculation of EC transport coefficients.

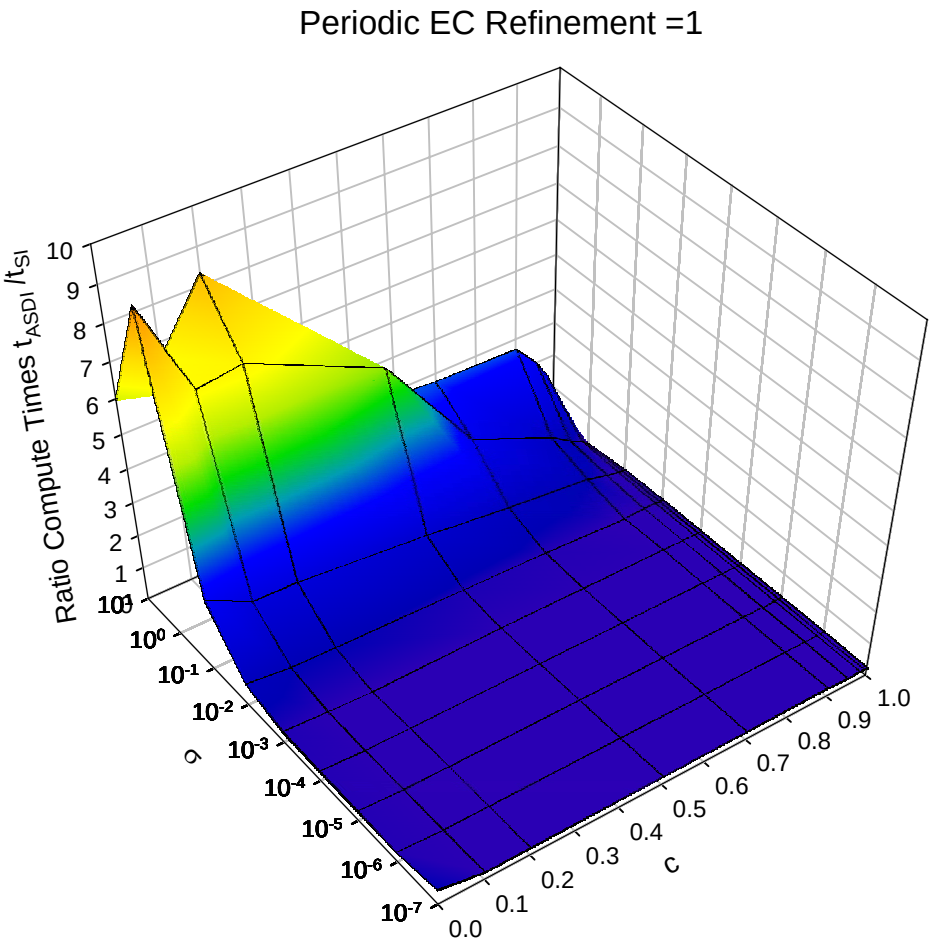

Figure 50: 3D Plot of the ratio ASDI compute time to SI Compute time as scattering ratio and cross section vary . Angular quadrature is DE-8, convergence tolerance is 10^{-6}, refinement factor is 1.

These experiments demonstrate that ASDI is reliably accurate for all the parameters studied and therefore robust. The method dramatically reduces iteration count and required compute time for diffusive problems. The experimental results show that ASDI is a useful and practical iteration scheme for any material properties. The method now allows researchers to examine the computation of EC transport coefficients in problems that are optically thick with little or no absorption.

VI. Summary and Conclusions

Accurate, and robust positive spatial quadrature schemes used in discrete ordinates methods, such as EC, provide physically meaningful, non-negative fluxes given non-negative incident fluxes, non-negative emission sources, and non-negative scattering cross sections. In 1969 K.D. Lathrop eloquently stated why positive spatial quadratures are needed. He said that in addition to numerical difficulties there are "psychological problems" with negative fluxes. The user who understands the transport equation and not just the numerical solution procedure knows that there is no such thing as a negative angle integrated flux, and rapidly becomes cynical about the effectiveness of a program which produces negative numbers (*12* :476)". Mathews et all have been developing the EC spatial quadrature since the early 1990's which is positive and approaches fourth order in its spatial convergence. To date this method has been difficult to implement in problems where scattering ratios were nearly one (7:36, 11:165). EC and other more conventional spatial quadratures based on source iteration are impractical for highly diffusive, optically thick problems. The objective of this effort was to develop an accurate and efficient scheme to rapidly converge EC. This has been done for slab geometry. This contribution makes it possible to use the exponential characteristic method, and similar methods, for real materials, even for notoriously slow transport computations involving one or a few groups describing the thermal neutron energy range from about 0 to 1 eV. (2:83). I originally explored synthetic acceleration as the method to rapidly converge these quadratures. Although successful for most problems this technique diverged for problems with sharp material discontinuities. By taking advantage of the lessons learned from synthetic acceleration, I found it possible to formulate a new transport method that more directly solves for fine angular resolution flux and spatially coupled coarse angular resolution flux. The fine angular quadrature accounts for the contribution of infinite number of particle flights to scattered source within a single cell. The coarse angular quadrature accounts for the

contribution of an infinite number of particle flights to scattered source across the spatial domain.

The introduction of two transport techniques, one producing full angle coupling for a fine quadrature and one producing full spatial coupling without iteration are both major contributions of this research. The ability to couple these methods and iterate on transport coefficients for both EC and SC instead of source iteration removes the need to accelerate optically diffuse problems per se. The transport method provides the estimate of infinite particle flights. The ASDI method provides an alternative to conventional source iteration at the expense of a larger linear algebra problem. It has the demonstrated advantage robustness (reliably accurate for the problems it is designed for) effective (requires few iterations) and efficient (requires practical compute times).

The coupling of the two transport methods worked surprisingly well. The discovery that EC converges rapidly with this method and can now be applied to diffusive problems should lead to renewed interest in the EC spatial quadrature within the transport community.

The use of flux weights to project between coarse and fine angular quadratures is general with respect to the spatial quadrature chosen. Extension to other positive spatial quadratures is immediate. This should further generate interest within the community for the method developed. Spatial quadratures that do not preserve positive flux require further research regarding flux weighting. I did not derive a method to calculate flux weights when faced with negative currents. Flux weights as employed in the method approximate flux distributions at cell edges. These flux weights conserve angular information while collapsing to a coarse quadrature that readily captures diffusive behavior. The concept of flux weights, and cell edge flux distribution should find application in a wider set of transport applications.

The method has been implemented in FORTRAN-95 on a PC, demonstrating the computational practicality of the approach in slab geometry with isotropic cross sections. The method as derived is immediately extendable to anisotropic scattering cross sections. Its extension to multiple dimensions will entail flux weighting on four cell edges vice two and an efficient solver for the spatially coupled coarse angular quadrature. The minimum bandwidth of the coefficient matrix which readily inverts in 1D will require research to develop an efficient 2D solver. However, the demonstrated

ability to cast a fine angle problem into an equivalent coarse angle problem should make the effort in 2D tractable.

The fine angle routine algorithm 6 is readily parallelizable. The routine uses iteration edge flux as an estimate for each spatial cell. Substantial improvement in performance can be obtained by parallelizing this subroutine. Further, profiling reveals that 60% of computational effort (time) is spent with this routine. Hence significant reduction in the ASDI method's overall computational efficiency would result from this parallelization. The method as developed lends itself to adoptive spatial and angular meshing. There is good reason to believe that a problem, such as the periodic horizontal interface tested, could use a coarse angular and spatial mesh in regions without material discontinuity and a finer mesh in regions that needed to capture angular or steaming behavior. Research in this area is straightforward.

The code written for this research is not a production code. A graphical user interface to obtain user input defining a flexible range of problem parameters is needed. This user interface should also interface with available cross section computational tools such as the NJOY suite of algorithms and Gerts' PAX cross sections. Nevertheless, the practicality of my method has been demonstrated successfully for EC which is what I set out to do.

Appendix A

This appendix demonstrates that $\varepsilon_{SRD}(x,y)$ meets the requirements for a distance function and that it can readily be applied to vectors in FORTRAN 90.

A1. $\varepsilon_{SRD}(y,x)$ as a distance function

A non-empty ,X, set together with a 'distance function' $\varepsilon_{SRD}(x,y)$ is said to form a metric space provided that:

$$\varepsilon_{SRD}(y,x) = 0 \text{ iff } \quad x = y \tag{1}$$

$$\varepsilon_{SRD}(y,x) = \varepsilon_{SRD}(x,y) \geq 0 \qquad \forall\, x, y \in X \tag{2}$$

$$\varepsilon_{SRD}(y,x) = \varepsilon_{SRD}(x,z) + \varepsilon_{SRD}(y,z) \qquad \forall\, x, y, z \in X \tag{3}$$

The distance function $\varepsilon_{SRD}(y,x)$ is

$$\varepsilon_{SRD}(x,y) = \frac{2|x-y|}{|x|+|y|} \tag{4}$$

The numerator in equation (4)

$$2|x-y| = 0 \tag{5}$$

is zero if and only if and only if

$$|x-y| = 0 \tag{6}$$

This occurs only if x = y. The denominator in equation (4) is only zero if x and y are zero in which case the distance between them is zero. Equation (4) is then zero only if equation (6) is zero. This occurs if only when x=y meeting requirement one.

If x is not equal to y, and x >0, and y>0 then

$$\left(2\frac{|x-y|}{|x|+|y|}\right)_{\max} = 2\frac{(|x-y|)_{\max}}{(|x|+|y|)_{\min}} = 2\frac{(|x|+|-y|)_{\max}}{(|x|+|y|)_{\min}} = 2\,, \tag{7}$$

and

$$\left(2\frac{|x-y|}{|x|+|y|}\right)_{\min} = 2\frac{(|x-y|)_{\min}}{(|x|+|y|)_{\max}} = 2\frac{(|x|+|-y|)_{\min}}{(|x|+|y|)_{\max}} = 0\,, \tag{8}$$

which meets requirement two.

If $0 < x < z < y$ then

$$\frac{|x-y|}{|x|+|z|} = \frac{z-x}{z+x} \tag{9}$$

and

$$\frac{|y-z|}{|y|+|z|} = \frac{y-z}{z+y}\,. \tag{10}$$

Adding equation (10) to equation (9) results in

$$\frac{z-x}{z+x} + \frac{y-z}{z+y} \geq \frac{y-x}{x+y}\,. \tag{11}$$

Multiplying each of the terms by the appropriate denominator results in

$$(z-x)(z+y)(x+y) + (y-z)(z+x)(x+y) \geq (y-x)(z+x)(z+y)\,. \tag{12}$$

Subtracting the right side from the left side of equation (12) and simplifying results in

$$(x-y)(x-z)(y-z) \geq 0 \tag{13}$$

which is always true based on the initial condition $0 < x < z < y$. The same result can be shown if x, y or z are swapped. This demonstrates that the distance function meets the condition three.

A.2. Application of $\varepsilon_{SRD}(x,y)$ to Vectors $\varepsilon_{SRD}(\vec{x},\vec{y})$.

The distance function $\varepsilon_{SRD}(x,y)$ defined by equation (4) can be applied to vectors $\vec{x},\vec{y}$ resulting in a vector of distances $\vec{\varepsilon}_{SRD}(\vec{x},\vec{y})$. An element of this distance vector is

$$\varepsilon_{SRD_i}(\vec{x},\vec{y}) = \varepsilon_{SRD}(x_i, y_i). \tag{14}$$

In my algorithm I am interested in ensuring that no element of the distance vector $\vec{\varepsilon}_{SRD}(\vec{x},\vec{y})$ is greater than a convergence tolerance. Therefore, I define the maximum of the distance vector

$$\left\|\vec{\varepsilon}_{SRD}(\vec{x},\vec{y})\right\|_{\infty} = \mathrm{Max}\left[\varepsilon_{SRD}(x_i, y_i)\right]_{i=1,N}, \tag{15}$$

which is readily implemented in FORTRAN 90 using an elemental function.

```
SRD=Max(SymRelDif((x,y))
Where the SymRelDif function is
Elemental Function SymRelDif(x,y)
Real::Intent(in):: x,y
Real::SymRelDif
If (x=y) then
    SymRelDif=0
Else
    SymRelDif =Abs(x-y)/((abs(x)+abs(y))/2)
End if
End Function
```

Implementing the SymRelDif Function in Fortran

Bibliography

1. Miller, Elmer E. and Lewis, W. F. Computational Methods of Neutron Transport. Illinois: American Nuclear Society, 1993.

2. Kingman J. F. C., S. J. Taylor. Introduction to Measure and Probability. Cambridge, England: Cambridge University Press, 1966.

3. Adams, Marvin L. and Edward W Larsen. "Fast Iterative Methods for Discrete-Ordinates Particle Transport Calculations," Nucl. Sci. Eng, 40:3-149 (2002).

4. Chang, Jae, and Marvin Adams, "Analysis of Transport Synthetic Acceleration For Highly Heterogeneous Problems", Conference Paper from Nuclear Mathematical and Computational Sciences: A Century in Review, A Century Anew. 1/16-16/16. Gatlinburg, Tennessee, April 6-11, 2003, on CD-ROM, American Nuclear Society, Lagrange Park, IL (2003)

5. Warsa, J.S., Wareing, T. A., and J. E. Morel, "On the Degraded Effectiveness of Diffusion Synthetic Acceleration for Multidimensional SN Calculations in the Presence of Material discontinuities", Conference Paper from Nuclear Mathematical and Computational Sciences: A Century in Review, A Century Anew. 1/17-16/17. Gatlinburg, Tennessee, April 6-11, 2003, on CD-ROM, American Nuclear Society, Lagrange Park, IL (2003)

6. Mathews, Kirk, Glenn Sjoden, and Bryan Minor. "Exponential Characteristic Spatial Quadrature for Discrete Ordinates Radiation Transport in Slab Geometry," Nucl Sci. Eng ,(118:24-37).

7. Walters, Wallace F., and Wareing, Todd A., "An Accurate Strictly-Positive, Nonlinear Characteristic Scheme for the Discrete-Ordinate equations," Transport Theory and Statistical Physics, 25(2), 197-215, 1996.

8. Todd Wareing, Wallace F Walters,. and Jim E. Morel, "A Diffusion Accelerated Solution method for the Non-Linear Characteristic Scheme in Slab geometry," Nucl Sci. Eng , (124:72-81), 1996

9. Mathews, Kirk, David Gerts. "Nonnegative Anisotropic Piecewise-Average Multi-Group Cross Sections ," ", Conference Paper from Nuclear Mathematical and Computational Sciences: A Century in Review, A Century Anew. 1/16-16/16. Gatlinburg, Tennessee, April 6-11, 2003, on CD-ROM, American Nuclear Society, Lagrange Park, IL (2003)

10. Minor, Bryan, and Kirk Mathews. "Exponential Characteristic Spatial Quadrature for Discrete Ordinates Radiation Transport with Rectangular Cells ," Nucl Sci. Eng , (120:165-186)

11. Lathrop, K.D., "Spatial Differencing of the Transport Equation: Positivity vs Acuracy," *Journal of Computational Physics: 4:475-495 (1969)*

REPORT DOCUMENTATION PAGE	Form Approved OMB No. 074-0188

PLEASE DO NOT RETURN YOUR FORM TO THE ABOVE ADDRESS.

1. REPORT DATE *(DD-MM-YYYY)*	**2. REPORT TYPE**	**3. DATES COVERED** *(From – To)*
March-2004	**Ph D. Dissertation**	Jun 2000 – March 2004

4. TITLE AND SUBTITLE

A RAPIDLY-CONVERGING ALTERNATIVE TO SOURCE ITERATION FOR SOLVING THE DISCRETE ORDINATES RADIATION TRANSPORT EQUATIONS IN SLAB GEOMETRY

5a. CONTRACT NUMBER

5b. GRANT NUMBER

5c. PROGRAM ELEMENT NUMBER

6. AUTHOR(S)

Wager, Nicholas, J., LTC, US Army

5d. PROJECT NUMBER

5e. TASK NUMBER

5f. WORK UNIT NUMBER

7. PERFORMING ORGANIZATION NAMES(S) AND ADDRESS(S)
Air Force Institute of Technology
Graduate School of Engineering and Management (AFIT/EN)
2950 P Street, Building 640
WPAFB OH 45433-7765

8. PERFORMING ORGANIZATION REPORT NUMBER

AFIT/DSP/ENP-04-01

9. SPONSORING/MONITORING AGENCY NAME(S) AND ADDRESS(ES)

10. SPONSOR/MONITOR'S ACRONYM(S)

11. SPONSOR/MONITOR'S REPORT NUMBER(S)

12. DISTRIBUTION/AVAILABILITY STATEMENT
APPROVED FOR PUBLIC RELEASE; DISTRIBUTION UNLIMITED.

13. SUPPLEMENTARY NOTES

14. ABSTRACT
The discrete ordinates method has been used to provide engineering solutions to the Boltzmann neutral particle radiation transport equation since it was developed over forty years ago. Conventional applications of the method use von Neumann iteration on the scattering source, which requires acceleration methods such as diffusion synthetic acceleration for problems with regions in which particles scatter many times before being absorbed or leaking out. Sometimes these acceleration methods fail or are ineffective. Correcting these limitations is a current area of effort in this field. In this work, a new *angular-spatial distribution iteration* scheme was developed and demonstrated for slab-geometry problems. The new method proved to be comparable in computational storage and cost to the source iteration scheme even for problems that are easy for source iteration. In strongly scattering-dominated problems, for which source iteration requires the addition of an accelerator algorithm, the new scheme does not require an accelerator and reliably provides accurate results at moderate cost. Recent studies have revealed a class of problems for which diffusion synthetic acceleration is slow to converge and transport synthetic acceleration fails to converge. Our testing showed that the new angular-spatial distribution iteration performs well even with these challenging problems.

15. SUBJECT TERMS
Radiation Transport, Boltzmann Transport Equation, Discrete Elements, Discrete Ordinates, Rapidly Converging

16. SECURITY CLASSIFICATION OF: UNCLASSIFIED			**17. LIMITATION OF ABSTRACT**	**18. NUMBER OF PAGES**	**19a. NAME OF RESPONSIBLE PERSON**
REPORT	**ABSTRACT**	**c. THIS PAGE**			Kirk A Mathews Professor,(ENP)
U	**U**	**U**	**UU**	193	**19b. TELEPHONE NUMBER** *(Include area code)* (937) 255-3636, ext 4508; e-mail: Kirk.Mathewsl@afit.edu